THE MESSENGER

EL MENSAJERO

Munich
Paranal
La Silla
La Serena
Santiago

No. 79 – March 1995

European SL-9/Jupiter Workshop

On February 13–15, 1995, a Workshop on the SL-9/Jupiter collision took place at the ESO Headquarters in Garching. More than 100 astronomers from all continents discussed the various aspects of this unique event, from the numerous multi-wavelength observations on the ground and in space to the subsequent difficult interpretation of the complex physical and chemical processes that took place in Jupiter's atmosphere.

On page 19 of this Messenger issue, we bring the summary of the concluding round-table discussion. It reflects well the present status of the ongoing, hard labour by many groups around the world. While there has undoubtedly been significant progress within several areas, it is also obvious that it will still take quite some time before a coherent, detailed understanding emerges.

The Workshop Proceedings are already at the printer and will become available by mid-April 1995. (See announcement on page 47.)

TELESCOPES AND INSTRUMENTATION

Manufacturing and Assembling the VLT Main Structure

M. QUATTRI, ESO-Garching

The final design of the main structure was completed in May 1994. Since then, great progress has been achieved in building the components of the first two main structures, and the remaining two main structures have already been ordered. The large mechanical components, like azimuth tracks and centrepiece, are at present being manufactured. All the components of the first Main Structure (MS) to be erected and tested in Milan before the end of 1995 have been built. Some of them are undergoing the final machining, and they will reach the European erection site in Ansaldo Energia in Milan by August 1995, to allow the

Figure 1.

Figure 2.

Figure 3.

complete erection before the end of November 1995. Figure 1 shows one of the four parts of the base frame of the MS 1 painted in the final colour. The base frame is about 20 m long, 9 m wide and 1 m high and weighs about 60 tons. Figure 2 shows a picture of one of the pedestals in upside-down position holding the altitude hydrostatic bearings. The centrepiece during the machining of the seats of the altitude shafts installed on the machine is shown in Figure 3.

As already mentioned before, the erection of the Main Structure number 1 will take place in one of the buildings of Ansaldo Energia located in Milan. Figure 4 shows the concrete pier in which the steel plates composing the interfaces to the telescope, have been embedded, creating a surface planar within 0.4 mm. This operation has taken about two months and great care has been applied in pouring the shrinkless mortar, to avoid any permanent deformation in the steel plates, which could have jeopardised the planarity of the interface. The azimuth tracks, which compose the bearing journal of the azimuth thrust bearing system and the centring journal of the radial azimuth bearing system, have been installed on the steel plates. They are aligned with such a precision that they create a virtually perfect plane. The planarity is about 0.08 mm and the run out of the centring journal of the inner track, which defines the run out of the telescope azimuth axis, is less than 0.1 mm.

The motors and the encoders have been built and are now on the way to Milan for integration. The tests carried out on the prototypes have shown that their performance is within specification.

For further information please contact:
M. Quattri, ESO-Garching:
e-mail: mquattri@eso.org

Figure 4.

Manufacturing of the VLT Primary Mirrors – a Brief Progress Report

P. DIERICKX, ESO, Garching

Of the four primary mirrors of the VLT, two are presently under figuring at REOSC's plant in St. Pierre du Perray, and two at SCHOTT's plant, one under fine annealing and the fourth ready to have its centre hole ground out. For comic's addicts, these are Joe, Jack, William and Averell.

Joe's first light occurred in December when REOSC switched from infrared to visible interferometry. Figure 1 shows the mirror being cleaned prior to an optical test run. The robot arm is visible at the left; at the centre of the picture is the cleaning head which projects water onto the surface. At the top of the picture is the lower opening of the inflatable skirt. Upon testing the latter descents down to the edge of the mirror to provide a suitable thermal insulation of the test tower. Polishing is due to proceed until May 1995, and the current status of the mirror is about 1 micron RMS wavefront error. Consistent data obtained through different test setups show that the curvature and conic constant are already within tolerances. A definite confirmation should be obtained upon acceptance tests in May/June. The accidental scratch that occurred early 1994 has been totally polished.

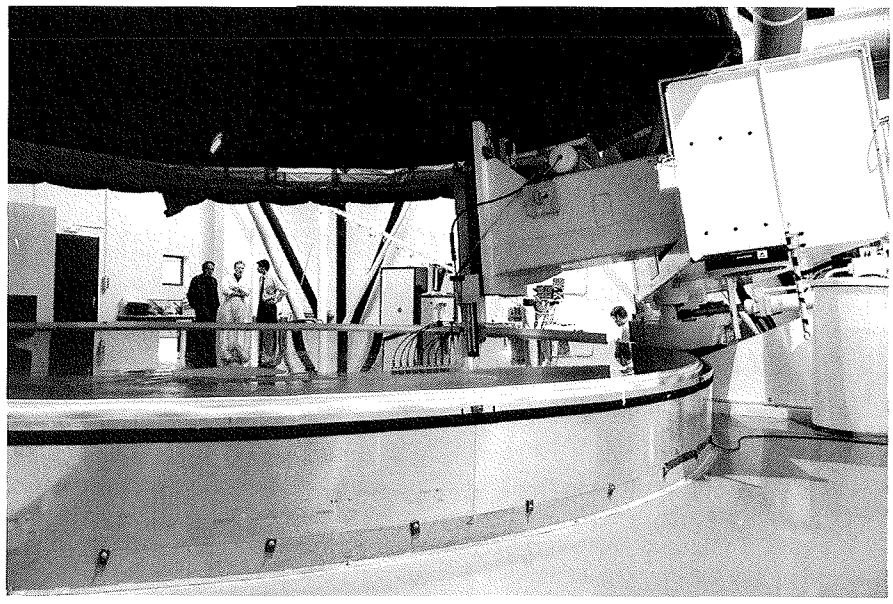

Figure 1: *Joe being washed (with permission by REOSC).*

Figure 2: *Jack's arrival at the optical figuring plant (with permission by REOSC).*

Jack was delivered by SCHOTT in October 1994. Final inspection revealed outstanding geometrical accuracy and internal quality, in line with the first (and then rated exceptional) achievements made by SCHOTT with Joe. Bubble and inclusion content is extremely low. Compressive stresses around the centre hole are somewhat higher than with Joe, but still within the standard for special quality Zerodur. Transport to REOSC took quite some time because of bad weather conditions in the Channel. Figure 2 shows Jack's arrival at the REOSC plant at 2:00 a.m. on November 22, 1994. The background shows the new REOSC plant built next to the VLT facility. Since then the axial pads have been glued and grinding is starting. Delivery of the finished mirror (ex works) is scheduled for June 1996.

William should be delivered by SCHOTT in July/August 1995. At the moment it is under ceramisation and should come out by mid-May for final machining. Averell is under quality inspection prior to grinding its centre hole. Delivery is foreseen in October.

For further information please contact:
P. Dierickx, ESO-Garching,
e-mail: pdierick@eso.org

Impact of the Microseismic Activity on the VLT Interferometer

B. KOEHLER, F. KOCH, ESO-Garching; L. RIVERA, EOPGS, Strasbourg, France

1. Introduction

In a previous article ("Hunting the Bad Vibes at Paranal", Messenger No. 76 – June 1994), we described the approach followed by ESO to investigate the effect of microseismic noise on the VLT Interferometer (VLTI). In section 4 of that article, we presented a measurement campaign performed at Paranal to precisely characterise the natural microseismic activity in view of assessing its impact on the VLTI performance. At that date, only preliminary results were available and presented.

This article presents the final results of this campaign which provide the statistical characterisation of the micro-activity as seen from Paranal, as well as the evaluation of its impact on the stability of the Optical Path Length inside the VLT 8-m telescope.

2. Characterisation of the Natural Seismic Activity at Paranal

As a preamble to the field experiment at Paranal described in the next sections, the Ecole et Observatoire de Physique du Globe de Strasbourg (EOPGS) performed for ESO a specific processing of the seismic data obtained with its permanent monitoring network installed in the Antofagasta area since 1990. This processing consisted in characterising the seismic activity in that area in terms of earthquakes' magnitude (Richter scale), precise localisation of the sources and frequency of occurrence. Figure 1 illustrates a result of this pre-study. It shows the location of earthquake epicentres and their magnitude for a one-year period (July 1990–June 1991).

2.1. Field experiment

The field experiment was carried on from March 21–31, 1994 at Paranal by Dr. L. Rivera, seismologist from EOPGS, and B. Koehler from ESO-Garching with the logistic support of ESO-Paranal.

Three different kinds of ground motion were recorded during this period: (i) background seismic noise samples in the absence of any seismic events or artificial disturbance, (ii) seismic events due to earthquakes, (iii) human-made noise samples. The noise samples were recorded continuously within pre-defined time windows; with duration ranging from 2 to 10 minutes. The sample frequency used was 500 Hz and occasionally 1000 Hz. Seismic events, on the other hand, were recorded by triggering; the signal was continuously digitised and fed to a detection algorithm which decided whether "an event" was presently arriving. In this case, the recording was activated including a pre-trigger window. A sample frequency of 250 Hz was selected.

All noise samples were recorded during the night at the location of Telescope No. 4. The seismic events were monitored during day and night at the same location but also at the so-called "NTT peak" some 1.5 km north-east from the Paranal top to avoid contamination by human activity during certain days.

The measurement set-up included two types of high-sensitivity seismometers; uni-axial Kinemetrics SS-1 and tri-axial Mark-Product L4-3D. Both are velocity transducers based on the spring-mass principle. The inertial motion of the mass/magnet with respect to the outer cage equipped with a coil creates a voltage proportional to the velocity of the seismic mass.

A Reftek 72A-07 seismic station was used to digitise and record the signals coming from the seismometers. The A/D conversion (24 bits) was performed at a very high sample rate of 16 kHz, then a digital FIR filter was used to perform anti-alias filtering of the raw data. Finally the data were decimated to the selected output sample rate.

A portable Sun Workstation was also brought to the field, in order to read the tapes, visualise the signals and make a preliminary signal analysis.

The resolution and the noise of the whole acquisition chain was carefully computed and experimentally checked. The resolution was 3.10^{-10} m/s and the noisepower spectral density 2.10^{-10} (m/s)/$\sqrt{\text{Hz}}$). This very high sensitivity prevented to be limited by the measurement noise even for the very low level of the natural background seismic noise.

2.2. Data analysis and results

The total effective time of seismic monitoring by triggering was 125 hours. Figure 2 shows a typical example of recording. A total of 164 events due to earthquakes were recorded during the time mentioned above. For each of them, the following parameters were calculated: (i) the distance of the earthquake epicentre from Paranal, (ii) the seismic moment, (iii) the Richter magnitude and (iv) a parameter representing the level of the local ground acceleration called Γ, and defined later in this section.

Distance between Paranal and the earthquake source were obtained from the so-called, S-P delays. Indeed, even though the propagation speeds of the shear (S) and compression (P) waves varies with the local earth material, their difference is almost a constant. This permits to determine the distance from the difference of arrival times of the two waves. Figure 3 shows a histogram of the number of recorded events as a function of their distance. Some interesting remarks can be made from this histogram (see caption of Figure 3). The most important one is the absence of seismicity closer than 25 km. This indicates the absence of earth-

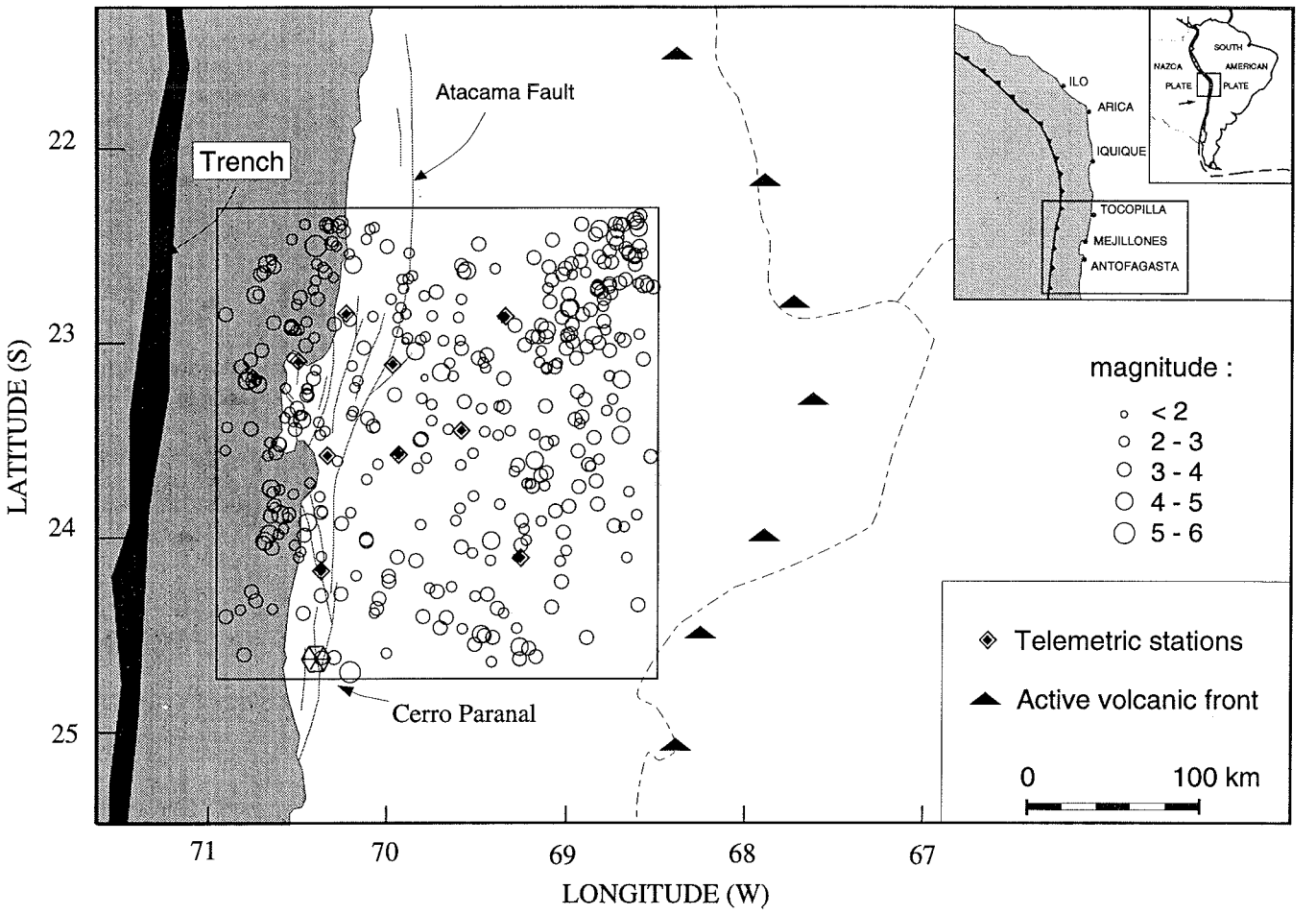

Figure 1: *Map and cross-section of the Antofagasta area showing the location of earthquake epicentres and their magnitude for a one-year period (July 1990–June 1991). These maps were generated for ESO by the EOPGS from data collected with its permanent seismic monitoring network.*

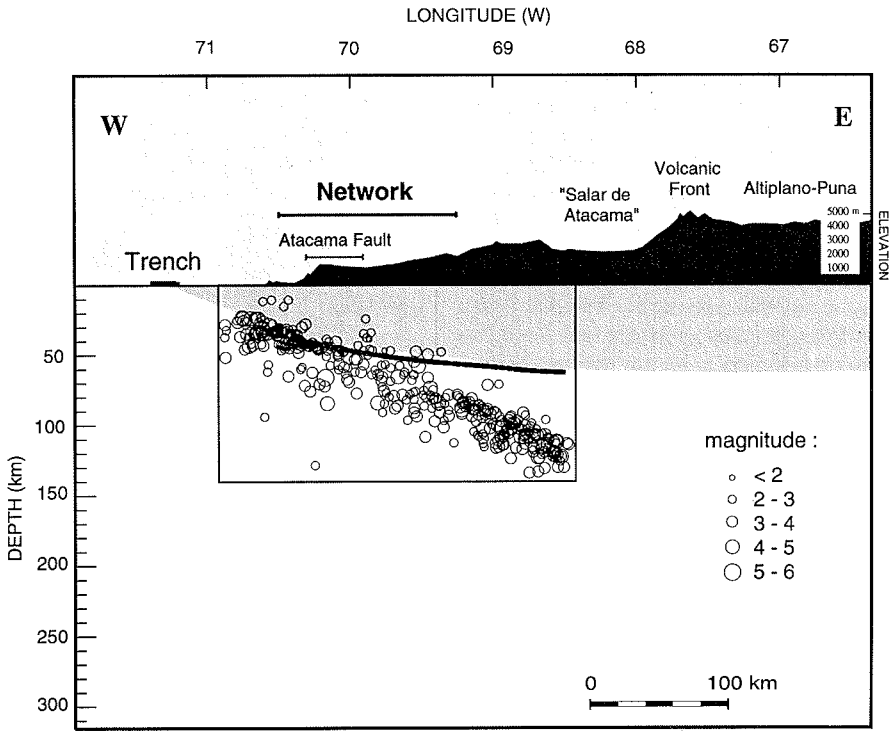

quake sources very close to the Earth surface which can be particularly destructive (refer, for example, to the effects of such a crustal earthquake in Kobe-Japan in January 1995). This fact is confirmed by the permanent seismic monitoring of the Antofagasta area performed by EOPGS over the last years (see Figure 1). It is also a confirmation of previous observations by the EOPGS that the Atacama Fault, which runs roughly in north-south direction some 4 km east of Paranal, has a very low activity. All that is, of course, very positive for the operation of the VLT since even small events so close from Paranal could produce important acceleration.

A Local Richter Magnitude (ML), which characterises the intrinsic strength of an earthquake, was calculated for each event from the seismogram and taking into account the computed distance. Another measurement of the strength of an earthquake is the Seismic Moment (M0), a well-defined physical value, which is intimately related to the standard dislocation model for tectonic earthquakes. These parameters which are theoretically linearly related were used to check successfully the homogeneity of the sample. The largest Richter magnitude recorded during the campaign was 5.17 (at 377 km) and the smallest was 0.82 (at 37 km).

The action of an earthquake on the structure of the VLT is, of course, function of the Magnitude (or Seismic Moment) and distance (geometric and intrinsic attenuation). The level of ground acceleration might be the same with a small nearby earthquake or with a larger-distant event.

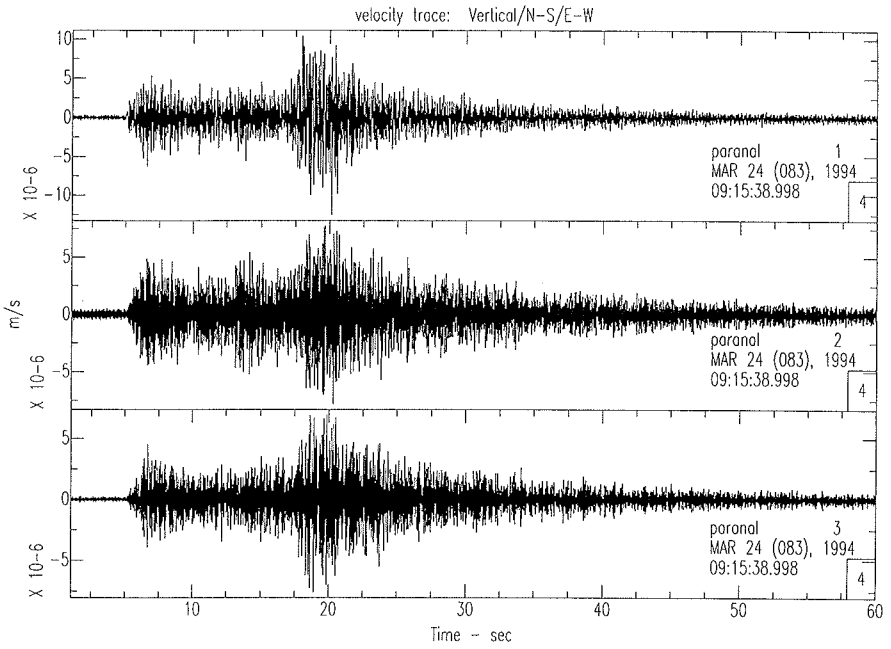

Figure 2: *A typical example of recording of a seismic event at Paranal. The start of recording is March 24 at 9 h 15' 39". The three components of the motion (velocity: m/s) are represented against time (sec). From top to bottom: Vertical, N-S and E-W directions. The arrival of the compression wave (P-wave) occurs 5 seconds after the beginning of the record and the shear wave (S-wave) arrives 12 seconds later. This difference of arrival times allows to determine the distance to the earthquake source (here: 100 km). Amplitudes in these three components are quite similar and velocity peaks at about 10 μm/s. Duration of events is of the order of 60–70 seconds.*

For this reason, we defined the local parameter Γ as the average level of the ground acceleration Power Spectral Density (PSD) in the frequency range [10–50 Hz] expressed in nano-g/$\sqrt{\text{Hz}}$. This parameter is adequate to investigate the effect on the VLTI for two reasons: (i) the acceleration PSD is almost flat (white noise) in this frequency range (in fact up to 100 Hz) and can therefore be characterised by its average, (ii) the most significant structural modes of the VLTI subsystems have frequencies in this range. The smallest Γ value recorded was 6 ng/$\sqrt{\text{Hz}}$ corresponding to an earthquake of ML = 1.6 at 138 km. The largest value recorded was 9581 ng/$\sqrt{\text{Hz}}$ corresponding to an earthquake of ML = 4.5 at 160 km. This last event occurred during the night and the acceleration was enough to awake some people at Paranal.

A number of verifications were done to ensure the representativity of the Γ parameter. In particular, the value used later in the analysis, which is computed on the whole 60-second seismogram, was compared with the more instantaneous values obtained on a running window of 2 seconds. It came out that the maximum values of the acceleration PSD reached at the arrival of the P & S wave are very well correlated with the "average" value given by Γ and exceed it by a factor of about 1.5 during some 5 seconds.

The ultimate goal of the campaign was to determine the statistics of the Γ parameter. To this end, a diagram similar to the so-called Gutenberg-Richter law was constructed. The Gutenberg-Richter law is used by the seismologists to characterise the seismic activity in a given area. It represents the logarithm of the number of earthquakes with a magnitude higher than M which occurred during a given period versus the magnitude M. The similar diagram for the Γ parameter is shown in Figure 4 for the duration of the experiment (125 hours). As for the standard Gutenberg-Richter law, the relationship is fairly linear. The departure from the linear relationship for low values of Γ (<100 ng/$\sqrt{\text{Hz}}$ is an artefact due to the non-completeness of the sample for these low levels of acceleration which did not always trigger the acquisition.

From Figure 4 we can extrapolate this law for a week (168 hours):

$$\log_{10}(N) = 4.778 - 1.162 \times \log_{10}(\Gamma) \quad (1)$$

Where:

N: number of seismic events during 1 week which exceed the level of acceleration Γ

Γ: average level of the ground acceleration PSD between 10 and 50 Hz in ng/$\sqrt{\text{Hz}}$.

This means that on average each week there is an event with $\Gamma \geq 13000$ ng/$\sqrt{\text{Hz}}$ or each night one with $\Gamma \geq 1300$ ng/$\sqrt{\text{Hz}}$ and three events with $\Gamma \geq 500$ ng/$\sqrt{\text{Hz}}$ or each hour one event with $\Gamma \geq 160$ ng/$\sqrt{\text{Hz}}$.

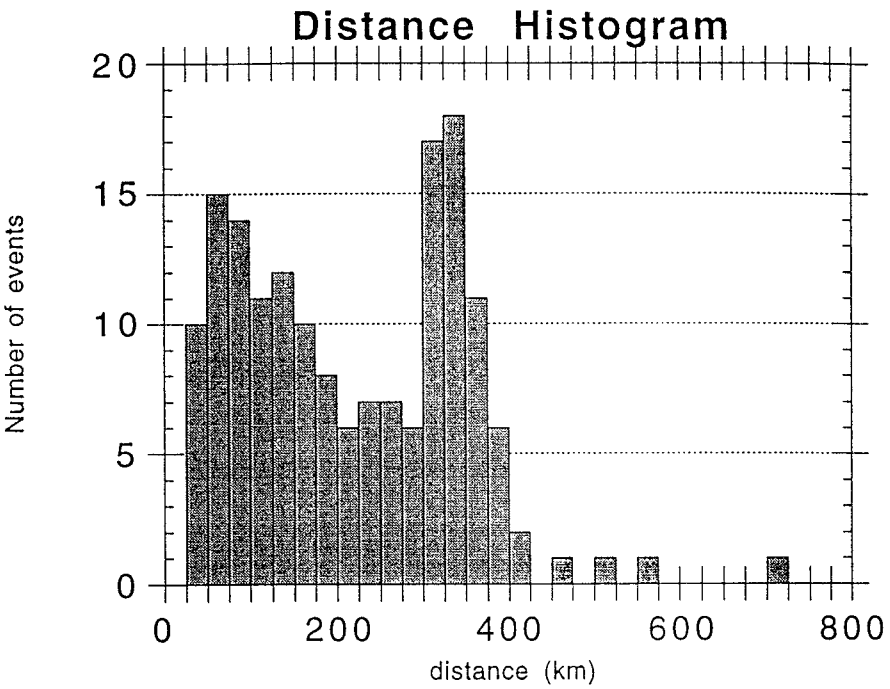

Figure 3: *Histogram of the number of earthquakes recorded during the 10-day measurement campaign as a function of their distance from Paranal. The absence of events closer than 25 km comes from the fact that the earthquake sources are located near the subduction plane which lies about 30 km below Paranal (see also Figure 1). Except for the very active zone at 350 km which probably corresponds to a cluster of deep seismic activity already identified by the EOPGS on the Argentinean border, the regular decrease of the histogram is consistent with the simple hypothesis that the earthquakes are uniformly distributed along the subduction plane. Events more distant than 400 km are rare and far enough to be unimportant for the every-day operation of the VLT.*

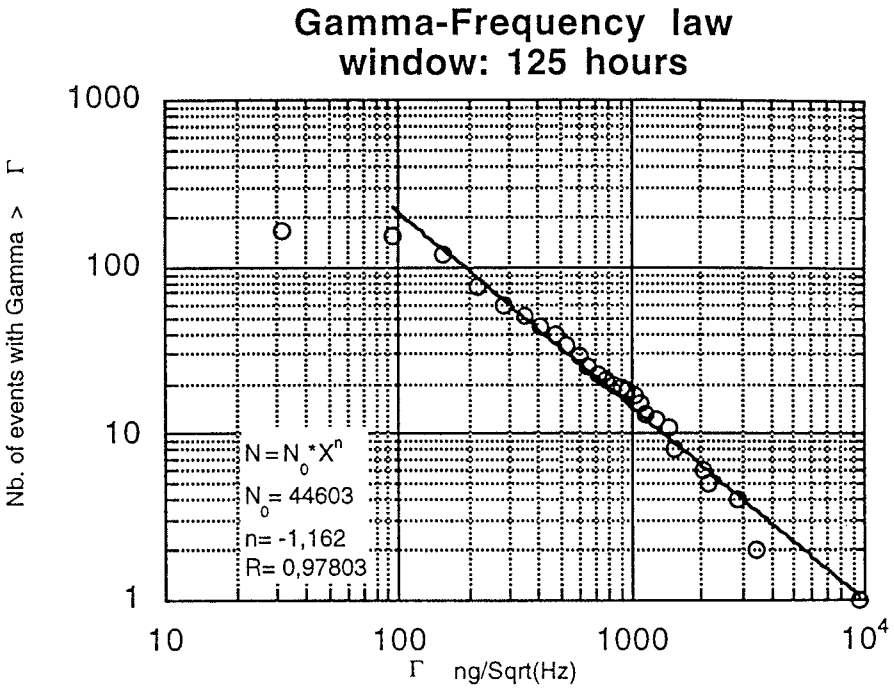

Figure 4: *This plot shows the frequency of occurrence of seismic events at Paranal as characterised by the level of ground acceleration they generate. The parameter Γ is the average level of the PSD of the ground acceleration in the frequency range [10-50 Hz]. The Y-axis is the number of events recorded during the 125 hours of the experiment which exceeded the value Γ. Note that the departure from the straight line at Γ < 100 ng/√Hz is due to the non-completeness of the sample.*

Figure 5 shows an alternative representation of the same statistics. It represents the probability of exceeding a given acceleration level versus this level for different time windows. It shall be reminded that the sample is not complete for the value of Γ < 100 ng/√Hz and Γ > 3000 ng/√Hz and the curves shall not be used in these ranges.

Because of the short duration of the field experiment in comparison to the recurrence times of large earthquakes in the region, which are of the order of 120 years, it is quite clear that the samples collected in this measurement campaign, or the longer time series obtained by the EOPGS from permanent local networks, north of Cerro Paranal, represent only the seismic activity under relatively "normal" conditions. In order to illustrate the effect of a large earthquake on the seismic regime, the Alaskan earthquake (Magnitude 9.2) which occurred on March 28, 1964 was used. This well-documented event, though larger than what could be expected in northern Chile, is tectonically similar and also located in a subduction zone. The long-term seismic monitoring shows that the level of background seismicity can increase by a factor larger than 10 during the first year after the main earthquake and that more than one year may be required to return to a level of seismicity comparable to what existed before the earthquake.

3. Impact of the Natural Seismic Activity on the VLTI

3.1. Description of the method to assess the OPD variation inside the VLT 8-m telescope

With the detailed characterisation of the seismic activity described above, the impact on the VLT (and more particularly the VLTI) can be assessed. We present in the following the computations and the results obtained for the VLT 8-m telescope.

Similar computations are necessary on the VLTI Auxiliary Telescope and on the Delay Line. Less detailed computations were performed for these subsystems during their feasibility studies. The assessment of micro-seismic effects will have to be updated according to their final design, but we anticipate these effects to be less important than on the 8-m telescope, for various reasons.

The goal of the computation is to evaluate the time variation of the Optical Path Length inside the telescope from M1 to the Coudé focus due to mirror vibration. This will be referred to as Optical Path Differences (OPD) in the following.

For that purpose, a detailed Finite Element Model of the telescope was built by F. Koch using substructure models developed by the contractors of the various telescope parts. The model consists of the telescope pier, a complete structural model of the telescope structure including hydraulic bearings and all mirrors and their supports down to the Coudé focus. The model contains 24,000 elements and 95,000 degrees of freedom. It is shown in Figure 6.

The computation consists of the following steps: (i) computation of the transfer functions (or harmonic responses) between an input ground motion in X, Y or Z directions and the displacements of each individual mirror, (ii) computation of the global OPD transfer function corresponding to the above motions using an optical sensitivity matrix, (iii) computation of the PSD of OPD variation by multiplica-

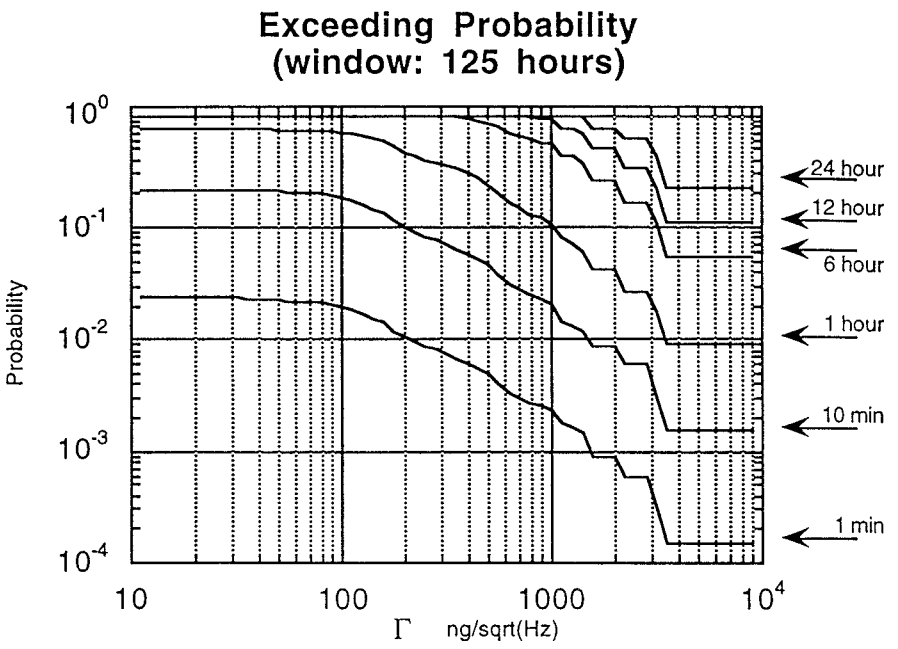

Figure 5: *This plot shows the probability of occurrence of seismic events exceeding a given Γ value during different time windows.*

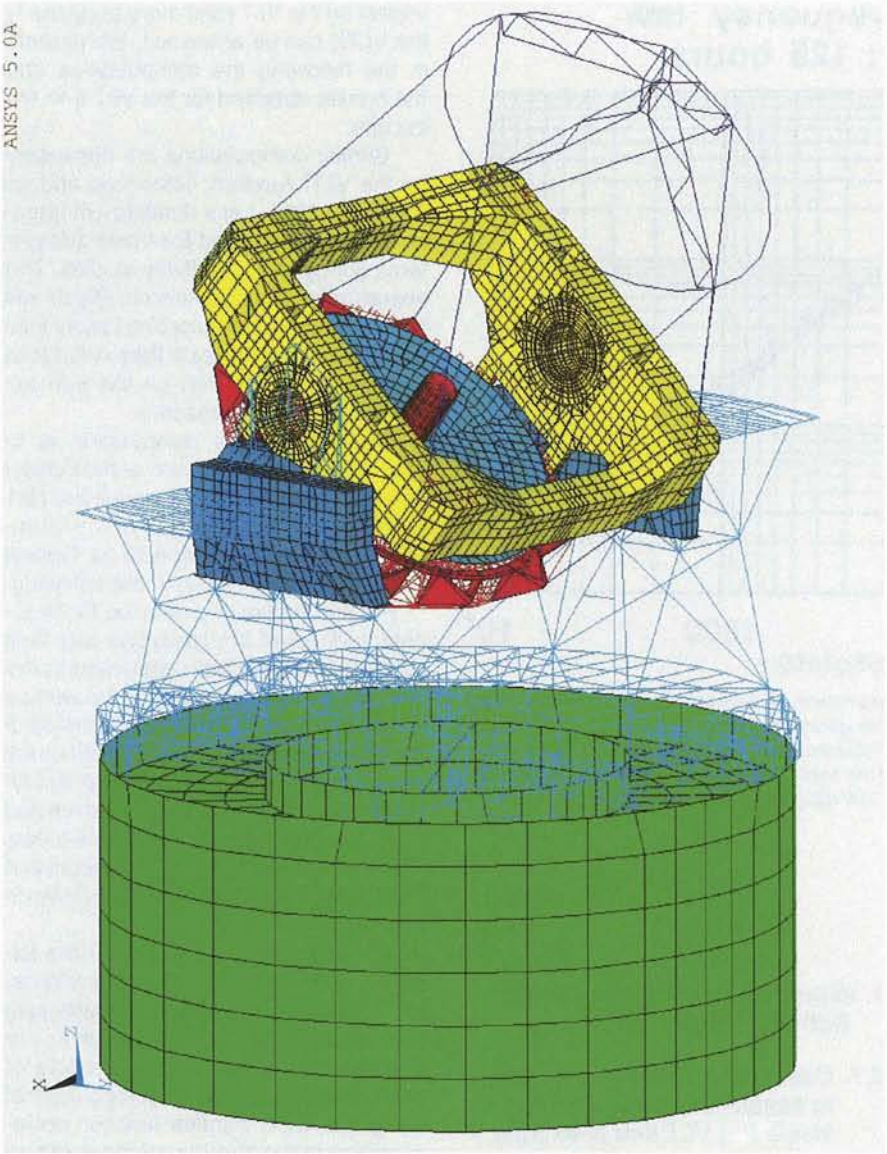

Figure 6: *Finite Element Model of the VLT 8-m telescope used to assess the impact of seismic activity on the VLTI performance. The model consists of the telescope pier, a complete structural model of the telescope structure including hydraulic bearings and all mirrors and their supports down to the Coudé focus. The model contains 24,000 elements and 95,000 degrees of freedom.*

tion of the PSD of the ground motion with the square of the global OPD transfer function, (iv) computation of the OPD variation on a given exposure time by integration of the properly weighted PSD of the OPD.

3.2. Results

Figure 7 shows the OPD transfer functions obtained for each direction of ground motion. The amplification due to the numerous structural modes is clearly visible. The major amplification factors occur in the Z direction (vertical) in the 50 to 70 Hz region. They correspond to the local modes of the supports of the Coudé mirrors M5, M6 and M8.

Figure 8 illustrates, as an example, the effect of the seismic event recorded on March 26 at 03:36 UT. This event has a Γ of 510 ng/$\sqrt{\text{Hz}}$ (i.e. a type of event occurring typically 3 times per night). The resulting OPD variation together with the VLTI specifications is given in Table 1. The specifications are derived from the error budget of the fringe contrast decrease corresponding to different observing wavelengths. The OPD variation under the natural background seismic noise (i.e. in the absensce of any seismic events or artificial sources) is also given for comparison.

This shows that the VLTI performance will be degraded (with regard to the present error budget) for events with magnitude and frequencies of occurrence as given in Table 2.

In case of occurrence of an event larger than the above thresholds, the performance of the interferometer will be degraded for about 1 minute (see Fig. 2).

Figure 5 can also be used to assess the probability of exceeding the above values for given observing windows. For example during an observation of 10 minutes, the probability to exceed the disturbing threshold in the visible, near-IR and IR is respectively ≈ 20 %, 8 % and 2%.

In parallel to the assessment of OPD variations presented above, the impact of seismic events on the image motion at the Coudé focus was evaluated and was found to be negligible; an event of $\Gamma = 510$ ng/$\sqrt{\text{Hz}}$ creates 5 milli-arcseconds RMS of pointing error.

4. Conclusion

The results presented above evidence an important impact of the seismic activity at Paranal on the VLTI performance. The bottom line is that the fringe contrast will be significantly affected, for periods of about 1 minute, by seismic events occurring, on the average, every 40 minutes for observations in the visible and every 1 hour 40 minutes for near-IR observations. Such an impact is not dramatic, but cannot simply be ignored.

TABLE 1.

Exposure time (msec)	10	48	290
Observing wavelength (μm)	0.6	2.2	10
Specifications (nm RMS)	14	50	225
OPD variation under natural background seismic noise (nm RMS)	3	12	72
OPD variation for a seismic event of $\Gamma = 510$ ng/$\sqrt{\text{Hz}}$ (nm RMS)	64	109	119

TABLE 2.

Observing wavelength (μm)	0.6	2.2	10
Disturbing threshold Γ_0 (ng/$\sqrt{\text{Hz}}$)	110	234	964
Period of recurrence of disturbing events	40 min.	1 h 40 min.	8 h

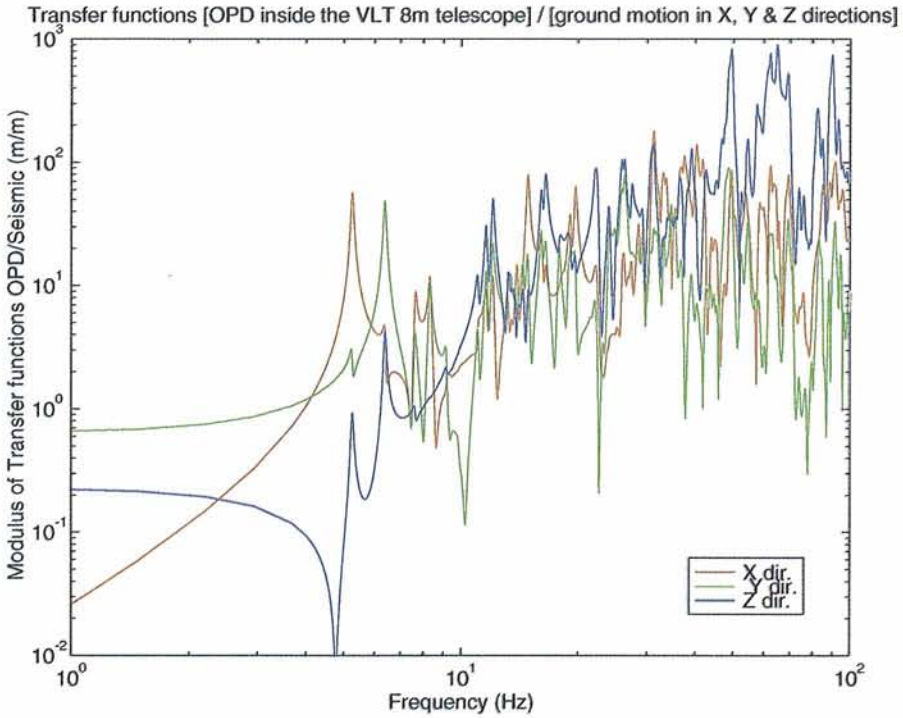

Figure 7: *Transfer functions relating the OPD variation inside the VLT 8-m telescope to an input ground motion. The curves represent the ratio of the OPD over the input ground displacements in X (along altitude axis), Y (horizontal, perpendicular to the altitude axis), and Z (vertical) directions versus the frequency of the displacement. The peaks and valleys are all related to structural modes. The highest amplification factors, driving the final OPD stability, occur at 50 Hz and between 60–70 Hz in the Z direction. They are related to modes of the supports of the Coudé mirrors M5, M6 and M8.*

The immediate consequence is the need to monitor the seismic activity at the site during VLTI operation with the 8-m telescopes. For this purpose, a seismic monitoring system will be included in the Astronomical Site Monitor of the VLT. It will consist of several seismometers monitoring the ground acceleration on the site. They will inform the VLTI Control System of the occurrence of any significant seismic events to allow immediate action to be taken (e.g., close the instrument shutter in case of long exposures) and will store in a data base the recorded ground accelerations to be used during post-processing (e.g., for identification of corrupted snapshot exposures).

A second consequence can be drawn from the detailed analysis of the OPD spectrum resulting from seismic events. The major part of the OPD variation energy over short exposures originates from the excitation of local axial modes of the support of mirrors M5, M6 and M8 in the Coudé train of the 8-m telescope and not from global modes of the telescope structure. This means that optimisation of these supports by increased stiffness or damping shall be considered during their final design and that improvement of the results presented in this article may be expected.

The third consequence concerns a metrology system based on laser interferometer and accelerometers which could be developed to monitor in real time the OPD variations inside the telescope in view of their correction with the PZT-mounted secondary mirror of the VLTI Delay Lines. In fact, such a system has been considered since the early stage of the VLTI project, and provision has been included in the design of the telescope to allow, if necessary, its future implementation such as a space for a retro-reflecting device at the centre of the secondary mirror. Even though the studies of other disturbances such as wind load, artificial vibration sources, etc. have shown that such a metrology is not essential, the present results indicate that it is prudent to study its feasibility and its design in order to allow its quick implementation if it appears necessary and feasible.

As a last consequence, we can wonder if the early knowledge of the results of such a detailed analysis would have impaired the selection of Paranal as the VLT/VLTI site. Indeed, the loss in observing time due to microseimic activity (1 min./40 min. = 2.5 % in the worst case) remains negligible with regard to the gain (up to 200 %) due to improved seeing and cloud conditions (see VLT Report No. 62).

For further information please contact:
B. Koehler, ESO-Garching.
E-mail: bkoehler@eso.org, Tel:
+40 (89) 320 06 515, Fax: +49 (89) 320 23 62.

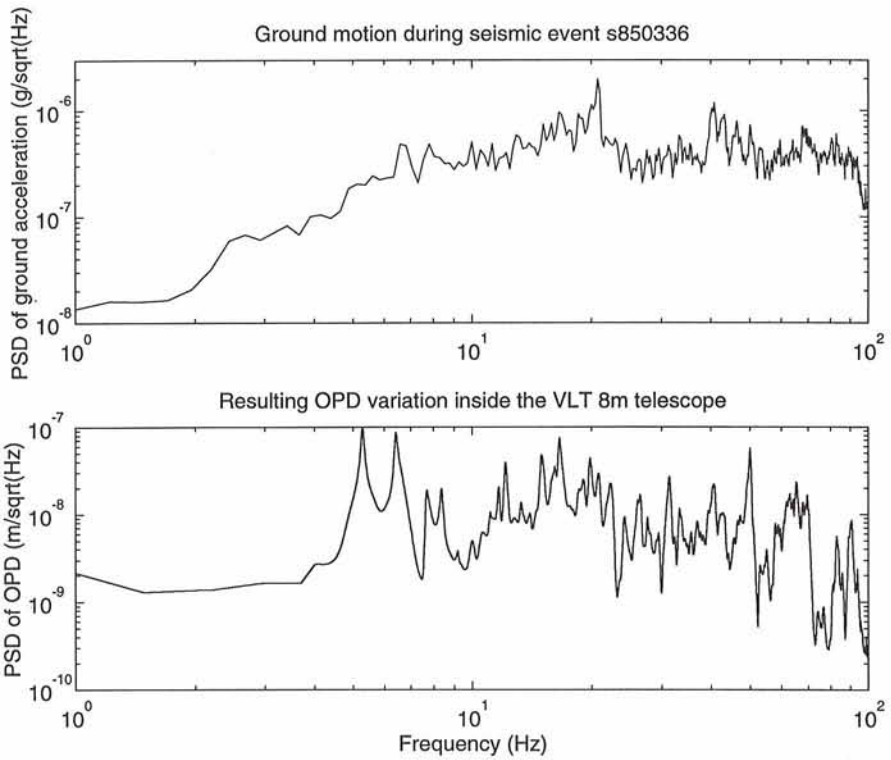

Figure 8: *Effect of a seismic event on the OPD variation inside the VLT 8-m telescope. The event was recorded on March 26 at 03:36 UT. It is a type of event occurring typically 3 times per night. Upper: Power Spectral Density (PSD) of the ground acceleration measured at Paranal. Lower: PSD of the resulting OPD inside the telescope.*

NTT BITS & PIXELS

With this periodically compiled collection of short notes, the NTT Team intends to keep the community informed about changes in performance, configuration, and operation of the NTT and its subsystems.

New NTT Support Astronomer at La Silla

With the arrival of Griet van de Steene on February 1, the NTT Team received some further reinforcement. As a support astronomer at La Silla, she will help Visiting Astronomers with the usage of EMMI and SUSI and also periodically assume the function of the NTT Coordinator.

Griet is Belgian and obtained her master's degree in Gent. Thereafter she moved to Groningen where she worked on the problems of the incompleteness of catalogues of planetary nebulae and the PN distance scale and recently received her PhD from the Rijksuniversiteit there. The NTT Team cordially welcomes her to a busy but exciting job.

Rotator Stops Stopped!

During the last year, the single most important reason for losses of observing time were sudden stops of the instrument rotators, a nuisance which had been around for years. The two most severe problems could now be identified and eliminated.

On side A the problem was that the rotator would stop with accompanying error messages "Power amplifier not ready". It could be traced back to the interface between the ETEL-supplied control system for the amplifier and ESO's control system. The response time of the ETEL system was so short (msecs) that narrow but sufficiently high noise spikes were interpreted as stop commands. Filtering of the input signal has brought this behaviour to an end. Jean-Michel Moresmau's help with the analysis is much appreciated.

On side B the rotator would also stop but *without* any error message. Similarly to the problem on side A, this one was due to noise which made the VME believe that the rotator brake had been engaged manually. Consequently, the software stopped the rotator and disabled the motor driver without issuing an alarm message since the supposed manual intervention could not be assumed to be anomalous. Filtering of the input signal suppressed this problem, too.

Image Analysis and Active Optics Systems

Preparations continued for the implementation of the continuous image analysis in parallel to the scientific exposures. This had been integral part of the initial design of the NTT but was never fully implemented. The offsets between the telescope focus positions inferred from the image analysis and focus exposures taken with one of the scientific instruments have been calibrated for sides A and B. A bug in the field curvature compensating software for the trombones has been identified due to which the focus of the guide probes varies with position in the field. The minimum flux of the guide star of which 80 % are used for the image analysis has been measured. Image shifts induced by lateral displacements of M2 (to correct for decentring coma) were measured and found to be virtually negligible. Extensive tests of the continuous closed-loop operation will take place in February. Once implemented, this operation mode will keep the optical quality of the NTT permanently as close to the optimum as possible and finally make the NTT a truly active telescope.

Telescope Optomechanics

Gerardo Ihle has kindly undertaken precision measurements of the flexure of the telescope as a function of zenith distance. The most important component of the flexure is fully elastic. This is consistent with image analyses performed at different telescope elevations. It opens the possibility to establish, by analogy to pointing models, an active optics model so that the residual corrections to be measured and applied in closed loop are accordingly smaller.

Other tests indicate that M1 may be under permanent stress from its lateral supports which furthermore varies with zenith distance. The resulting deformation of the mirror may not follow one of its natural modes. But astigmatism would not be orthogonal to it, and astigmatism has, in fact, often been found to vary significantly with telescope position. This will be further investigated during tests in February as it may have a bearing on the frequently reported elongated images of point sources.

Further Field Tests of VLT-Like Control Software

In January, the first part of Work Component 4 of the NTT Upgrade Plan was successfully completed. Functionally, it concerned the control of the calibration units and on side A (IRSPEC/SUSI) the autoguider. The real objective, however, was to test the VLT Common Control Software (CCS). A few minor problems with the CCS were discovered. However, their effects could all be worked around on-site, and the conclusion is that the CCS is already in good shape. Feed-back to the VLT Software Group has been formally filed in the form of six SPR's. Test observations showed no difference in performance.

An interesting by-product of some observations has been obtained by Stefano Benetti during the first night when the new control system of the autoguider was not yet fully installed: For exposure times up to 15 minutes and not too extreme telescope positions he also found no significant difference between observations obtained with and without autoguider. Given the much improved pointing which is based on exactly the same software as the telescope tracking, this is no surprise.

New-Generation CCD Controller Tested on EMMI

Also in January, the prototype of ESO's new-generation controller, ACE (Array Control Electronics), was tested on the blue arm of EMMI. This was a test of the entire system that will be used for the FORS and UVES instruments on the VLT; the system includes ACE, the LCU (local control unit), the WS (workstation) and the new modular dewars. All individual modules performed well and the system as a whole demonstrated that the fundamental design is sound.

During 1995, modifications will be made in the hardware and software to prepare for the FORS and UVES instruments. The question of when this system could be installed on the NTT is being

discussed with the newly-formed optical detector group.

An article is in preparation for the next issue of *The Messenger* to provide a detailed description of the controller system and the results of the January test.

New Field Lens Installed in Red Arm of EMMI

The 2k × 2k Tektronix CCD which in February 1994 was installed in the red arm of EMMI has a significant intrinsic curvature. As a result, the focus would be constant only in concentric annuli. Now, a new field lens has been installed which compensates the axisymmetric part of the non-flatness of the detector. The results are described in a separate article in this issue of *The Messenger.*

During the tests it was furthermore confirmed that a lens in the red camera probably is not properly cemented and has some play. Image shifts of the order of 1–2 pixels may occur as the rotator position angle of EMMI changes.

Straylight in EMMI's Echelle Mode Eliminated

Observer Sandro D'Odorico found that the long-known problem of straylight in the echelle mode of EMMI was actually due to external light leakages or an internal parasitic light source outside the beam. The symptoms of this problem could, therefore, be quickly cured by adding some extra light baffles. The investigation of the actual origin of the straylight continues. For observations of faint sources the achieved reduction in effective system noise can be quite significant.

Further Steps Towards Automatic On-Line Data Reduction

The capability to associate incoming calibration frames with science exposures and vice versa has been added by Michele Péron to the MIDAS Data Organizer. Default association rules have been defined for EMMI and SUSI which, however, can be fully customized. This will make the task of the observers much easier as they no longer have to do much tedious bookkeeping when reducing the data.

As a first step towards automatic exploitation of the association table provided by the Data Organizer, Rein Warmels has interfaced the MIDAS CCD package to it. In its present installation, the observer still has to trigger the reduction process in order to exclude unwanted interference with the data acquisition. However, thereafter the reduction is fully automatic and includes the averaging of multiple calibration exposures, bias subtraction, flatfielding, etc.

The next stages such as flux calibration for on-line magnitudes or the extraction of wavelength-calibrated spectra are in preparation.

More Space on Faster Disks

Two fast wide SCSI disks of 4 Gbyte each were attached on workstation insntt where observers perform the online analysis of their data. The loading of a new CCD frame now takes only 2 seconds as compared to 9 seconds before.

The installation of IRAF is now foreseen for February.

Logging of Temperatures and Windspeeds Within Enclosure

Various temperature sensors and anemometers have been installed. The measurements are merged with the telescope operations log files which are transferred daily to the ESO Archive. The Archive will also make them available to archival users of NTT data. The more immediate aim is to build up an empirical database which can be compared with model computations for the windflow within the enclosure. From this comparison and its correlation with actual seeing data, an operations model for the enclosure will be developed which should permit the dome seeing to be minimised.

Graphical User Interface to IRSPEC Package in MIDAS

Now that also IRSPEC data are routinely transferred to a workstation, a graphical user interface to the IRSPEC reduction package in MIDAS has been added. This makes the on-line quality control and reduction of IRSPEC data quite effective. Meanwhile this user interface has been made available as part of the 94NOV release of MIDAS and can, therefore, also be used for off-line work. Cristian Levín is to be thanked for the development effort.

Eightfold Throughput Improvement for Remote Observers Confirmed

The improvements which in the previous issue of *The Messenger* were announced to result from the coming into operation of the new 2 Mbit/s roof-to-roof link have meanwhile been confirmed during a number of remote observing runs performed from Garching. The system also seems to be very stable. The efforts of Joar Brynnel, Michael Fendt, Manfred Mornhinweg, Charlie Ounnas and Manfred Ziebell in making this system operational are gratefully acknowledged.

Improved Reliability?

One of the stated aims of the NTT Upgrade Project is to improve the reliability of the NTT. Only 10 months after the start of the project it is certainly too early for any conclusions. But we are delighted to report that the start into 1995 was a very encouraging one: During the month of January, only 2 times 20 minutes of observing time were reported lost by the observers (a terminal caught fire, and EMMI's slitwheel got stuck). Thirteen of these 31 nights were used for a large variety of tests (cf. above) which in the past would often have put the system under considerable stress, provoking a variety of problems. Even after subtraction of these 13 nights, the fraction of the time lost between astronomical twilights does not amount to more than 0.5 %.

For further information please contact:
D. Baade, ESO-Garching,
e-mail: dbaade@eso.org

New Power for the Danish 1.54-m Telescope

J. ANDERSEN, M.I. ANDERSEN, J. KLOUGART, P. KNUDSEN, H.H. LARSEN, N. MICHAELSEN, R. FLORENTIN NIELSEN, P. NØRREGAARD, E. OLSEN, P. KJÆRGAARD RASMUSSEN, K.E. SEIFERT, H. JØNCH-SØRENSEN, Copenhagen University, Denmark

Meeting New Challenges

After more than 15 years of intensive use, the Danish 1.54-m telescope on La Silla and its equipment are undergoing a major overhaul. The goal of this joint effort with ESO is to provide a more powerful research tool, updated to reflect changing scientific priorities. It will be armed with a couple of core instruments, permanently mounted and requiring a minimum of effort in operation and maintenance.

On January 20, 1995, we passed a major milestone in the upgrade project with the installation of several new features, chief of which is the new DFOSC (Danish Faint Object Spectrograph and Camera), patterned after ESO's very successful EFOSC instruments and equipped with a thinned Loral 2048 × 2048 CCD with exceptionally high quantum efficiency (QE). Also, a simple mirror cooling system was installed which will hopefully lead to an improved image quality. In this article, we briefly describe the DFOSC and its capabilities and our plans for the next steps.

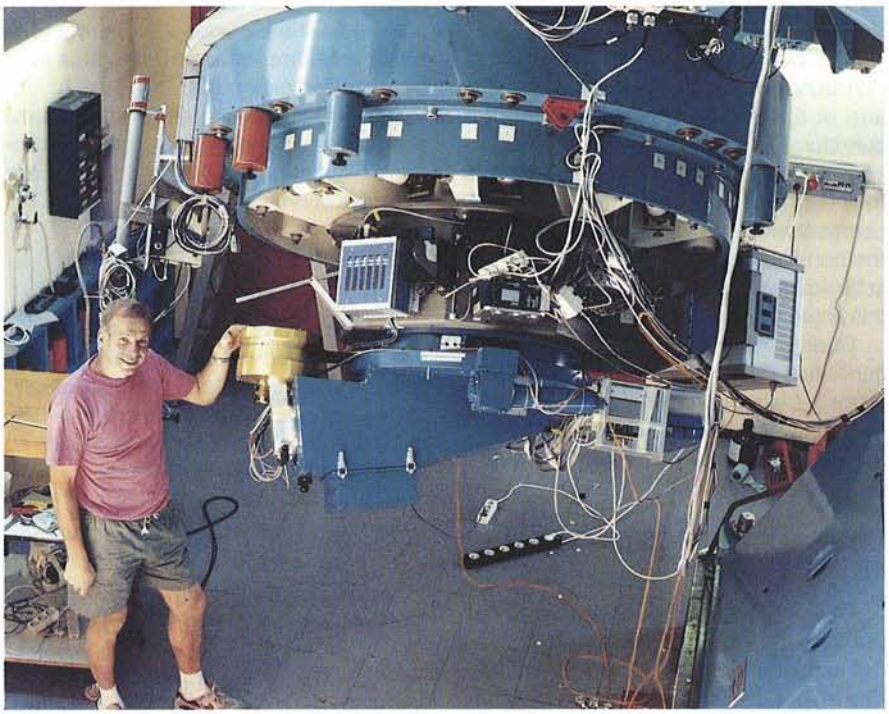

Figure 1: *DFOSC and the new CCD camera mounted on the telescope.*

The DFOSC

In choosing our new workhorse, scientific goals, the main strengths of the telescope, and the capabilities that do or will exist elsewhere on La Silla must all be considered. A future main class of research for a 1.5-m telescope on La Silla will be searches for and spectroscopy of faint objects, in stand-alone programmes or in preparation for studies with the VLT. Its wide-field Ritchey-Chrétien optics makes the 1.54-m particularly suited for such work. The EFOSC design (cf. *The Messenger* 38, 9) offers an elegant way to match a large optical field to available CCD detector formats, providing a maximum of observing modes with a minimum of operational effort. Therefore, and with the kind collaboration of Bernard Delabre of ESO, the DFOSC optical design is based on the EFOSCs, adapted to the 1.54-m environment.

With a single 2K × 2K CCD – as ambitious as our modest resources and the optical properties of the design were likely to allow – and an optimum final pixel size of 0.″4 (15 μm), the full field covered by the instrument is 13.′7 × 13.′7. Selecting a 30-mm collimated beam then fixes the main optical parameters. A prism with total internal reflection bends the light path almost parallel to the primary mirror, giving a compact instrument with minimal operational constraints (see Fig. 1).

Filters and grisms are introduced in the parallel beam via two wheels and are easily exchangeable from the bottom of the instrument. Thus, one can change from direct imaging in a variety of passbands to spectroscopy with a range of resolutions (Table 1) in a few seconds. In the telescope focal plane, aperture plates with long slits, multi-slits, or test patterns can be inserted in an aperture wheel; a small CNC machine allows quick fabrication of customized aperture plates for multi-object spectroscopy. The entire instrument rotates about the telescope optical axis so that long slits can be placed in the desired orientation, and it is operated from a workstation in the control room. The basic DFOSC was commissioned by ESO in November 1994.

In January 1995, the final CCD camera was added, and a new, user-friendly filter and shutter unit (FASU) was installed in front of the DFOSC. The 90-mm filters accommodated here cover the full field for applications, e.g. narrow-band interference filters, where filters mounted in the collimated beam (and tilted 6° to avoid ghost images) would introduce a significant field gradient in the passband.

The CCD Detector

As mentioned above, DFOSC is designed to use a 2K × 2K CCD with 15-μm

TABLE 1. DFOSC grisms data. RS is the resolution-slit product. Data for the echelle grisms are given for 13th (#9) and 3rd orders (#13).

Grism No.	Blaze (Å)	Dispersion (Å mm^{-1})	RS
3	385	179	640
4	495	220	700
5	670	220	870
6	385	110	990
7	515	110	1300
8	725	88	2200
9	520	26	4300
10	415	460	230
11	510	340	390
12	730	910	200
13	545	36	4200

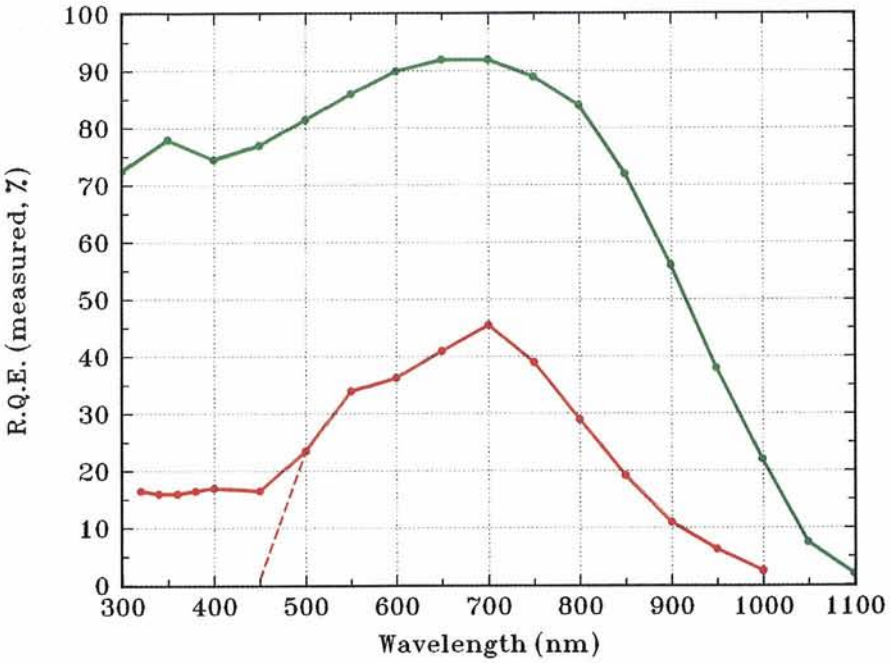

Figure 2: *Measured quantum efficiency of the thinned DFOSC CCD (green), compared to a typical thick Loral CCD (red; dashed: uncoated).*

pixels. The chip now mounted is the 3-side buttable version designed by John Geary (SAO) and fabricated by Loral Fairchild. In order to enhance sensitivity, especially in the blue, it was thinned by Michael Lesser (University of Arizona) and coated with a two-layer anti-reflection coating (HfO_2 + MgF_2). A simple UV flooding procedure is needed for optimum QE if the chip is warmed up to room temperature.

Figure 2 compares the actual, measured QE with that of a typical thick, coated Loral CCD. As will be seen, it is remarkable indeed. In fact, in the UV, the gain over the thick chip is quite comparable to that from a 3.6-m to one of the VLT 8.2-m unit telescopes!

As can be seen in Figure 1, a special shape of dewar is needed to avoid collisions with the telescope or pier when the telescope moves around and DFOSC is rotated about its axis. This special camera was constructed in our laboratory and equipped with a CCD controller and data acquisition system also developed there. Measured readout noise with the thinned Loral CCD is about 7 e^- rms, dark signal about 2 e^- $pixel^{-1}$ s^1 at –100 C (MPP mode), linearity very good up to near the saturation limit of about 85,000 e^- $pixel^{-1}$ (also in MPP mode). CTE and cosmetics are excellent, and crosstalk between the two amplifiers negligible. Pixel binning in X and Y and readout windows are easily selectable from exposure to exposure. Using both amplifiers, the full chip is read out and the data stored on the workstation disk in FITS format in 45 seconds, ready for processing.

Performance

During the nights January 20–26, 1995, a large number of tests were made of all operational aspects of the instrument. The detailed results will be given in a technical report when all the data have been properly reduced. To give readers a first impression of the new capabilities of the telescope, we show in Figure 3 a direct exposure of the 30 Doradus region in the Large Magellanic Cloud. In addition, Table 1 gives approximate count rates for grism spectroscopy; these numbers are subject to revision after the final data reduction.

In the cryostat window of the new CCD camera, doubling as the DFOSC field flattening lens, the original, slightly radioactive BK7 glass has been replaced by fused silica. The result is a tenfold reduction in cosmic-ray-event rate.

Future Plans

Our plans for the future have as one goal to integrate the new ESO Telescope Control System with the controls of the new adapter, the FASU, the DFOSC, and the CCD through one convenient user interface, so the observer can easily control all functions that are essential from his/her point of view (field to be observed, filters, exposure times; focus or calibration sequences, etc.), and the

Figure 3: *A 4-minute exposure of the 30 Doradus region in the Gunn r band, taken on January 20, 1995, with DFOSC and the new CCD camera.*

TABLE 2. Count rates (e^- s^{-1} $Å^{-1}$) for monochromatic magnitude $m_\lambda = 12.0$.

λ (nm)	Grism #6	Grism #7
350	41	–
400	69	52
450	56	59
500	48	61
550	–	58
600	–	52
650	–	48

data are transferred seamlessly and with all necessary header information right into the observer's favorite image-processing system.

Another important goal is to add a direct CCD imaging option. Finer sampling is needed to yield the best spatial resolution on nights of good seeing (which will, we hope, be more frequent with the new mirror cooling system). Also, focal reducing optics are not always optimal for precision field photometry. Therefore, we plan to install, perhaps in early 1996, a direct CCD of the type described above in a stand-by position in the adapter, fed by a 45° mirror and with rapid tip/tilt correction for atmospheric image motion. At 0.″23 per pixel, this should be a valuable high-resolution imaging option, always readily available when good seeing occurs.

Moreover, a fiber-feed position is foreseen in the adapter, so an off-telescope instrument can be permanently connected, eliminating changeovers and improving instrument stability. Options under study include the radial-velocity scanner CORAVEL or (better) an optimized, bench-mounted échelle spectrograph.

Finally, much remains to be learned about the optimization (including UV flooding), testing, maintenance, and operation of high- performance CCD detectors. We look forward to continuing our pleasant cooperation with the ESO Optical Detector Group in this area, to the benefit of both sides – and our users.

Acknowledgement

The DFOSC, CCD development, and telescope upgrade projects were made possible by generous financial support from the Carlsberg Foundation and the Danish Natural Science Research Council.

For further information please contact:
J. Andersen, Copenhagen University, Denmark, e-mail: ja@bro835.astro.ku.dk

A New CCD Field Lens in EMMI Red Arm

R. GILMOZZI, B. DELABRE, S. D'ODORICO, J.-L. LIZON, O. IWERT, P. GITTON, S. DEIRIES, ESO-Garching

The ESO Multi-Mode Instrument EMMI was first installed at the NTT in the summer of 1990. At that time the red arm was equipped with a thick CCD with UV-blue sensitive coating because the originally planned thinned 2048^2 detector had not become available. At the beginning of 1994 (see *The Messenger* No. 76, p.15) a 2048^2 thinned SITe CCD was finally installed on the instrument with its dedicated camera. One last step was however still necessary to fully realize the planned optical quality of the instrument. The sensitive surface of the CCD delivered to ESO proved to be convex with a peak at its centre in the direction of the camera. The curvature is due to the CCD assembly process and it is well approximated by a paraboloid. The difference between centre and corners is approximately 200 μm and resulted in a higher dispersion around the average value of the image quality in the field of view, with a significant degradation in the corners. A new field lens, to serve also as window of the cryostat, was computed to compensate for this curvature and it has been installed and tested in three nights in January 1995.

Image quality has been determined through observations of several star fields (either outer regions of globular clusters, or open clusters) in order to determine the best centring position for the field lens. One important point to realize is that image quality can be really assessed only through astronomical observations performed in good seeing. NGC 2204 appeared to be the best choice in terms of uniform star distribution. After several iterations of fine-centring the lens, an image of 0.57″ was obtained (i.e. just above the critical sampling for the 0.27″ pixels of the camera). Although a 10 % variation was visible between centre and edges of the field of view, this demonstrated that the performance of the lens allows us to

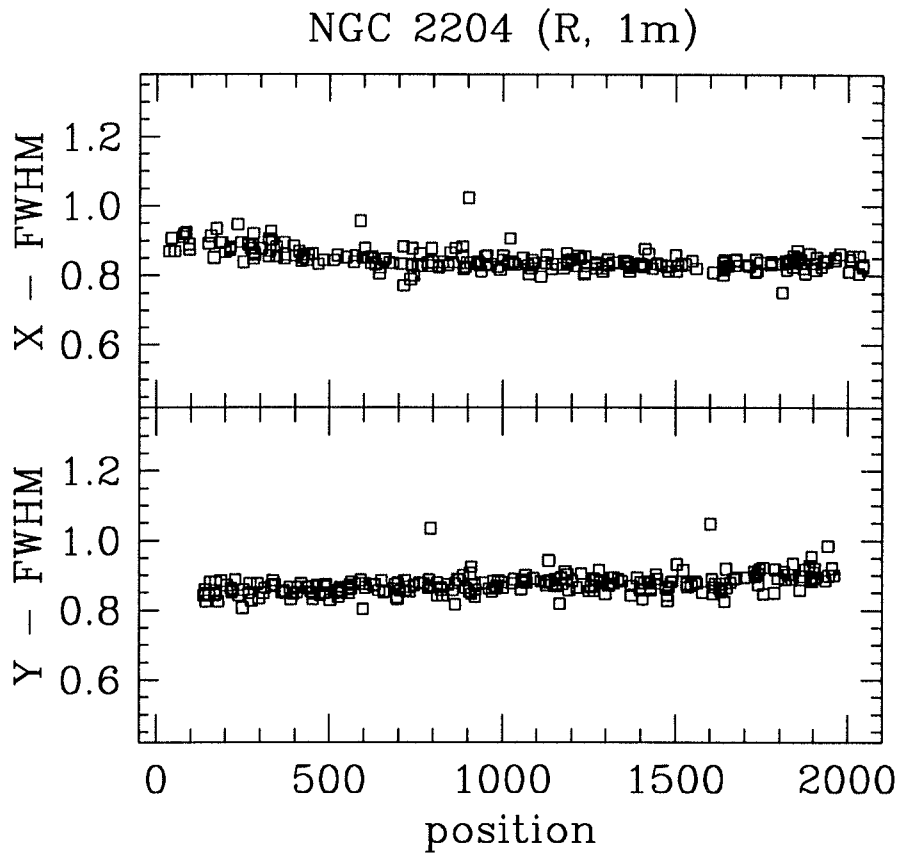

Figure 1: *Distribution of the stellar FWHM as a Function of position.*

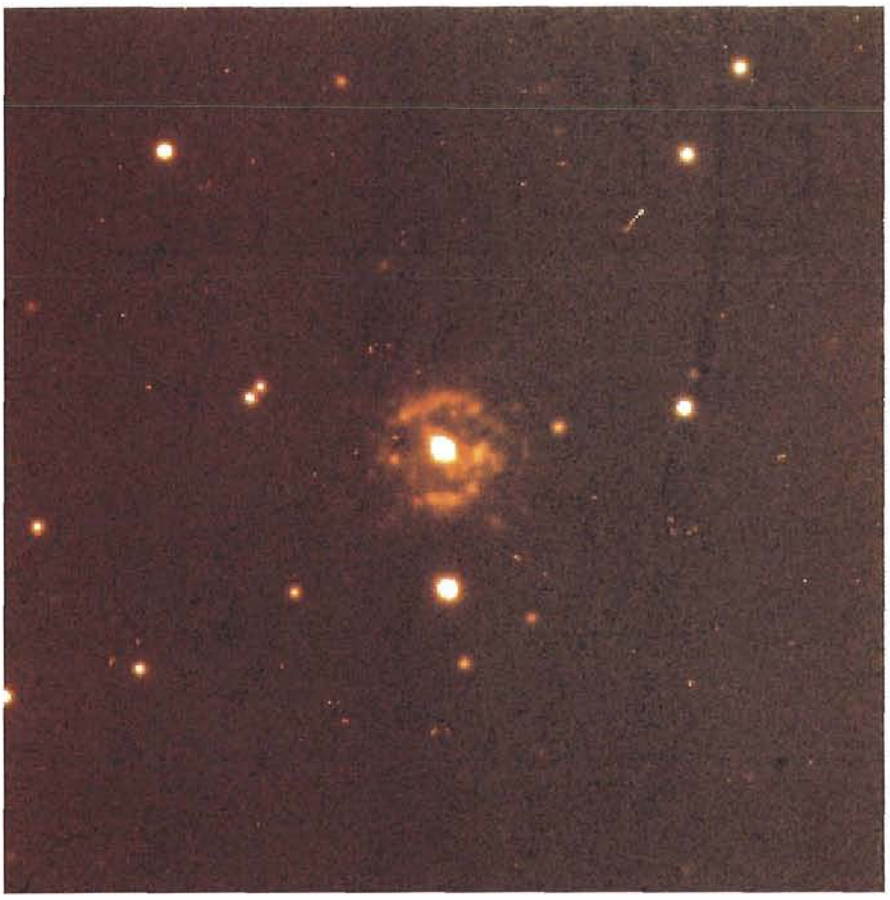

Figure 2: *40-min Hα image of the recurrent nova T Pyx in 0.7" seeing. The image is 80" × 80".*

A preliminary value of the plate scale was obtained by comparison of a 2' × 2' image portion with an HST WFPC2 image for which astrometry was available. Though a determination of the plate scale based on the full field of view will be produced, the derived value of 0.2698± 0.0002 arcsec per pixel shows that the new lens has not introduced any substantial changes. However, users should be aware that images taken prior to the lens change cannot be used as they are for preparing MOS plates: a scale change of 8% is present between images taken before and after the replacement. Old and new images can be successfully coadded if the old ones are rebinned by 0.99187.

The efficiency of the camera has also not changed with respect to the value prior to the installation of the new lens (to within the uncertainties): the numbers of $e^- s^{-1}$ for a 15^m A star are 20,600 (V), 24,000 (R), 12,700 (I), to be compared with the previous 18,900 (V), 22,000 (R), 11,900 (I) (J. Storm 1994).

Focusing of the telescope should be preferentially done in the inner 1000×1000 pixels of the frame, since the focus wedge gives, at the edges, a large dispersion of values.

We also tested the stability of the image quality over longer integrations, with results very similar to those of Figure 1.

reach an image quality close to the best seeing values ever measured at the NTT. Figure 1 shows the variation of the Point Spread Function as a function of position for the best (and final) lens position (NGC 2204, R filter, 1 minute integration). The average value of the FWHM is 0.84 (0.87) ±0.02 arcseconds in x (y) – of course, the 0.57″ seeing would not last!

A very small effect at the edges of the chip is still present (of the order of 5 %), but it is not clear whether it is due to the new field lens: during the tests it became apparent that both the position of the rotator and the zenith distance can affect the image quality (for a discussion of the latter effect, which is also the cause of the slight ellipticity of the star images and which will be further analysed – and possibly corrected – in February, see "NTT Bits and Pixels" in this issue). In the worst case, these effects can amount to at most 10–15 % at the edge of the field of view, a value still quite acceptable, especially in view of the very large field of view of this camera (9' × 9'). A more thorough analysis of the dependence on rotator position of the instrument flexure and of the camera triplet (see "NTT Bits and Pixels") will be performed in the near future in order to quantify and understand these effects and to try to reduce even further the spread of the FWHM as a function of position.

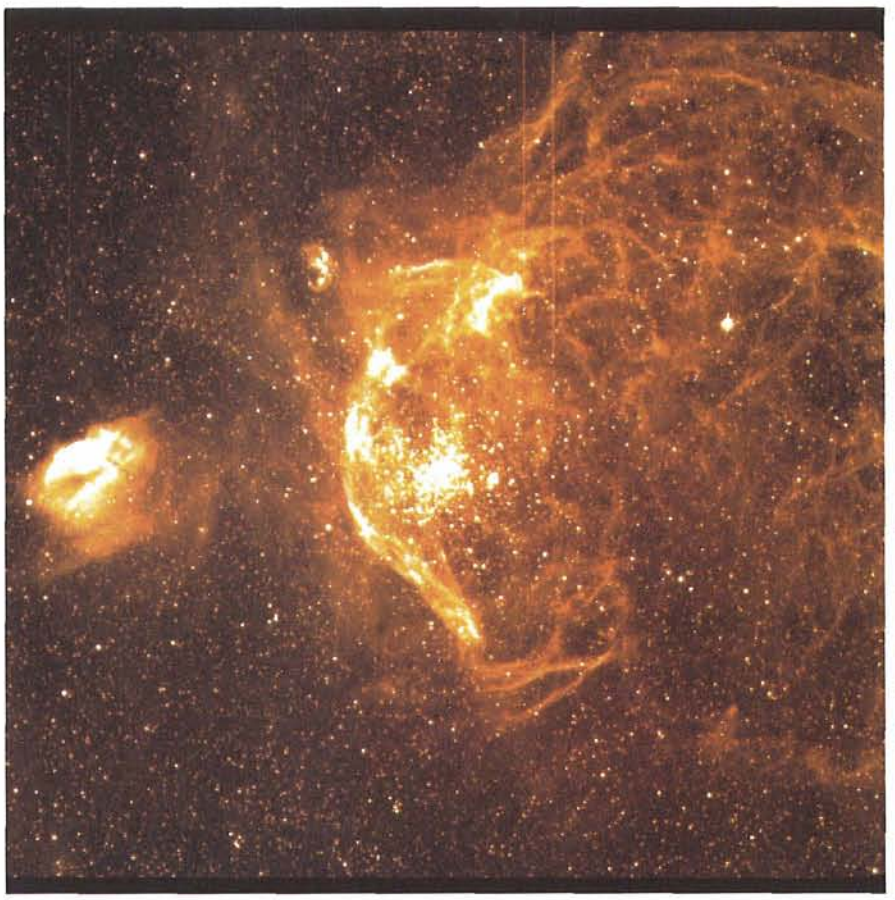

Figure 3: *Full field of view (9' × 9') image of NGC 1850, a young double cluster in the LMC, in the light of [NII]. The filamentary structures are most likely supernova remnants.*

Figure 2 shows a 40-minute Hα image of the recurrent nova T Pyx. The FWHM of stellar images is 0.7″, one of the best ever attained for such a long exposure time through a narrow-band filter. The image shows in exquisite detail the debris from a previous outburst and will be used together with spectral information to determine to which historical outburst the surrounding material refers, and hence to derive a new, better estimate of the distance. Figure 3 is a 0.9″ seeing, 30-minute [NII] image of the young double cluster NGC 1850 in the LMC and shows extended filamentary emissions around the cluster. These are very likely the remnants of supernova explosions in the main cluster, which is only 50 million years old. Shock waves from supernova explosions were invoked as the probable cause of the formation of the much younger companion cluster (*Ap. J. Lett* 435 L43.

For further information please contact:
R. Gilmozzi, ESO-Garching,
e-mail: rgilmozz@eso.org

Ghost Analysis and a Calibration Database for the Long Camera of the CES

L. PASQUINI, H.J. ARAYA, ESO-La Silla

1. Introduction

We present recent improvements and changes at the CAT and CES, mostly performed during the telescope idle period in September 1994. We also describe a new calibration database which has been installed in La Silla computers and an analysis of the ghosts found in our extensive tests.

2. CAT Telescope

The floor of the CAT dome was in a bad shape and unsafe for observers and night assistants. The floor panels were replaced.

The CAT telescope and the CES spectrograph were re-aligned and the primary mirror of the telescope adjusted. This intervention was requested to improve the CAT optical quality, in particular to minimise coma; with this intervention also a more stable and accurate pointing model has been achieved.

3. CES Spectrograph

Due to a major technical problem (abnormally high read-out noise) on CCD #30, mounted on the CES Long Camera, this was replaced by CCD #34 in October 1994.

The CES spectrograph was used, in combination with the Long Camera and CCD #30, to acquire a full set of calibration spectra. 140 Th-Ar and Flat Field calibrations were recorded with the RED path covering the range between 8990 and 5215 Å, while 80 frames were acquired with the BLUE path covering the 5200–3790 Å domain. In Table 1 and 2 a summary of the wavelength interval steps used in the RED and BLUE path is given.

The aim for the acquisition of the calibration data set was twofold:

(1) To allow an analysis of the spectrograph ghosts present in the wavelength domain commonly used by the observers.

TABLE 1: Summary of central wavelengths and steps used for the calibrations in the RED domain.

λc Beg	λc End	Step (Å)
8890	8500	70
8435	8110	65
8050	7330	60
7275	6670	55
6620	6070	50
6025	5925	50
5880	5340	45
5295	5215	40

TABLE 2: Central wavelengths and steps used for the calibrations in the BLUE domain.

λc Beg	λc End	Step (Å)
5200	4520	40
4485	4030	35
4000	3790	30

(2) To provide the potential CES users with a complete set of calibration data, to be used to better planning their observations.

We note that, although the presence of ghosts is known to be more serious when using the CES in combination with the Short Camera, we have preferred to perform the calibration set with the Long Camera, mainly because, as soon as a new thinned detector will be available at La Silla (March 1995), the Short Camera will be decommissioned and only the Long Camera will be offered to the users.

The spectra were acquired with a nominal resolving power R =10^5 and a decker height of 5 arcsec. Although the CES users are recommended to use a longer decker, a short decker was preferred because this facilitates the separation of those Flat Field (FF) ghosts falling close to the science spectrum.

The central wavelengths of the calibration frames were chosen to ensure some overlap between adjacent spectral ranges. The FF exposures integration times were selected to give a peak intensity level around 10,000 ADU (one ADU corresponds to 2.8 electrons in the used configuration) in the extracted spectra, and the intensity maximum typically varies between 6000 and 14,000 ADU after extraction. Only at very blue wavelengths (i.e. below ~ 4000 Å) lower exposure levels were obtained, because the maximum duration of the FF exposures was fixed to two minutes.

Th-Ar integration times were set to obtain a level of at least 10,000 ADU in the strongest lines of the extracted frame.

One-dimensional spectra were extracted over a slit of 13–14 pixels, almost the whole slit height.

Because these frames may be very useful for the CES users to prepare their observing runs and calibrations, they are made available to the users' community. Both the original (2-dimensional) and the extracted (1-dimensional) files are stored as FITS files; they can be accessed and copied through ftp with the following commands:

```
ftp 134.171.81.6
username: anonymous
password: your ident as password
cd pub/ces/calib
get README
binary
get Mλc.ND
```

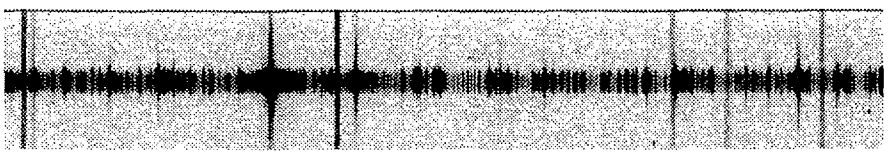

Figure 1: *Two-dimensional image of the Th-Ar exposure centred at 6470 Å.*

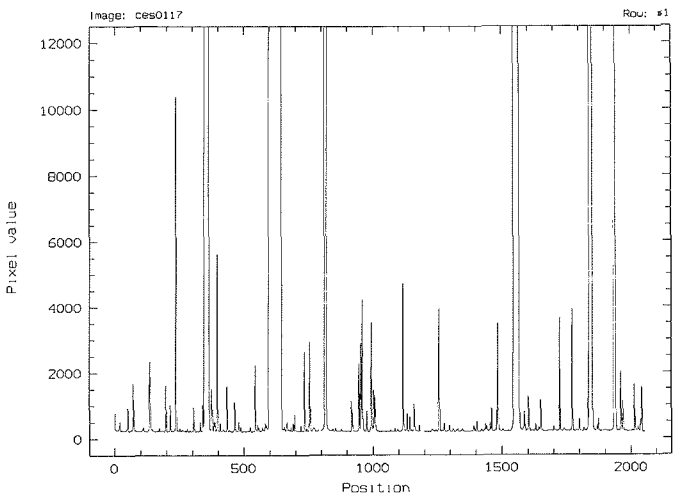

Figure 2a: *Extracted spectrum of the Th-Ar exposure centred at 6470 Å.*

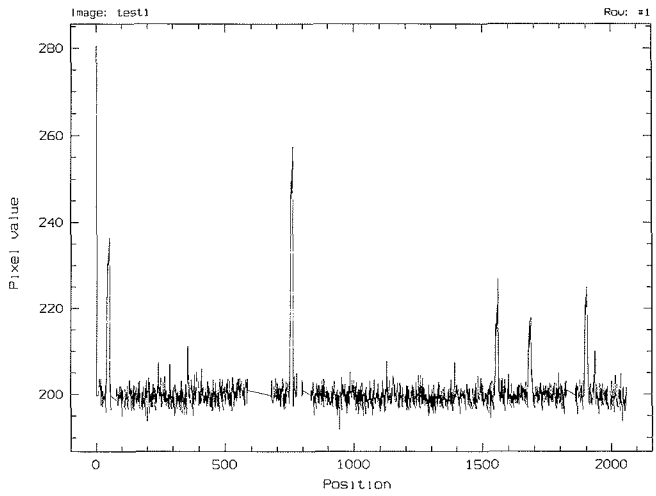

Figure 2b: *Ghost spectrum for the same region as in Figures 1 and 2a.*

After the transfer has been successfully completed, you may exit with

quit

The labels describe: M = FF or TH for Flat Field and Th-Ar exposures respectively

λc the central wavelength (in Å)

N = 2 or 1 respectively indicate the two- or one-dimensional files.

As an example, FF5415.2D will be the two-dimensional Flat Field frame at 5415 Å central wavelength. The names of all the stored frames are given in the README file, which also contains suggestions and advices for the use of the database.

The extracted spectra can be used by the CES users and by the technical crew to monitor the calibration procedures, the ageing of the lamps as well as the functioning of the neutral density filter wheel.

Note that complete descriptors (including integration time and neutral density filter used) are given only in the 2D files.

4. Ghosts

In the course of the ghosts' inspection, we have used both the 2D and extracted images. The 2D images were displayed using very low cuts (from 195 to 250 ADU, note that 191 ADU was the CCD BIAS level) and the inspection was carried out visually. When ghosts were noticed the 1D files were checked.

Hereafter we give some general remarks which came out from the tests. Observers are strongly invited to analyse the spectral region of interest before starting their observations.

4.1 Th-Ar ghosts

These ghosts are easily identified by displaying the 2D frames with very low cuts. In Figure 1 an example is shown: TH6470.2D with cuts between 195 and 250 ADU. In this frame we may distinguish two different effects:

(i) Strong, saturated lines: they produce x-elongated images, and are characterised by a stronger intensity in the slit centre, decreasing towards the edges.

(ii) Thin lines, having uniform intensity and extending over the whole CCD window. These lines are real ghosts. They are probably due to the reflection of strong adjacent Ar lines. No corresponding ghosts are seen in the FF exposures. They are present in the whole RED do-

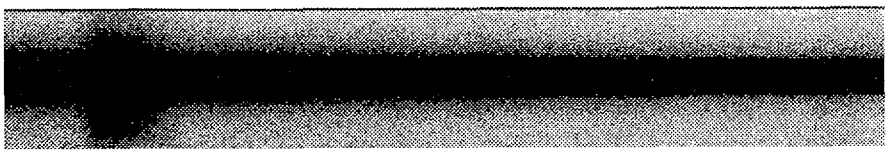

Figure 3: *Two-dimensional image of the FF centred at 5865 Å; note the presence of a FF ghost in the blue part of the spectrum.*

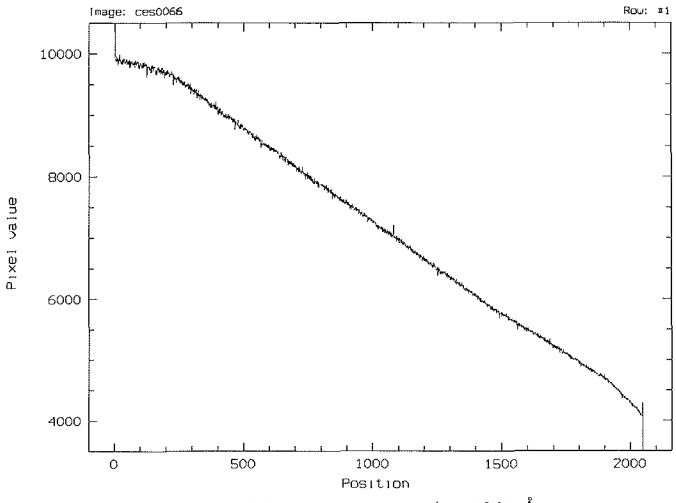

Figure 4a: *Extracted FF spectrum centred at 5865 Å.*

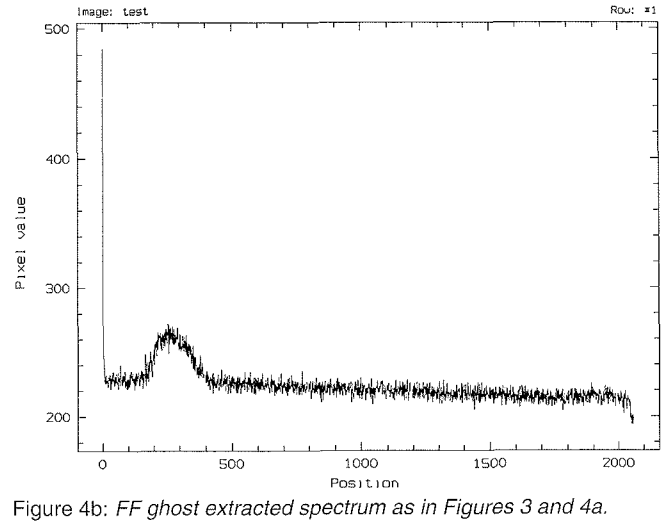

Figure 4b: *FF ghost extracted spectrum as in Figures 3 and 4a.*

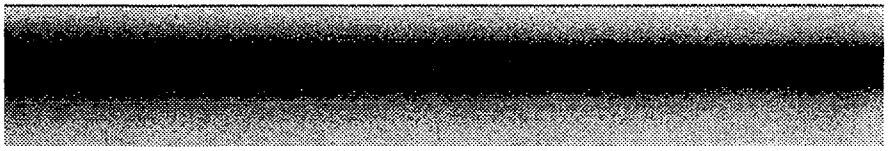

Figure 5: *Two-dimensional FF spectrum centred at 7870 Å.*

main, at virtually all wavelength settings, but their number and intensity increase with the wavelength; none are reported below 5000 Å.

Although Figure 1 could suggest that these ghosts may seriously affect the wavelength calibration, we would like to emphasize that in most cases their presence is negligible. Their intensity is typically much lower than that of true Th-Ar lines. This can be seen directly from Figures 2a and 2b. In Figure 2a the extracted spectrum of Figure 1 is presented (it will be TH6470.1D in the present notation); in Figure 2b the 'ghosts' spectrum for the same region is shown, obtained by extracting the spectrum on the side of the slit and taking away the contribution of the strong, saturated lines.

The presence of these low-intensity ghosts will therefore be most critical in those regions in the RED domain where the paucity of suitable lines makes the wavelength calibration difficult. A careful inspection of the calibration frames is always suggested in the reduction phase.

For several RED settings we have taken multiple exposures slightly shifting the central wavelength (typically by 5 Å). In all the cases the Th-Ar ghosts appear at constant wavelengths.

4.2 Flat Field Ghosts

The presence of ghosts in the Flat Field may be very critical, because their presence may produce uncertain results, changing for instance the shape or the equivalent widths of spectral lines.

FF ghosts were also identified visually using suitable (low) cuts, and it was found that their presence is confined to the spectral range 6170–4560 Å. Most of them fall at the side of the spectrum, thus not influencing the astronomical results for point-like sources.

Unfortunately, some of the FF ghosts do fall over the spectra. In Figure 3 the FF centred around 5865 Å is shown; a ghost is clearly present. In Figures 4a and 4b the extracted FF spectrum and the extracted ghost (the ghost image was extracted on the side of the slit) are shown: the ghost intensity is ~ 0.5 per cent of the FF intensity. Notice that in the extracted FF spectrum no 'bumps' are evident at the pixels corresponding to the ghost.

The presence of FF ghosts is limited to grating angles comprised between 273.5 and 275 degrees, which could suggest that they are due to the grating itself, however, in other grating positions encompassing this range, they were not recorded.

Although their intensity is very low and they are not clearly detectable in the extracted spectra, some care should be taken when the ghost is going to overlap over a spectral line of interest and in very high S/N-ratio observations.

A list of FF ghosts cannot be provided because, unlike Th-Ar ghosts, FF ghosts are *not* at a constant wavelength, but they shift by only a few pixels when changing the λc by several Å. This characteristic is on the other hand quite important, because if the presence of a FF ghost must be avoided at a given wavelength, this can be done by slightly shifting the required λc.

An additional, interesting feature emerges from the comparison of Figures 5 and 6, which show FF exposures taken at 7870 and 4310 Å respectively. The spectra are shown with the same cuts, and they have similar intensity. The level of diffuse light (clearly visible as hazy background out of the slit), is higher in the Blue spectrum. This is a general feature and it is not surprising: in general blue ranges are more sensitive to diffuse light, mostly due to enhanced scattering by dust in the spectrograph optics.

Acknowledgements

This work could not be achieved without the help of the La Silla TRS and Astronomy Support departments. A special thanks goes to the many CAT+CES Visiting Astronomers, who have, with their suggestions, pushed for the construction of the calibration data base.

For further information please contact:
L. Pasquini, ESO-La Silla,
e-mail: lpasquin@eso.org

Figure 6: *Two-dimensional FFspectrum centred at 4310 Å. The cuts are the same as in Figure 5: note the higher level of diffuse light in the 4310 Å frame with respect to the 7870 Å one.*

ERRATUM

Figure 1of the article "New Holographic Grating for the B & C on the ESO 1.52-m Telescope", published in *The Messenger* No. 77 – September 1994, had incorrect labelling of the x-axis. The correct figure is shown here.

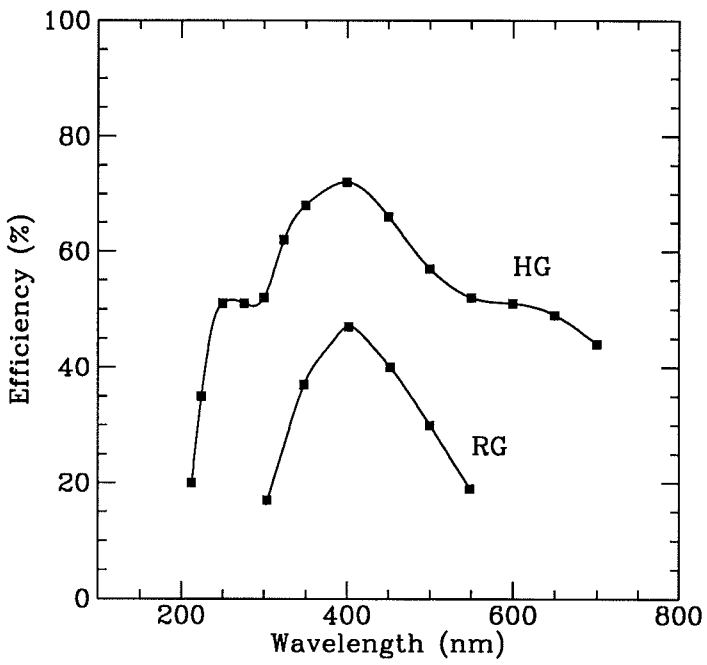

The SL-9 Workshop Round-Table Discussion – A Summary

H. BÖHNHARDT (Universitäts-Sternwarte, München, Germany);
R. SCHULZ (MPI für Aeronomie, Katlenburg-Lindau, Germany)

Introduction
(by R. West, ESO-Garching)

The SL-9 Workshop at ESO-Garching, demonstrated that – since the exciting impact week from July 16 to 22, 1994, over the IAU General Assembly in The Hague in late August 1994 and the DPS Meeting in Washington DC in early November 1994 – significant progress has been achieved in the understanding of the SL-9 phenomena. The fragmentation of the object, the initial impact phenomena, their spectral signatures and long-term effects of the spots in Jupiter's atmosphere can now be analysed on the basis of the available flux- and time-calibrated observations over a wide wavelength range covering X-ray, UV, visual, IR to radio regions. Simultaneously and to a large extent driven by expected and unexpected observational results, the interpretation and theoretical modelling of the SL-9 pre- and post-impact phenomena have brought up new scenarios and already very valuable quantitative descriptions for various phases of the SL-9 event. However, we are still far away from a global scenario and satisfactory understanding of all phenomena related to the SL-9 impacts at Jupiter. This holds equally for observation and theory. Statements of workshop participants like (cited anonymously):

– "Something" exploding in the atmosphere . . .

– We see different effects at different times at different wavelengths!

– I don't see it either, but I did observe it!

– There is perfect agreement, except that in our images the northern hemisphere is bright, in his data it is in the south!

– I think everybody will finish publishing the observations this year (big smiles . . .)!

– I did expect some questions! may reflect the vivid discussions of the still puzzling results obtained so far from a unique and tremendous amount of data gathered all over the world.

This round-table discussion at the end of the workshop aims for conclusions on what is really understood and which steps into which directions are now required to proceed towards a final clarification of the SL-9 impacts at Jupiter.

Fragment Size (by H. Rickman, Astronomical Observatory, Uppsala)

The capture of SL-9 by Jupiter may well remain obscured since the backward orbit integration based upon the available astrometric data can probably not be very significantly improved. However, there are essentially two potential sources from which SL-9 could have come from, i.e. the Trojan zone in the Jupiter sphere of influence and a low velocity accretion zone of cometary objects outside Jupiter's sphere of influence. The mechanical strength of the object was low (probably of the order of 100 Pa). Trojan objects as SL-9 pre-capture candidates are therefore unlikely since they are not believed to be that fragile. Therefore, SL-9 may have resembled more an aggregate of only weakly bound cometary nuclei. The tidal splitting of SL-9 points to a relatively low tensile strength, in that way also imposing a constraint on the radius for the parent body. A fragment size of about 1 km would fit the existing observations.

Discussion

Corrections to the formula for tidal disruption should be made since object rotation and adhesive forces of the body material are not included in the model (Shulman). Gravitational pressure was also neglected so far which would support larger radii for the parent object of the fragmented nuclei. SL-9 may be considered as loose aggregate of planetesimals which split in Jupiter's orbit along weakest adhesive walls (Kelemen). For equal tensile strengths a big comet is easier to break (Sekanina).

Penetration Depths (by B. Mosser, Institut d'Astrophysique, Paris)

The actual penetration depth of the SL-9 fragments into the Jovian atmosphere is still an open question. The proposed scenarios range from "far above the cloud layers", over "right on top or slightly below the upper layer" to penetration "down into atmospheric levels of several bars". The penetration depth should be related to the size of the body entering the atmosphere, i.e., the larger the size of the fragment, the deeper the penetration into the atmosphere of Jupiter. However, a direct relation between these still unknown quantities has not yet been demonstrated. A key role for the description of the entry phenomena is played by the energy deposition in the atmosphere versus altitude, a relation which has so far not been established. Besides the lightcurve features of the impacts and post-impact seismic phenomena on Jupiter, the chemical abundances in the ejecta clouds may also allow to constrain the entry depth of the fragments.

Discussion

Mass ablation plays a dominant role for meteorites entering the atmosphere of Earth (for instance: a 50-ton meteorite was observed to be totally dissipated, already above an altitude of 55 km in the Earth's atmosphere). Such a scenario for the SL-9 entry at Jupiter would imply a much stronger mass loss and kinetic energy dissipation of the fragments above the upper cloud layers with even complete disintegration at pressure levels of some mbar (Sekanina). Whether the existing smart theory for meteorite entries on Earth can be applied to the description of the SL-9 impact at Jupiter, remains an open issue for the future. However, for our ongoing analysis of the SL-9 impacts it seems absolutely necessary to invoke also the knowledge about meteorite phenomena on Earth (Shulman). This may be improved for the entry of larger bodies with a weaker and differentiated internal structure (Mosser). The possibility of constraining the fragments' penetration depth by the non-detection of explosion signals at 5 mm (Käufl) was questioned (Orton, Hammel), since it is not clear that this wavelength range is really sensing the 5 bar level in the Jovian at-

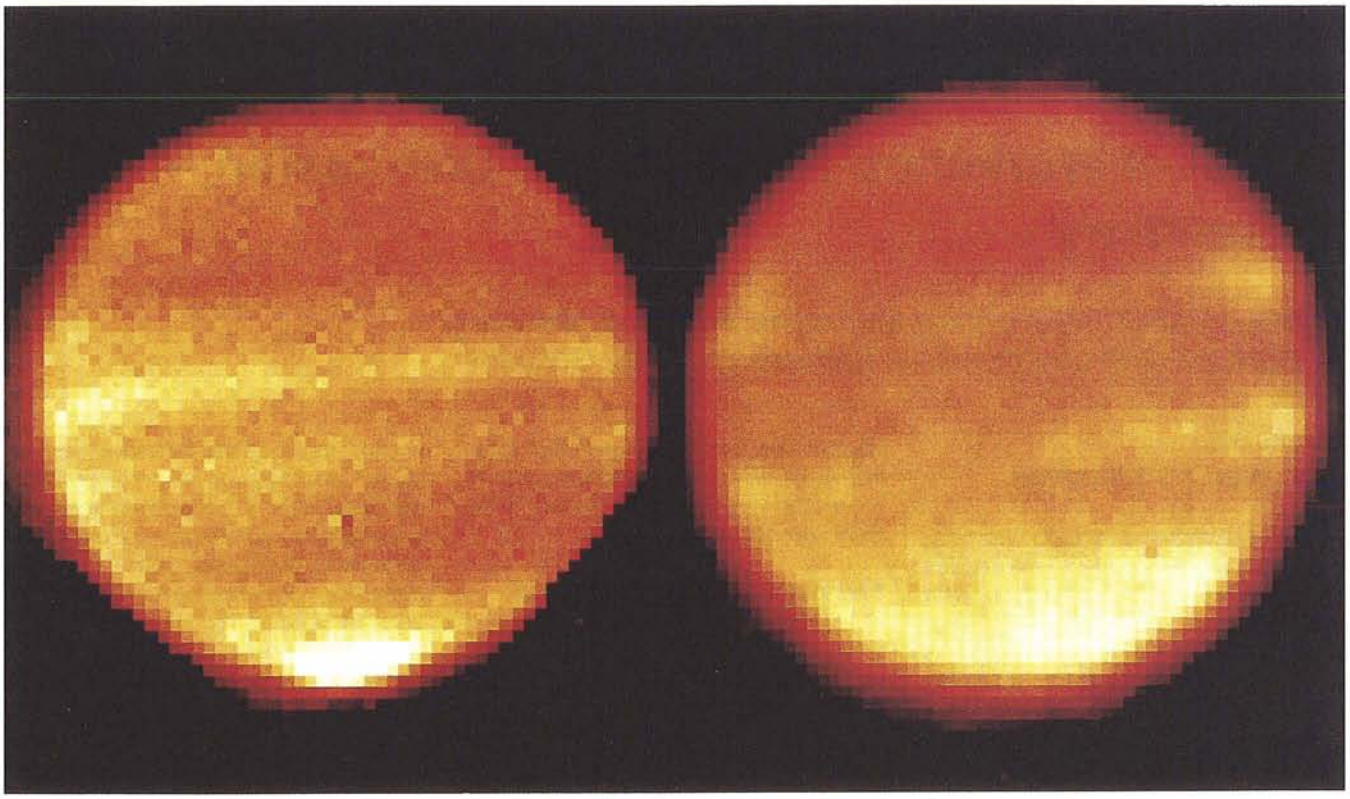

Persistent Effects of SL-9 Impacts On Jupiter

These two images illustrate the persistent effects of the impacts of the fragments of Comet Shoemaker-Levy 9 on Jupiter which took place on July 16– 22, 1994. The first was obtained 5 months before these impacts; the second almost 7 months thereafter. Both were taken with the TIMMI instrument attached to the ESO 3.6-m telescope at La Silla. The first image was taken in the night February 28–March 1, 1994 by ESO observers Ted Kostiuk, Tim Livengood and Hans Ulrich Käufl as part of a parallel observation of Jupiter together with the IUE spacecraft to study auroral phenomena on Jupiter. It shows a bright spot at the south pole. This is the well-known phenomenon of the Southern Aurora which was the main objective of this observation run. While on Earth the Aurora Borealis is a transient effect, it is nearly always present on Jupiter. Due to the inclination of Jupiter's magnetic axis, the appearance of this aurora depends on the rotational state of the planet.

The second image was taken on February 5, 1995, at 14 h 20 UT, i.e. in daytime at La Silla, at a moment when this aurora was located on the rear side of Jupiter and therefore not visible. When compared to the first image, it is obvious that the entire southern hemisphere southwards of –40 degree (which includes the SL-9 impact zones) now appears brighter than one year before. This image therefore indicates that debris (e.g. fine dust) from the impacts is still present in the upper atmosphere. Here it absorbs the sunlight and causes an extra heating effect; we see this in this image as thermal emission from the methane molecules there. Apparently the dust from the individual impact sites has now been mixed rather uniformly throughout the southern polar region.

Technical information: Both images are aligned so that the Jupiter North Pole is up and astronomical east to the left. Both images have been made with 0.45 arcsec/pixel magnification; however, because of the different apparition (the Jupiter–Earth distance in February 1995 is 5.75 AU versus ~ 4.95 in February 1994), this corresponds to 1900 and 1620 km per pixel, respectively. Both images were taken with a filter sensitive to methane (CH_4) in the stratosphere of Jupiter having a wavelength pass band of 7.53–7.87 micron. Thermal emission of CH_4 in this band is known to be a good indicator of temperature in the stratosphere.

mosphere. If the fragments did not penetrate deep into the sulphur clouds of Jupiter, they must have had a size of 4 km to explain the large amount of detected S_2 as being of cometary origin (A'Hearn).

Lightcurves, Timing

(by G. Orton, JPL, Pasadena)

The impact lightcurves of the individual fragments are very similar at same wavelength, but exhibit interesting differences (for instance shoulders in the lightcurve decay phase) in the various wavelength ranges observed. There were signals recorded on the ground for almost all impacts which precede the first Galileo detections. Which phenomena have we seen in these first precursors? Can we develop a "standard impact model" and can this include chemistry?

A central question of the SL-9 phenomena is the calibration of the impact energy and the partitioning of the deposited energy in the various dissipative channels in the atmosphere. Related to this are further similarities like the almost identical plume height and the very similar albedo of the fresh impact particulates. However, the plumes behave different in their morphology, size of the impact region and lifetime of the particulates as well as the temperature variations in the stratosphere and troposphere. The basic question is: what can we use for calibration, or in other words, whas it always the same for different fragments?

Another important point is the partitioning of the energy in the atmosphere and the determination of the temperature variations/gradients between the stratosphere and the troposphere. We have to understand the lightcurves and model them. All of this can only be accomplished by collaborations between the observers of the different phenomena: 1. heating of the channel (IR), 2. bolide, 3. plume.

Discussion

A possible consent of this workshop on what was happening during the impact was formulated by H. Hammel: entry channel heating for the first precursor, a very hot fireball for the second precursor, followed by a rapid sweeping through of

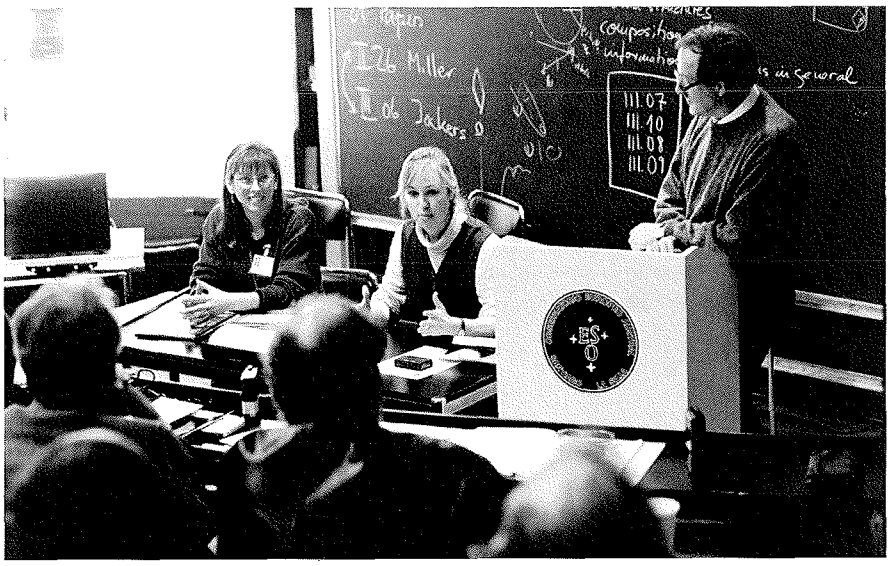

SL-9 Press Conference. From left to right: Heidi B. Hammel, Victoria Meadows, R. West.

maximum light from UV to IR, but still increasing in luminosity. Time scale differences may also depend on the actual depths of the impact explosion (Hamilton).

Shock Chemistry
(by R. West, ESO-Garching)

The chemistry of the impact phenomena is even more complicated than their temporal evolution. Although a whole suite of post-impact ingredients was measured at the impact sites, we are very far from understanding what is ob-served. We do not know the composition and chemistry of the fireballs and plumes, and we have only preliminary ideas about the detailed causes for the very rapid changes that have been spectrally docu-mented. The simple picture of evaporat-ing gas of cometary origin does not easily match the observed phenomena. It is very evident that all of this requires proper theoretical treatment by experts who usually work outside the field of astronomy. Interdisciplinary collaborations are now needed and must be widely encouraged.

Aeronomical Effects
(by W.-H. Ip, MPI for Aeronomy, Katlenburg-Lindau)

The impact explosions caused disturbances in the atmosphere followed by disturbances of the Jovian ionosphere. The latter do couple back to atmospheric layers, in that way closing a loop which may play an important role for the understanding of the post-impact phenomena. There are also severe magnetospheric effects from the impacts which still await explanations: the H_3^+ emission in the impact counterparts at northern latitudes, the brightening and dimming of the northern and southern aurorae and the injection and storage mechanisms for the synchrotron radiation observed. A very puzzling issue are the very selective effects on the inner and outer region of the Jovian magnetosphere whereas at the same time no reaction in the plasma torus of Io could be measured. The aeronomical effects observed call for a 2D theoretical treatment, or even 3D tomographic approach for solution.

Discussion

The phenomenological description of the impact effects to the Jovian magnetosphere is still incomplete since the VLA measurements are not yet available (Dulk). The amount of impact energy coupled into ionospheric and magnetospheric phenomena should comprise – to about 2 orders of magnitude – that of the X-ray and UV energy release by the phenomena (Ip). It is very unclear how the increase of synchrotron radio emission by Jupiter can be explained since it is in total contradiction to what was expected, i.e., a decrease of the radio emission due to electron absorption by the impact dust after migration into the magnetosphere. At the same time decametric observations do not show an increase in radio emission; so far, this has no reasonable physical interpretation (Miller, Dulk).

Collaboration and Coordination
(by T. Encrenaz, Observatoire de Paris-Meudon)

Since calibrated lightcurves and spectra of the impacts are available now from various sites in different wavelength ranges, it is very valuable and absolutely necessary that collaborations between the various groups start immediately. The synergy of multi-wavelength interpretations is now required to further the understanding of the impact phenomena. A very preliminary and still incomplete list of potential collaborations between groups of observers is compiled in Table 1 (sorted by impacts for the lightcurves and by wavelength range for spectral features).

It seems to be very important to compare the similarities and diversities between the detections of the same impacts.

Discussion

A more complete list of groups which have collected observations of the same

SL-9 Round Table. From left to right: B. Mosser, W. H. Ip, H. Rickman, Th. Encrenaz, G. Orton.

TABLE 1. Lightcurves.

Fragment	Visible	Near-IR	Thermal IR
A	HST	Pic-du-Midi Calar Alto UKIRT	ESO La Palma
C		UKIRT AAT Japan IRTF	
D		AAT	
E	HST	Pic-du-Midi Calar Alto	La Palma
G	HST	NIMS IRTF AAT	
H	PPR	Calar Alto Pic-du-Midi ESO	ESO La Palma
K	SSI	AAT Japan	
L	PPR	Pic-du-Midi Calar Alto	La Palma
N	SSI	AAT	
Q		Pic-du-Midi Calar Alto	La Palma
R		Keck Palomar NIMS AAT	IRTF
S		Pic-du-Midi Calar Alto	
W	HST SSI	AAT	

TABLE 2. Spectral identifications

Wavelength	Species	Group	Fragments
UV	S_2, S, SII, Na(*), Mg, CS(*), CS_2, NH (*)	HST IUE	
Visible	Na(*), Ca, Fe, Mg, Mn, Li, K, H, Ha	La Palma Pic-du-Midi	L, Q
2.2–2.4 μm	H_2 CO(*) CH_4(*) NH_3(*) H_2O ? (*)	AAT ESO Calar Alto AAT AAT AAT AAT	C, D A, E H, L C, D, G, K, R C, D, G, K, R C, D, G, K, R C, D, G, K, R
2.7–3.2 μm	O-H, C-H (*)	NIMS	G
3.5 μm	H_3^+ CH_4(*)	ESO UKIRT ESO UKIRT CFHT	1 week after impact H C C, R
4.7 μm	CO(*)	CFHT IRTF	L L
7 μm	H_2O(*)	KAO	
10 μm	NH_3(*) C_2H_4	IRTF IRTF	G G
mm	CO(*) CS(*), OCS HCN	IRAM SEST IRAM JCMT	
cm	H_2O ? (*)	Medicina	E
Multi-wavelength detection of species is indicated by symbol (*)			

These preliminary tables were mainly compiled from the presentations of the workshop; many other data, US in particular, will probably be missing.

event shall be compiled within the next few weeks and will be attached to the proceedings of this workshop. Input for this list should be directed via e-mail, either to R. West (rwest@eso.org) or to M. A'Hearn (ma@astro.umd.edu).

Early speculations of the formation of a new ring around Jupiter due to dust ejected from the impactors during their decent are not very realistic, since most dust of SL-9 (at least down to 100 μm grains) hit Jupiter. Therefore, if something will happen to the ring, it should show only small effects (Hamilton).

It must be assumed that the impactors were totally evaporated during the explosions. New dust was formed in the impact plume within 2 to 3 minutes, but how and why is completely unclear. Whether there is a chemical differentiation in the dust, is also on open issue which can at present not be answered by the modellers (Fitzsimmons).

The most important question of the SL-9 impacts however is: *where did all that energy go?* (A'Hearn). Energy dissipation by shock breaking and ablation of the nuclei during entry into the Jovian atmosphere followed by increased deceleration during descent was so far not taken into account. Differential effects of that kind may have caused substructure in the lightcurves of the fragment impacts (Sekanina).

Closing Remarks
(by R. West, ESO-Garching):

The three days of this workshop convincingly proved that considerable progress has been achieved in the compilation of reliable and quantitative observational facts, as well as in their theoretical understanding. It is nevertheless clear that we must continue the series of SL-9 conferences in order to improve the description of this unique event and before we may finally converge towards a comprehensive model of all related phenomena of the impacts at Jupiter. The next SL-9 conference is scheduled for 9–12 May 1995 in Baltimore. I am sure that later follow-up meetings are also very likely to occur, perhaps already in late 1995, and certainly next year.

For further information please contact:
H. Böhnhardt, Universitätssternwarte, München; e-mail: hermann@vlt.usm.uni-muenchen.de

Diffraction-Limited K-Band Observations of the Star Cluster R136

B. BRANDL, S. DRAPATZ, A. ECKART, R. GENZEL, R. HOFMANN, M. LOEWE, B.J. SAMS,
Max-Planck-Institut für Extraterrestrische Physik, Garching, Germany

Introduction

The 30 Doradus region in the LMC is the largest Giant HII region in the Local Group. Although its diameter is only about 200 pc, it contains a stellar mass of more than $5 \times 10^5 M_\odot$. The bolometric luminosity in its centre is 50 times larger than in the inner 0.2 pc of Orion and its stellar density is a million times larger than in our solar neighbourhood. The ionising radiation is produced by the massive early-type stars of the stellar cluster NGC 2070,

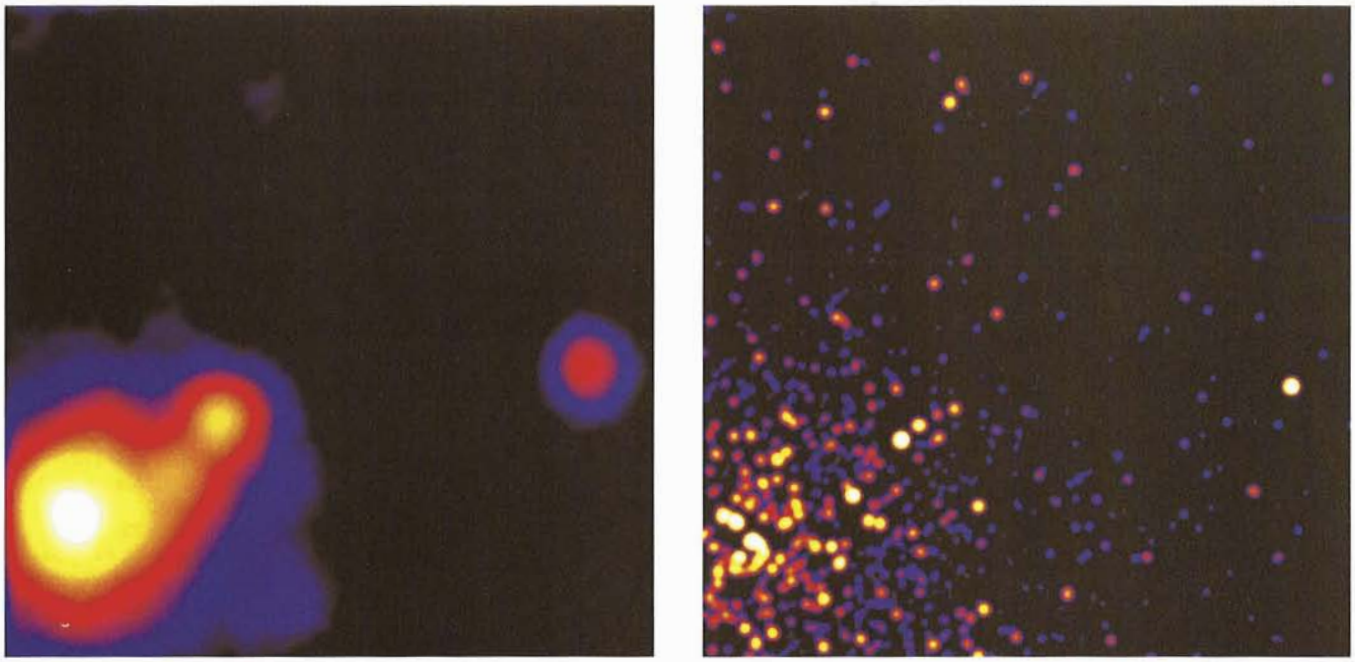

Figure 1: *The-left-hand side shows a short exposure taken in H band with the AO system switched off; the right-hand side shows the same 12."8 × 12."8 (3.2 × 3.2 pc²) field of view in K-band with adaptive optics correction. North is down and east is to the right. Logarithmic scaling has been used.*

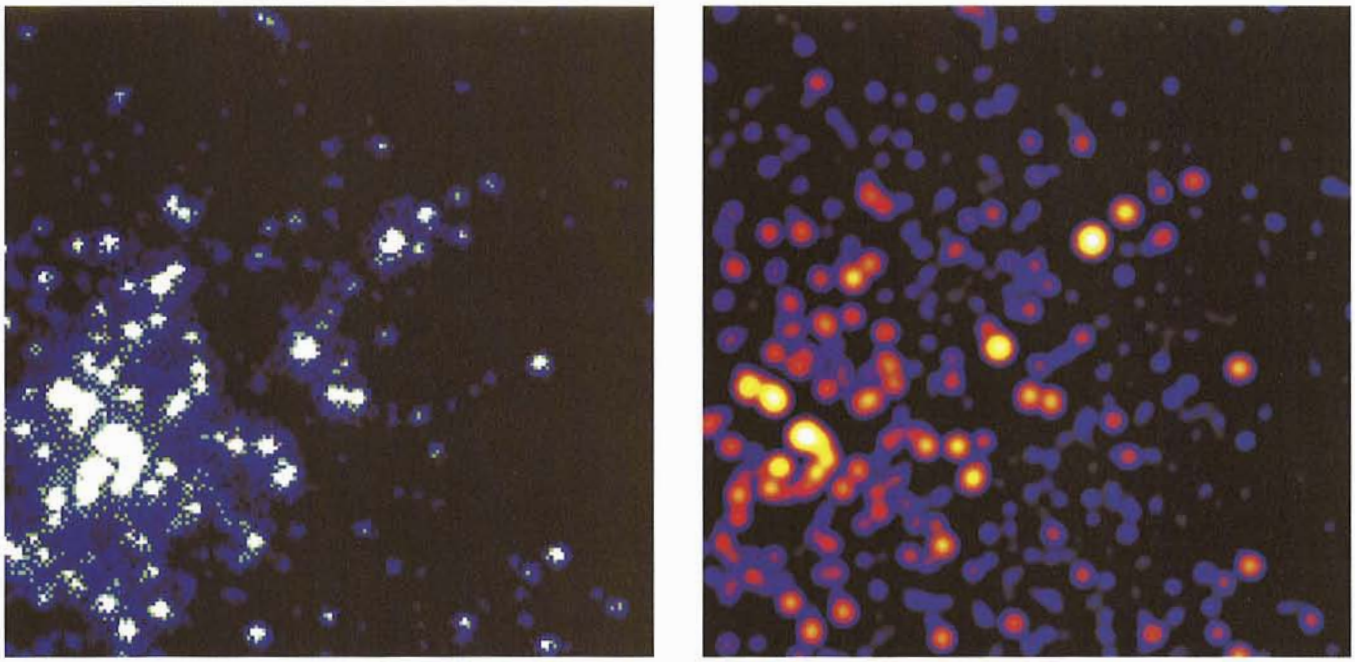

Figure 2: *The central 6."4 × 6."4 around R136 as seen by the HST WF/PC-2 camera (left) and the Come On +/Sharp2 system (right). North is down and east is to the right. The peaks in the HST image are clipped and logarithmic scaling has been used for both images.*

located in the inner 45 pc of this Giant HII region (Campbell et al. 1992). Standard ground-based observations, hindered by atmospheric seeing, showed that the massive core of this stellar cluster (known as R136) consists of three components: R136a, b and c. At one time, R136a was considered to be the most massive star ever known, with about 2000 solar masses (Cassinelli et al. 1981). With ground-based speckle techniques in the visible, Weigelt & Baier (1985) demonstrated that this object consists of at least eight stellar components, thus solving the super-massive star problem. These results have been confirmed by HST observations (Weigelt et al. 1991, Campbell et al. 1992).

The age of the cluster is supposed to lie between 3 and 5 million years, estimated from the presence of massive WN-type Wolf-Rayet stars and the lack of red supergiants. Although none of the stars in R136 is in itself exceptional, the extraordinarily high concentration of O, B and Wolf-Rayet stars represents an ideal, unique starburst laboratory – near enough to be resolved into individual stars and large enough to serve as a typical model of starbursts in distant galaxies.

Observations

The data presented here were taken on December 27, 1994 using the MPE near-infrared camera SHARP2 connected to ESO's adaptive optics system Come On+ on the 3.6-metre telescope on La Silla.

The Sharp2 infrared camera is equipped with a 256 × 256 pixel Rockwell NICMOS3 array detector and is optimised for high-resolution broad-and narrow band imaging in the 1.1–2.5 μm band (Hofmann 1993). The image scale of 0.″05 pixel, results in a total field of view of 12.8 × 12.8 arcseconds and provides Nyquist sampling at wavelengths as short as the J band on the ESO 3.6-m telescope. Wide-band filters provide colour discrimination in J (1.10–1.40 μm), H (1.45–1.85 μm) and K (1.95–2.45 μm) bands. A circular variable filter (CVF) which covers the H and K band with a spectral resolution $\lambda/\Delta\lambda \approx 60$ is also integrated. The total throughput of the optical system, including the quantum efficiency of the detector, is around 50 % in H and K band. The array detector is read out with 4 custom-designed DSP boards permitting integration times from 50 ms up to several minutes per frame.

The Come On+ system (Beuzit et al. 1995) was the first adaptive optics system open to the astronomical community and in its first two years of operation has produced many remarkable results (Léna 1994). A reference source, brighter than approximately 13th magnitude in the V band, is required for wavefront correction. This source must appear unstructured on the wavefront sensor. The central cluster of stars forming R136a itself is sufficiently bright and compact to serve as the wavefront reference in our observations.

We integrated for 190 minutes in the K band under good atmospheric conditions (≈ 1″ seeing). Significant residual triangular coma in the PSF required additional image deconvolution. We used Melnick 34, a bright and isolated star near the edge of our detector, to deconvolve the image. After 5000 iterations of the Lucy-Richardson algorithm (Lucy 1974), the resulting map of delta functions was reconvolved with a Gaussian beam of 0.″12 FWHM, which corresponds to the 3.6-metre telescope's diffraction limit in K.

Results

The left-hand side of Figure 1 shows a short exposure taken in H band with the AO system switched off, while the right-hand side shows our final adaptive optics K-band image. For the first time in this wavelength region, the central stellar minicluster R136a is clearly resolved into several components. The dynamic range between the brightest and the faintest sources is approximately 9 magnitudes. The whole image reveals more than 400 stars above the 3-sigma detection level, the faintest of which are 20th magnitude in K, which corresponds to a lower mass limit of 2–3 $M_\odot$ (Forestini 1993). Assuming a cluster age of 3 million years those stars are still evolving on the pre-main sequence. This detection limit is valid in the outer parts of our field; due to crowding, it is lower in the central region. Transparencies showing the comparison between these images can be obtained from the authors.

Figure 2 displays the central region as previously observed by the refurbished HST (Hunter et al. 1995). Despite the fact that HST's spatial resolution is about twice ours, we see essentially the same sources as observed by Malumuth et al. (1994) plus some additional red objects. Our observations, which also include H- and J-band images, can be combined with HST stellar observations in U, B and V bands in order to minimise photometric errors and estimate the small-scale variations of dust extinction in the dense core of this stellar cluster. A combination of HST and adaptive optics data covers a wide spectral range and enables us to investigate individual stellar types, varying IMF slopes, and the duration of the starburst. The results of this analysis will be presented in a forthcoming issue of *The Messenger*.

References

Beuzit, J.L. et al. 1995, to appear in *A&A.*.

Campbell, B. et al. 1992, *A.J.* **104**, 1721.

Cassinelli, J.P., Mathis, J.C., Savage, B.D. 1981, *Science* **212**, 1497.

Forestini, M. 1994, *A&A* **285**, 473.

Hofmann, R. et al. 1993, ESO 42, *Progress in Telescope and Instrumentation Technologies*, ed. M.H. Ulrich (Garching, Germany), 617.

Hunter, D.A. et al. 1995, to appear in *Ap.J.* July 20.

Léna, P.J. 1994, *SPIE* Vol. 2201, *Adaptive Optics in Astronomy*, eds. M.A.Ealey & F. Merkle (Kona, Hawaii), 1099.

Lucy, L.B. 1974, *A.J.* **79**, 745.

Malumuth, E.M. & Heap, S.R. 1994, *A.J.* **107**, 1054.

Weigelt, G. & Baier, G. 1985, *A&A* **150**, L18.

Weigelt, G. et al 1991, *Ap.J.* **378**, L21.

For further information please contact:
B. Brandl, MPA-Garching;
e-mail: brandl@MPA-Garching.MPG-.DE

The H_2 Structure of OMC-1: Disruption of a Molecular Cloud

H. SCHILD, Institut für Astronomie, ETH-Zentrum, Zürich, Switzerland
S. MILLER and J. TENNYSON, Dept. Physics and Astronomy, University College London, U.K.

Introduction

The first detection of infrared quadrupole emission of H_2 in any astronomical object was almost twenty years ago in what is now known as OMC-1 (Gautier et al. 1976). OMC-1 covers an area of approximately 1.5 arcminutes square, located in the giant Orion Molecular Cloud, at a distance of about 450 pc. It contains the much studied Becklin-Neugebauer object and Kleinmann-Low nebula as well as a number of compact

infrared emission sources. According to Genzel and Stutzki (1989), BN-KL is a very dense, clumpy molecular core in which most of the radiation emanates from only a few major luminosity sources, of which IRc2 and BN are the most important. BN itself is considered to be a young star of mass 15 $M_\odot$; IRc2 is a similar object, somewhat more massive than BN at 25 $M_\odot$.

Maps of OMC-1 in the light of the H_2 1–0 S(1) transition at 2.121 μm were first obtained by Beckwith et al. (1978). The maps had an angular resolution of 13.5″ and 5″ and showed two extended lobes and several emission peaks. At this resolution the spatial intensity distribution was rather smooth. For many years these observations remained the standard for OMC-1. They were often used to compare the H_2 emission with detections of other molecular species. More recent H_2 images of the northwest tip of OMC-1 show a general patchy and filamentary or jet-like structure (Burton et al. 1991, Allen & Burton 1993).

Fabry-Perot Observations

A series of images of OMC-1 was obtained during the nights of December 29 to 31, 1993 with the 2.2-m telescope and IRAC2. The Fabry-Perot filter was centred at 2.121 μm. It had a bandwidth of 1.5 nm corresponding to a velocity spread of about 200 km/sec. The accuracy of the wavelength setting was 0.5 nm. The detector was a 256 × 256 NICMOS array. IRAC2 can be used with various objectives providing different image scales. We chose lens LC which provides a field of view of about 2′ and a projected pixel size of 0.5″. Integration times were 5 minutes on source and 5 minutes on two background positions. Subtraction of the background images also removed the rings of thermal emission from the warm FP rather well. The seeing conditions were excellent and the measured FWHM of the stellar images was 0.7″.

The H_2 Structure of OMC-1

In Figure 1 the resulting H_2 image of the OMC-1 is shown. It covers all of the area originally mapped by Beckwith et al. (1978). In the north (top) are Beckwith's Peaks 5 (which nearly coincides with IRc9) and Peak 1. Near the centre of our image, south and slightly east (left) of the line of Peaks 5 and 1, BN shows up brightly. Peak 3 is resolved into two bright sources, south-east of BN. IRc2 coincides with a hollow structure in the H_2 emission map. East-south-east of Peak 3, Peak 2 is a bright, highly structured region.

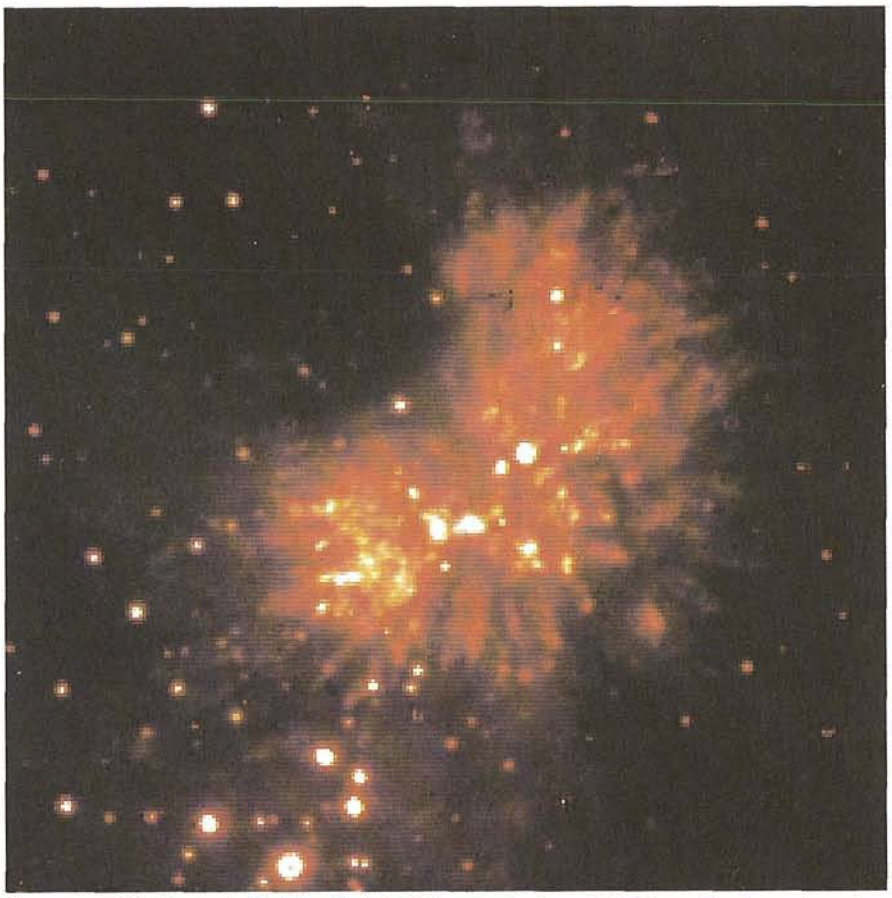

Figure 1. *OMC-1 in the light of the H_2 1–0 S(1) emission line at 2.121 μm. The trapezium stars are visible at the bottom. North is at the top, east to the left.*

With the exception of these sources, our image shows that most if not all of the H_2 emission in OMC-1 is due to near-linear jet-like features, which expand in all directions except the north-eastern quadrant. The H_2 structure of OMC-1 in Figure 1 looks as if it were produced by a highly dynamic or even explosive event. There are several short but well recognisable jets in the south and west. There is also a long, strong jet going almost due north. Tracing these jets back towards the centre, they appear to come from the region around IRc2. In the north-western quadrant and north of east-south-east it is more difficult to trace individual jets through the cloud.

The jets have the appearance of wakes such as might be produced by the bow shocks of "bullets" of dense material fired through the molecular gas. Along the path of the jets there are also knots of brighter emission, probably indicating that the emitting gas in these regions is above average density. In the southwest quadrant in particular, a number of the jets appear to terminate in these brighter knots. The northern jet passes through a bright ring of emission and emerges much weaker in intensity. If the two emission structures are indeed connected, it would appear as if the "bullet" hit a clump of denser material, causing a radially expanding density wave, before passing through.

The jets we measure typically have a projected length of 1.6×10^{12} km. Assuming that the measured H_2 linewidth (Nadeau & Geballe 1979) of 40–100 km/s gives a lower limit for the velocity of the "bullets", such a track could be produced in ~ 500 years. This compares with the estimate of 1000 years by Allen & Burton (1993) for the age of their jets, which are located further away from IRc2 than those presented here. At this expansion velocity, the jetheads will have moved an observable 1″ in 20 years from now. The phenomenon of the molecular cloud disruption is thus extremely short-lived and OMC-1 provides a unique opportunity to observe it.

Conclusions and Outlook

The new Fabry-Perot images of the Orion Molecular Cloud OMC-1 confirm it to be an object generated by a highly dynamic – even explosive – event, and unlike any other astronomical object known. We seem to witness the dynamic processes by which newly-formed massive stars disrupt their parent molecular cloud. OMC-1 appears to be made of numerous linear, jet-like structures, which

are responsible for producing nearly all the nebular emission. The dynamic structure is best described by the wakes of dense "bullets" ploughing through the surrounding molecular gas. The jets appear to diverge from the region around IRc2 in all directions apart from the north-east quadrant. More information on the region – including temperature profiles for the most interesting features — should be obtained by observations in other H_2-sensitive wavelengths and by carefully directed high resolution spectroscopy.

References

Allen D.A., Burton, M.G., 1993, *Nature* **363**, 54.

Beckwith S., Persson S.E., Neugebauer G., Becklin E.E., 1978 *Astrophys.J.* **223**, 464.

Burton M.G., Minchin N.R., Hough J.H., Aspin C., Axon D.J. Bailey J.A., 1991, *Astrophys. J.* **375**, 611.

Gautier T.N., Fink U., Treffers R.R., Larson, H.P., 1976, *Ap. J. Letts* **207**, L129.

Genzel R., Stutzki J., 1989, *Ann. Rev. Astron. Astrophys.* **27**, 41.

Nadeau D., Geballe T.R., 1979, *Astrophys. J.* **230**, L169.

For further information please contact:
H. Schild; e-mail: hschild@bernina.ethz.ch

Combined Optical and Near-IR IRAC2 Photometry of the Bulge Globular Cluster NGC 6553

M.D. GUARNIERI[1, 2], P. MONTEGRIFFO[3], S. ORTOLANI[4], A. MONETI[5], B. BARBUY[6], E. BICA[7]

[1]Istituto di Fisica Matematica, Università di Torino, Italy; [2]Osservatorio Astronomico, Torino, Italy;
[3]Dipartimento di Astronomia di Bologna, Bologna, Italy; [4]Osservatorio Astrofisico di Padova, Padova, Italy;
[5]SERCO/ESA-Astrophysics Division, Noordwijk, The Netherlands;
[6]Universidade de Sao Paulo, Brazil; [7]Universidade Federal do Rio Grande do Sul, Brazil

The bulge region of our Galaxy contains a number of globular clusters whose study can provide important information about the history of the Galaxy formation conditions after the initial collapse of the spheroid. The age, dynamical and chemical conditions of the bulge are the crucial parameters to be investigated. Unfortunately, they are hardly observable in the optical wavelength due to the heavy extinction in the direction of the Galactic plane.

For these reasons we have started a systematic study of a sample of metal-rich clusters in the infrared using IRAC2 withe the new NICMOS3 detector 256 × 256 pixels, mounted at the MPI/ESO 2.2-m telescope at La Silla (Chile).

Here, we present the results of combined visual and near-infrared photometry in one of the most metal-rich globular cluster NGC 6553 ([Fe/H] ~ –0.2). The optical counterparts come from Ortolani, Barbuy and Bica (1990).

1. Introduction

NGC 6553 (α = 18^h 05^m 11^s; δ = –25° 55' 06" (1950.0); [Fe/H] = $^{+0.2}_{-0.4}$ (Ortolani et al., 1990) is a low-latitude galactic globular cluster belonging to the metal-rich cluster family. These objects are projected in the direction of the galactic bulge and form a unique homogeneous sample of bulge population, so the correct determination of their age is crucial for the determination of formation epoch of the inner bulge. Their peculiar c-m diagrams are dominated by blanketing effects giving anomalous tilted HBs and a turnover on the giant branches (Ortolani et al., 1990, 1991, 1992, 1993a, 1993b, Bica et al., 1991). Recently (Bertelli et al., 1994), derived a whole set of solar and super-solar metallicity models which reproduce these characteristics, a major step towards modelling metal-rich pop-

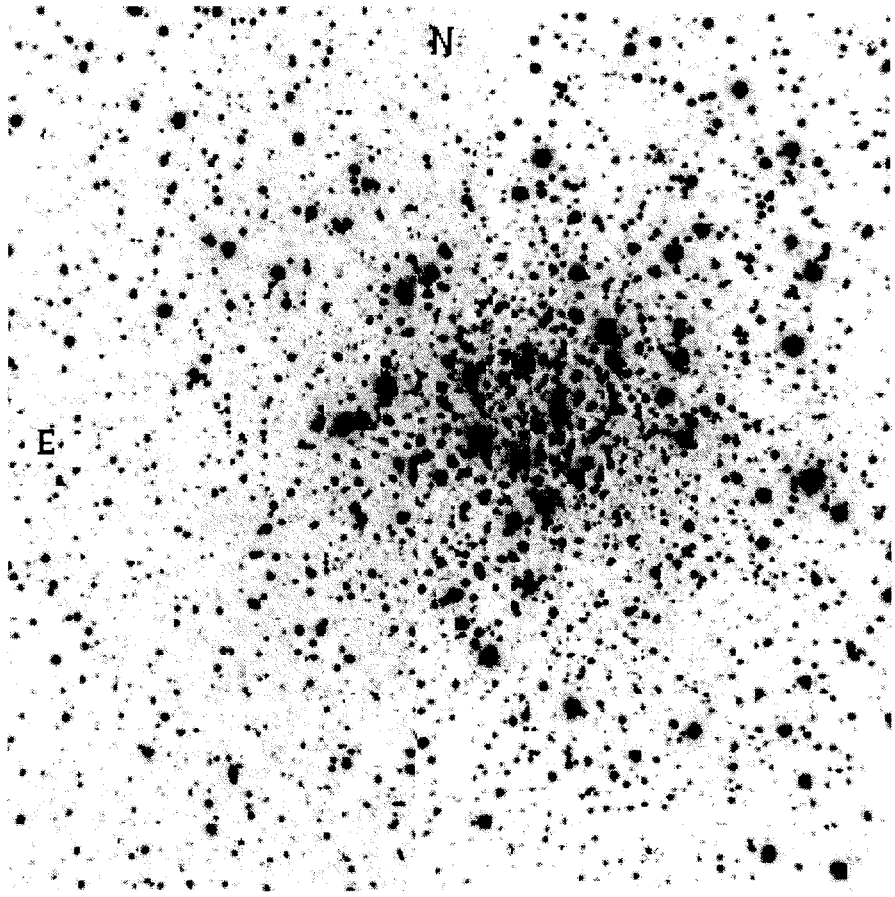

Figure 1: *NGC 6553 composite field as observed with IRAC2 0.5 arcsec/pixel mode, field size ~ 4 arcmin².*

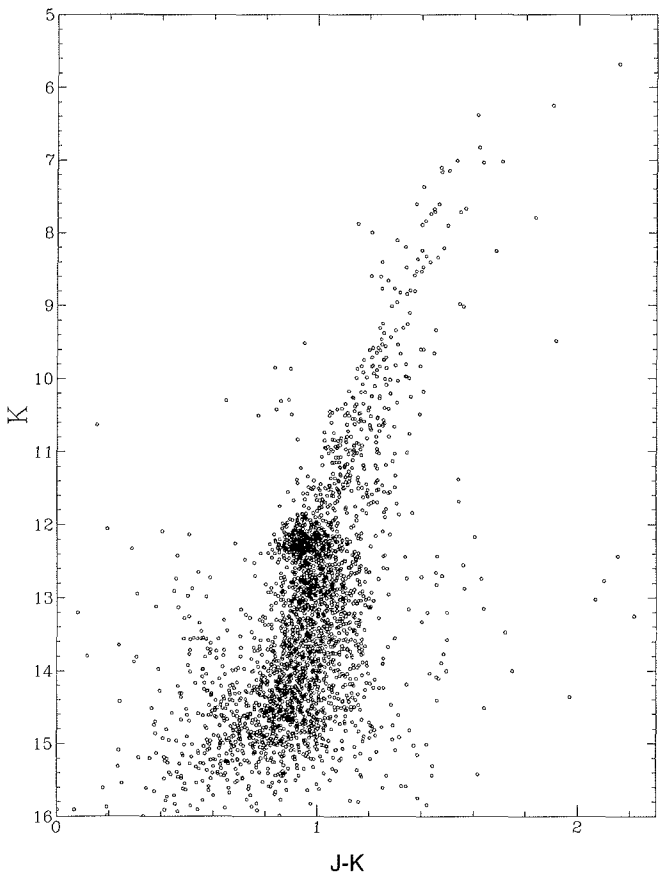

Figure 2: *(K, J–K) CMD of NGC 6553.*

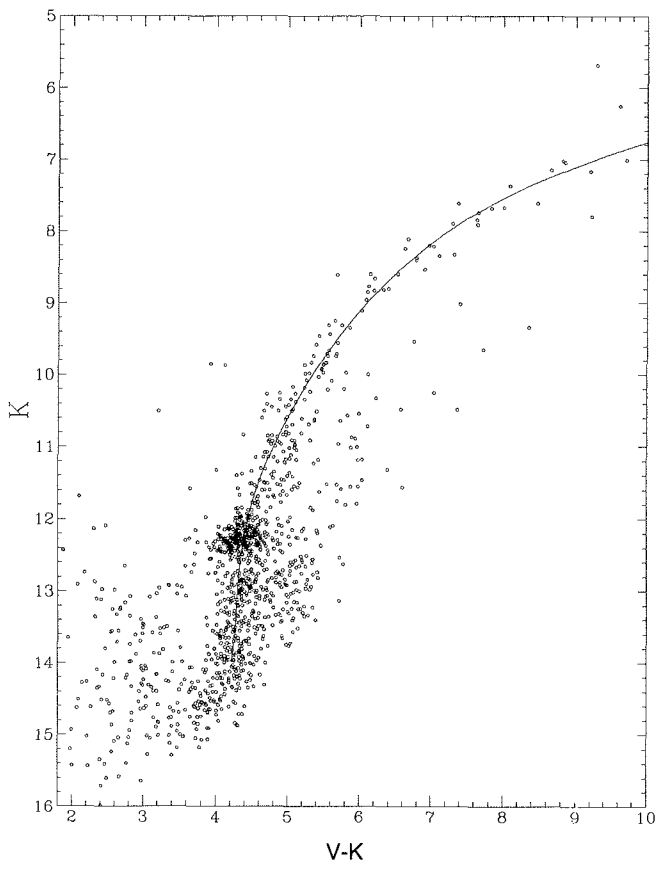

Figure 3: *(K, V–K) CMD of NGC 6553.*

ulations. One of the major problems seems to be the transformation from the theo-retical to the observational plane due to the heavy blanketing effect in the BVRI photometric data.

So, it is clear that IR photometry, much less affected by line and molecular band absorptions, can improve the current theoretical research in this field. For bulge stars, the infrared colours JHK are the best suited also because the extinction is much lower in the IR than in the optical bands, so that all uncertainties connected to the reddening plus blanketing effects determination are less important.

Moreover, combining optical and IR data, it is possible to obtain very useful colour indices, like the V-K which is an excellent indicator of effective temperature (T_e), being relatively insensitive to metallicity and having a long wavelength baseline and line-free continuum fluxes (Guarnieri et al., 1991; Ferraro et al., 1993).

The importance of this study is thus manifold: besides the information on temperatures for stars observable in high (or medium-low) resolution spectroscopy, or determined via the so-called "Infrared Flux Method" (Blackwell and Shallis (1977), Blackwell et al. (1980), Arribas and Martinez Roger (1987)), dating reddened clusters, estimating their red-dening and distance (consequently the globular system structure will be better known), check CMDs of some extremely reddened clusters and derive their properties are crucial points in determining the proto-Galaxy conditions after the initial collapse of the spheroid.

2. Observations and Data Reductions

Infrared observations have been carried out the night of June 11, 1992 using the ESO Rockwell NICMOS3 (HgCdTe, 256 × 256 pixels) infrared camera IRAC2 (cut-off wavelength at 2.5 μm, Moorwood et al., 1992) mounted on the MPI/ESO 2.2-m telescope at La Silla (Chile), at image scales of 0″.27 and 0″.49 for both standard J (1.25 μm) and K (2.19 μm) filters. Through each filter, we obtained a high-resolution image (first magnification value) of the cluster centre, and four partially overlapping images covering a ~ 2′× 2′ square region centred on the cluster core (second magnification). The total field covered is ~ 4 × 4 arcmin² (see Figure 1).

Separate sky frames located at ~ 10′ from the cluster centre were also observed, in each filter and magnification, for sky subtraction purpose. All images are the average of 60 frames of 1 second integration time. The observations were carried out with seeing < 1.4″.

The whole set of data has been analysed using the package for crowded fields photometry ROMAFOT (Buonanno et al. 1979, 1983).

Eight SAAO standards (kindly provided by Dr. Ian Glass) were observed during the run and most of them on at least two positions of the array. The calibration curve and all the details regarding the standard stars have already been published in Ferraro et al., 1993.

The optical BVRI sample, coming from Ortolani, Barbuy and Bica (1990), has been tied to the IR coordinate system using a linear interpolation and a comprehensive catalogue of 1196 BVRIJK stars has been created.

3. The Colour-Magnitude Diagrams

Figures 2 and 3 present the CMDs (K, J–K), and (K, V–K) for all the stars of the sample with the mean ridge lines superimposed. The (V, V–K) is shown in Figure 4 while Figure 5 shows the (V, V–I) diagram from Ortolani et al., 1990 containing only the stars in common with the infrared photometry.

These diagrams confirm the peculiar nature of NGC 6553 with a very red, compact horizontal branch also in the IR diagrams. The giant branch is well defined in the whole extension up to K ~ 6; a parallel redder and lower sequence is also visible in all the diagrams. Further investigations will confirm if this feature is due to a differential reddening or to the background field. The steep giant branch

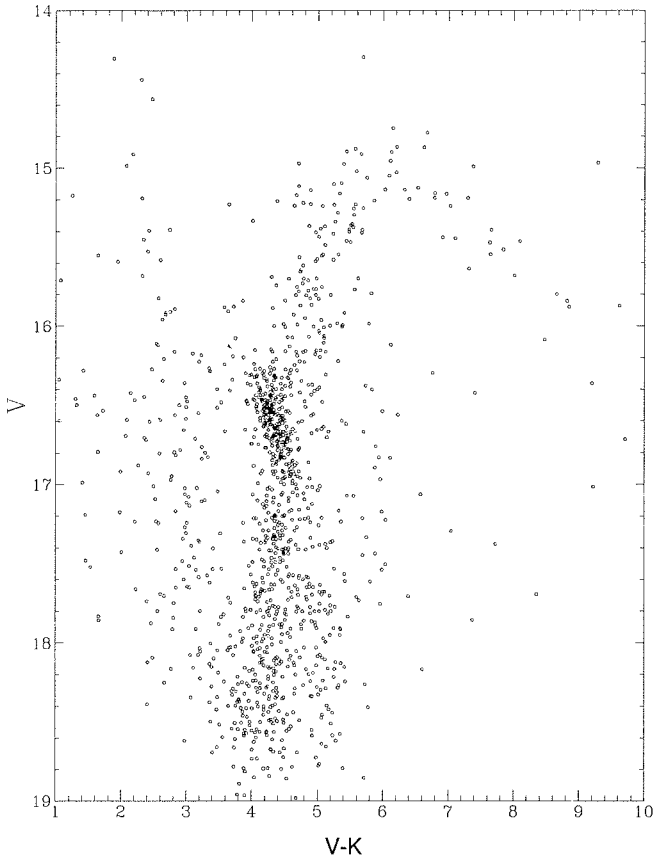

Figure 4: *(V, V–K) CMD of NGC 6553.*

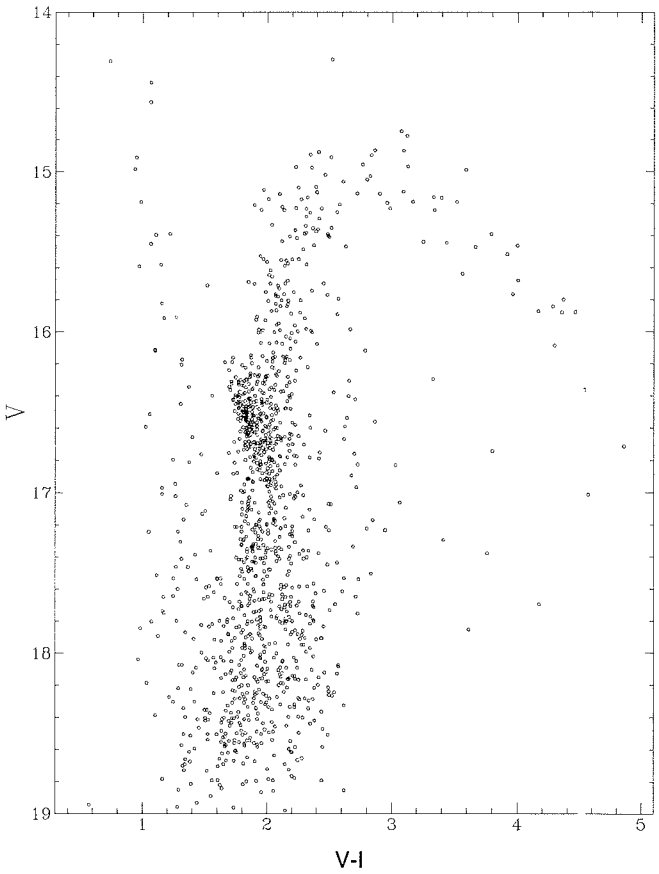

Figure 5: *(V, V–I) CMD of NGC 6553.*

in the IR diagrams shows that the use of IR colours greatly reduces the blanketing effects of the cool stars in metal rich clusters. The horizontal branch in Figure 2 can be localised at about K = 12.25 mag and V–K = 4.35. This measure is much more accurate than the luminosity level obtained using optical CMDs where it appears strongly tilted. From these values V_{HB} = 16.60 is deduced in a good agreement with Ortolani et al., 1990. Assuming M_V^{HB} = 0.8 for [Fe/H] = –0.2 (Fusi Pecci, F., private communication) we get a distance modulus of 13.35 corresponding to d = 4.8 Kpc from the Sun.

Another approach, not dependent on the data, makes use of the new Padua isochrones (Bertelli et al., 1994). For an age of ~ 14 Gyr, the mean level of the horizontal branch is at M_K = –1.45, that is a dereddened distance modulus of 13.4 or about 4.8 Kpc, in excellent agreement with the above determination.

Figure 6 relates the dereddened colour$(J-K)_0$ to the $(V-K)_0$, superimposed are the giant stars in 47 Tuc observed by Frogel et al., 1981 (filled circles). The sequence for the field giants (solid line) is from Frogel et al., 1978. There is a clear shift to a higher $(V-K)_0$ values of the NGC 6553 points compared with 47 Tuc, while the locus of the field stars fits very well. If the shift is only an effect of metallicity (Ferraro et al., 1994, Bertelli et al., 1994) this indicates a nearly solar abundance for NGC 6553.

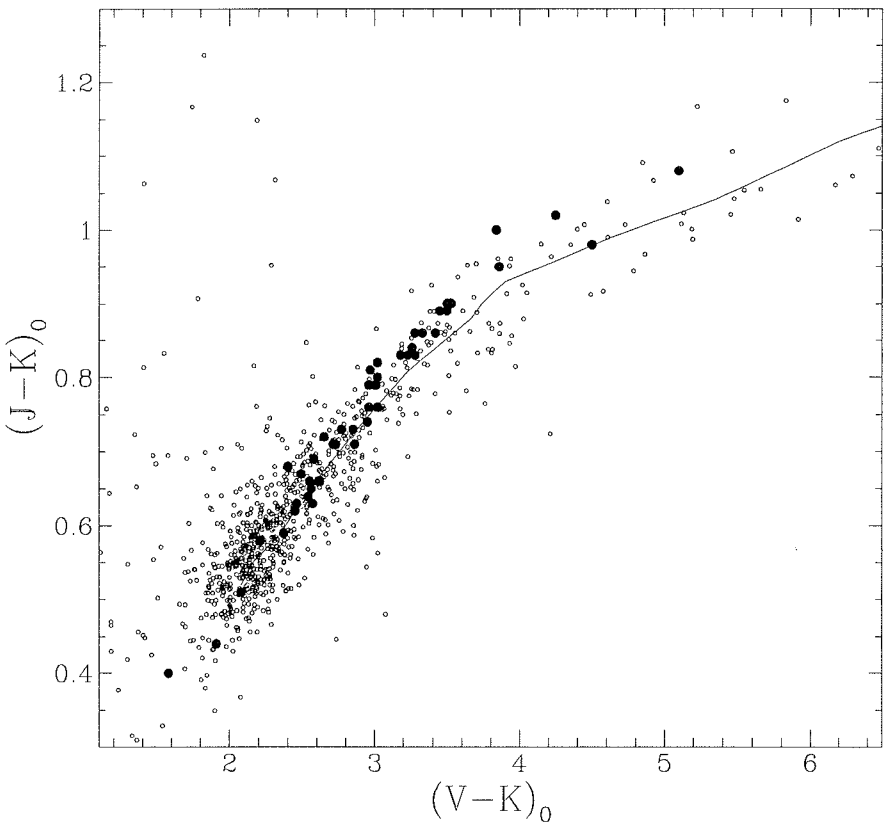

Figure 6: $(J-K)_0$ vs. $(V-K)_0$ CMD of NGC 6553. Superimposed are the giant stars in 47 Tuc observed by Frogel et al., 1981 (filled circles). The sequence for the field giants (solid line) is by Frogel et al., 1978.

The details concerning data acquisition and reduction, and the full astro-

physical discussion will be published in a separate paper (Guarnieri et al., 1994).

Acknowledgements

We would like to thank the ESO organization for the allocation of observing time and for giving us the chance to be the first IRAC2 users. We also thank Hans Gemperlein for the help during the observing run. MDG acknowledges the Università and Osservatorio Astronomico of Torino for their support.

References

Arribas, S., Martinez Roger, C., 1987, *AA* **178**,106.
Bertelli, G., Bressan, A., Chiosi, C., Fagotto, F., Nasi, E., 1994, *AAS* **106**, 275.
Bica, E., Barbuy, B., Ortolani, S. 1991, *ApJ* **382**, L15.
Blackwell, D.E., Shallis, M.J., 1977, *MNRAS* **180**, 177.
Blackwell, D.E., Pedford, A.D., Shallis, M.J., 1980, *AA* **82**, 249.
Buonanno, R., Corsi, C.E., De Biase, G.A., Ferraro, I., 1979, in *Image processing in Astronomy*, eds. G. Sedmak, M. Capaccioli and R.J. Allen, Trieste Obs., p.354.
Buonanno, R., Buscema, G., Corsi, C.E., Ferraro, I., Iannicola, G., 1983, *AA* **126**, 278.
Ferraro, F.R., Fusi Pecci, F., Guarnieri, M.D., Moneti, A., Origlia, L., Testa, V., 1994, *MNRAS* **266**, 829.
Frogel, J.A., Persson, S.E., Aaronson, M., Matthews, K., 1978, *ApJ* **220**,75.
Frogel, J.A., Persson, S.E., Cohen, J.G., 1981, *ApJ* , **842**.
Guarnieri, M.D., Fusi Pecci, F., Ferraro, F.R., 1992., Workshop on Star Clusters and Stellar Evolution, Teramo 18–20 September 1991, *Mem.S.A.It.* **63**,117.
Guarnieri, M.D., Montegriffo, P., Ortolani, S., Moneti, A., Barbuy, A., Bica, E., 1994, in preparation.
Moorwood A., Finger G., Biereichel P., Delabre B., Van Dijsseldonk A., Huster G., Lizon J.-L., Meyer M., Gemperlein H., Moneti A., 1992, *The Messenger*, **69**, 61.
Ortolani, S., Barbuy, B., Bica, E. 1990, *AA* **236**, 362.
Ortolani, S., Bica, E., Barbuy, B. 1991, *AA* **249**, L31.
Ortolani, S., Barbuy, B., Bica, E. 1992, *AAS* **92**, 441.
Ortolani, S., Barbuy, B., Bica, E. 1993a, *AA* **273**, 415.
Ortolani, S., Barbuy, B., Bica, E. 1993b, *AA* **267**, 66.

For further information please contact:
M.D. Guarnieri;
e-mail: MDGUARNIERI@astbo3.bo.astro.it

Observations of the Shoemaker-Levy 9 Impacts on Jupiter at the Swedish-ESO Submillimetre Telescope

D. BOCKELEE-MORVAN[1], P. COLOM[1], D. DESPOIS[2], E. LELLOUCH[1], D. GAUTIER[1], A. MARTEN[1], J. CROVISIER[1], T. ENCRENAZ[1], T. OWEN[3]

[1]Observatoire de Paris-Meudon, France; [2]Observatoire de Bordeaux, France; [3]University of Hawaii, USA

1. Introduction

The SEST was one of the ten telescopes which were used at ESO for the observation of the encounter of comet Shoemaker-Levy 9 with Jupiter (West, 1994). The purpose of these millimetre observations was to search for molecular species which could have been injected or generated by the impacts. Carbon monoxyde was detected on July 23 on impact site G+Q+R+S through its J(2–1) line at 230 GHz. CO, which is normally present with a very low abundance in Jupiter's atmosphere, was likely formed by shock chemistry following the impacts. Difficulties in the reduction of the data prevented us from reporting these results with the other ESO preliminary results of this event in the September 1994 issue of *The Messenger*.

2. Observations

The observations at SEST were conducted from July 18 to 23, 1994. They were a part of a global strategy undertaken by a consortium of European, Canadian and US scientists in order to search for molecular species using millimetre heterodyne techniques. As a result of this strategy, observations of various molecules were made at the IRAM 30-m radio telescope in Spain (Lellouch et al.,1995), at the IRAM millimetre interferometer in France (Wink et al., 1994),with the James Clerk Maxwell Telescope in Hawaii (Marten et al., 1995), and at the SEST. The interest of millimetre heterodyne techniques for planetary observations is the high spectral resolution which allows the detection of narrow molecular lines formed in the stratosphere.

The SEST 15-m antenna is equipped with three heterodyne receivers working in the 80–116 GHz (3-mm receiver), 215–270 GHz (1.3 mm) and 320–360 GHz (0.8 mm) ranges. These receivers were used alternately, depending on weather conditions. We used as backends two spectrometers simultaneously with an 80-kHz resolution (0.1 km/s at 230 GHz) and a 1.4-MHz resolution. In order to reduce the effects of sky and receiver noise fluctuations, the observations were carried out using the "beam switching" method, in which the receiver alternately viewed the impact site and a reference beam position at 2' in azimuth. Because of the relatively large beam width of the telescope (half-power beam width of 15", 23" and 57" at respectively 346, 230 and 86 GHz) with respect to Jupiter's diameter (38" in July), we found it was not worth tracking exactly in position the impact sites. For the observations performed with the 3-mm receiver, the centre of the planet was pointed. For those at 1.3 and 0.8 mm, five beam positions regularly spaced on the Jupiter disk at the latitude of the impact sites (44° South) were defined for the observations. After the first observing days, each position generally encompassed several impact sites. Particular attention was given to the observation of the large impacts G, H, K, L, Q and R. 2-min scans were recorded.

The observations suffered from poor atmospheric conditions, with an opacity exceeding 0.5 at 230 GHz during the first 4 days. The weather was more cooperative on July 22 and 23, with opacities on the order of 0.35 and 0.25. On July 18, the J(3–2) and J(2–1) rotational lines of CO at respectively 345 and 230 GHz were searched for. Although the detection of millimetre lines of CO and HCN was announced at the IRAM 30-m and JCMT, the weather appeared too bad at ESO to allow detection of these species at SEST, and the three following days were mostly dedicated to an exploratory search of other species, namely ArH^+, ArH_3^+, SO_2, HC_3N near 245 GHz, and SiO (86 GHz) and HCO^+ (89 GHz). On July

22, we searched for the HCN J(3–2) line at 266 GHz and the CO J(2–1) line at 230 GHz. On July 23, the CO J(2–1) line was observed on several impact sites.

The reduction of the data was hampered by baseline ripples caused by standing waves between the primary and secondary reflectors due to the high continuum flux of Jupiter (80 K in antenna temperature in the main beam at 230 GHz). This resulted in strong irregular oscillations in the spectra, and sometimes in spurious features of linewidth comparable to the searched lines. The real time data processing was not facilitated by the rapid and non-linear velocity displacement of the impact sites as Jupiter rotates (17 km/s in 4.5 hours to be compared to linewidths of a few km/s). This effect could only be taken into account afterwards, by making the appropriate velocity corrections before co-adding the individual scans.

3. Results

The reduction lead to the detection of the J(2–1) of CO from the spectra observed on July 23 in the D+G+Q_1 +Q_2+R+S complex (Fig. 1). This line was also detected at IRAM 30-m in impact site G on July 18, ten hours after the fall of the responsible cometary fragment. On July 20.82, 20.84, 21.33 and 21.64, fragments Q_2, Q_1, R and S collided with the planet within 7" of impact site G. As a result, the CO observations made at IRAM and SEST the following days on this site encompassed in fact several sites. The observations performed at SEST on July 22 and 23 complement the monitoring performed at IRAM, for which these dates are lacking. In addition, the line detected at SEST shows distinctly the contribution of at least three sites (G, Q_2 or R, Q_1). This differs from the IRAM observations which, due to a smaller beam width (10.4"), are more sensitive to the tracked impact site.

The formation of millimetre molecular lines in planetary atmospheres has been discussed at length in several papers (e.g. Lellouch et al., 1984; Paubert et al., 1984). Provided the velocity dispersion within the sites is small, the linewidth reflects pressure broadening and provides thus a strong constraint on the level of formation of CO. The width of the line due to impact G (1 km/s) suggests that CO is not present in a detectable amount at altitudes deeper than 0.1 mbar. The contrast of the line is a function of both the temperature structure and the vertical distribution of the abundance of CO. Figure 1 shows the

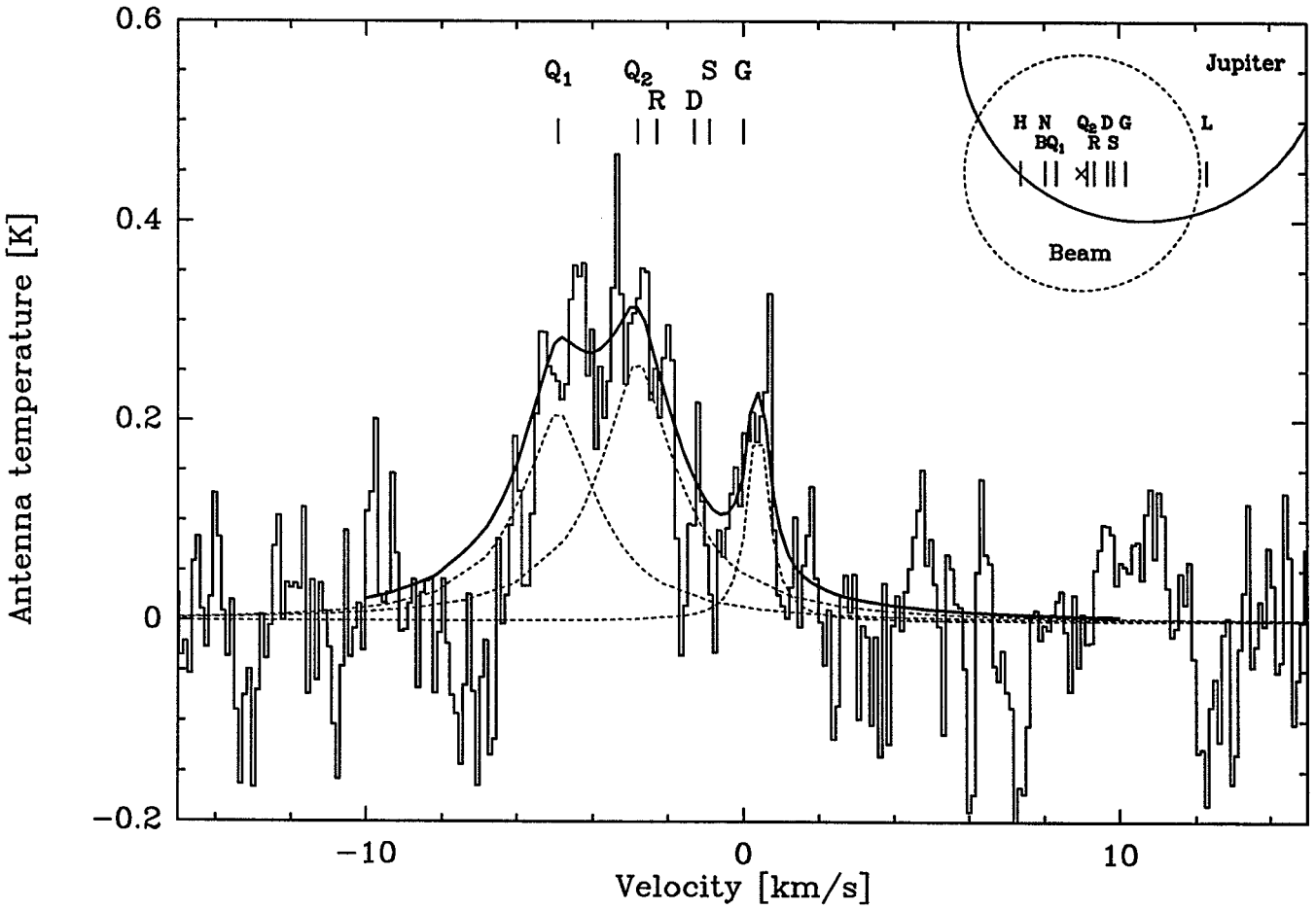

Figure 1: *The J(2–1) line of CO at 230.538 GHz detected on site D+G+Q_1+Q_2+R+S on July 23.81 at the SEST telescope. The integration time is 36 minutes. The geometry of the observations is shown in the right upper corner of the figure. Due to the rapid rotation of Jupiter, the geocentric velocities of the impacts differ. The velocity scale refers here to the velocity of impact G. Impact sites D, Q_1, Q_2, R and S were expected at respectively –1.3, –4.9, –2.8, –2.3, and –0.9 km/s at the moment of the observation. Note that the global shape of the line depends critically on the velocity corrections applied before co-adding the individual scans, due to the rapid and non-linear velocity displacement of the impact sites as Jupiter rotates. Superimposed is shown a model fit (full continuous line). Three emitting regions were modeled: Q_1, Q_2 and G (dashed lines). For line calibration, the diameter of each emitting region was assumed to be 2.5" (9400 km). Taking into account the beam efficiency and width, the dilution factor which converts observed antenna temperatures into brightness temperatures is 200. The continuum level originates from the troposphere where the disk-averaged brightness temperature is near 170 K and the opacity is due to H_2–He pressure-induced absorption. For each impact site, we assume a uniform temperature difference relative to pre-impact conditions and a constant CO mixing ratio q_{CO} above a pressure level determined by the linewidths, assumed to be due to pressure-induced collisions. For impact G, we adopt $\Delta T = 30$ K at $p \leq 2$ mbar and $q_{CO} = 4 \times 10^{-5}$ at $p \leq 0.1$ mbar. For impact Q_1, $\Delta T = 30$ K and $q_{CO} = 4 \times 10^{-5}$ at $p \leq 0.4$ mbar. For Q_2, $\Delta T = 40$ K and $q_{CO} = 4 \times 10^{-5}$ at $p \leq 0.4$ mbar. This fit is illustrative, since the solution is from being unique. In particular, impact site R, close to Q_2, was not taken into account. Similar fits can be obtained by assuming increased temperature gradients and lower mixing ratios, and vice versa. The retrieved CO masses are here 1.3×10^{14} g for Q_1 and Q_2, and 3×10^{-13} g for G.*

results of model calculations for a multi-site emission. For each impact site, we have assumed emitting region diameters of 2.5" (9400 km), in order to take into account the dilution within the beam. The model parameters are an excess temperature of 30–40 K above the normal 170 K temperature and a CO mixing ratio of 4×10^{-5} above the 0.1 mbar (impact G) or 0.4 mbar (impacts Q_1 and Q_2) levels. This fit is only illustrative and the solution is far from being unique. Emission due to impact R, close to Q_2, was not included. A somewhat higher temperature and lower mixing ratio would equally fit the results, and vice versa. The present solution implies CO masses on the order of 10^{14} g for each impact site, consistent with the conclusions of Lellouch et al. (1995) derived from the IRAM data.

4. Discussion

The detection of CO in the stratosphere of Jupiter will provide strong constraints on the physics of the impacts. CO has normally a very low abundance in Jupiter's atmosphere. The derived abundance is about 50,000 times larger than the normal tropospheric abundance, making unlikely that we were observing jovian CO transported in the plume. Since the high temperatures in the fireball are expected to dissociate most of the cometary and Jovian material, shock chemistry seems to provide the most plausible explanation for the formation of CO. The inferred amount of CO is quite comparable to the oxygen expected in a 1-km sized cometary nucleus. The millimetre observations provide in addition almost unique information on the thermal structure of the Jovian stratosphere modified by the impacts and its temporal evolution. The monitoring of millimetre lines of CO, CS and the HCN line indicated that a substantial warming occurred after the impacts and persisted over one week (Lellouch et al., 1995; Marten et al., 1995). Then the lines switched over from emission to absorption, indicating important cooling down to temperatures lower than the pre-impact values (Lellouch et al., 1995; Marten et al., 1994, 1995). The SEST observations, together with the other millimetre observations, will help to better understand this unique event.

References

Lellouch, E., Encrenaz, T., Combes, F., Drossart, P.: 1984, *Astronomy and Astrophysics* **135**, 365-370.

Lellouch, E., Paubert, G., Moreno, R., Festou, M.C., Bézard, B. et al.: 1995, *Nature* (in press).

Marten, A., Moreno, R., Paubert, G., Wild, W., Colom, P. et al.: 1994, *BAAS* **26**, 1589–1590.

Marten, A., Gautier, D., Owen, T., Griffin, M.J., Matthews, H.E. et al: 1995, *Geophysical Research Letter* (submitted).

Paubert, G., Gautier, D., and Courtin, R.: 1984 *Icarus*, **60**, 599–612.

West, R.M.: 1994, *The Messenger*, **77**, 28–31.

Wink, J., Lucas, R., Guilloteau, S., Dutrey, A.: 1994, *IRAM Newsletter* **18**,

For further information please contact:
D. Bockelée-Morvan;
e-mail: Dominique.Bockelee@obspm.fr

Evidence for Diffusely Distributed Dust in Elliptical Galaxies and its Effect on Radial Colour Gradients

P. GOUDFROOIJ, ESO-Garching

The presence of dust in elliptical galaxies has recently been shown to be quite common. Deep optical multi-colour CCD imaging has revealed the presence of dust lanes and patches, and the technique of co-adding IRAS survey scans has led to many detections of elliptical galaxies. The optical and far-infrared surveys reported similar detection rates of dust, which may indicate that dust in elliptical galaxies is generally distributed in the optically detected lanes or patches. However, we show here that the amount of dust as derived from the optical extinction values is typically an order of magnitude smaller than that derived from the IRAS flux densities, in strong contrast with the situation in spiral galaxies. To unriddle this dilemma, we postulate that the majority of the dust in elliptical galaxies exists as a diffusely distributed component which is undetectable using optical methods. Employing a multiple scattering model for the dust, we show that the presence of this newly postulated dust component implies significant radial colour gradients which were essentially thought to arise from stellar population gradients only. The energetics of the diffusely distributed dust component is shown to be consistent with the IRAS data. A comparison of the detectable amount of dust in elliptical galaxies embedded in hot, X-ray-emitting gas with the amount expected in case the production and destruction rates of dust are equal indicates that most of the dust in elliptical galaxies has been accreted from other galaxies.

1. Introduction

Although elliptical galaxies generally do not exhibit the large amounts of interstellar matter (ISM) typically found in spiral galaxies, it has recently become possible to detect various components of the ISM in elliptical galaxies (see, Roberts et al. 1991; Goudfrooij et al. 1994b). These studies have shown that the presence of dust and gas in elliptical galaxies is the rule rather than the exception.

Besides detecting the interstellar matter, we are interested in its origin and fate since this material is expected to hold clues to the formation and subsequent evolution of elliptical galaxies through both the physical properties and the dynamics of the gas and dust. There are at least two possible sources of the observed ISM: accumulation of material shed by evolved, mass-losing giant stars within the galaxy (e.g., Faber & Gallagher 1976; Knapp et al. 1992), and accretion of gas during galaxy interactions.

In order to systematically study the global occurrence and properties of dust and gas in elliptical galaxies, we (P. Goudfrooij from ESO, L. Hansen and H.E. Jørgensen from the Copenhagen University Observatory, H.U. Nørgaard-Nielsen from the Danish Space Research Institute, and T. de Jong from the University of Amsterdam) have performed an optical survey of a complete, *apparent*-magnitude selected sample of elliptical galaxies, containing all such objects (56 in number) with $B_T^0 < 12$ mag. in the *Revised*

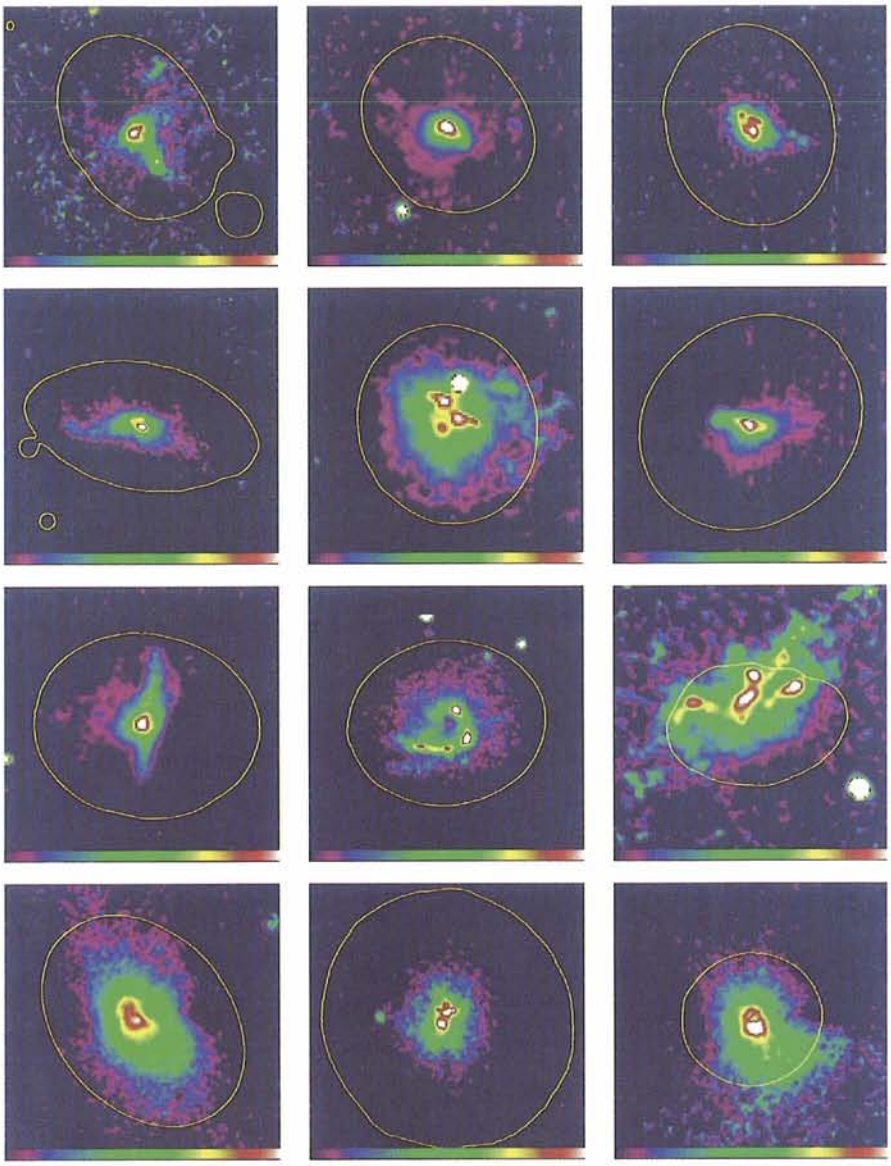

Figure 1: *B–I colour index images of (top left to bottom right) NGC 3136, IC 3370, NGC 3962, NGC 4125, NGC 4278, NGC 4374, NGC 4589, NGC 4696, NGC 5018, IC 1459, NGC 5044, and NGC 7507. For each galaxy, the B-band isophotal contour at half a de Vaucouleurs' effective radius (R_e) is superposed (except for NGC 4696 and NGC 5044, where the contour at $R_e/4$ is superposed). Dust shows as reddened structures with a morphology different from the isophote(s) of (stellar) galaxy light. The colour look up table is displayed at the bottom of each image.*

Shapley-Ames Catalog of Bright Galaxies (hereafter RSA catalog; Sandage & Tammann 1981). Deep CCD imaging has been performed through both broad-band filters and narrow-band filters isolating the nebular Hα+[NII] emission lines. For this we used the Dutch 0.91-m, Danish 1.54-m and ESO/MPI 2.2-m telescopes at ESO-La Silla for the southern galaxies, and the 1.0-m Jacobus Kapteyn telescope on the Canary island La Palma for the northern galaxies. Due to the size of the sample, the survey took several years to complete. The surface photometry and the isophotal properties of the sample galaxies are presented in Goudfrooij et al. (1994a, hereafter Paper I); distributions of dust and ionized gas are presented in Goudfrooij et al. (1994b, hereafter Paper II). Extinction properties of dust in selected dusty elliptical galaxies are presented in Goudfrooij et al. (1995, hereafter Paper III), where dust masses are also estimated from the optical extinction data.

1.1 Optical and far-infrared signatures of dust in elliptical galaxies

Optical CCD imaging is essential in establishing the presence and distribution of ISM in ellipticals in view of its high spatial resolution. However, quantitative estimates of the mass and the physical conditions of the dust from optical data alone are hampered by serious selection effects. This can be illustrated as follows: The optical methods for detecting dust in elliptical galaxies take advantage of the smooth distribution of the stellar light of these galaxies. Thus, only dust distributions that are sufficiently distinct from that of the stellar light (i.e., dust lanes, disks, or patches) can be detected. Examples of dust in elliptical galaxies in our "RSA sample" are shown in Figure 1.

In Paper II, we reported an (optical) detection rate of dust features in our RSA sample of 41 %. However, the ability to detect dusty disks or lanes in elliptical galaxies by these methods depends heavily on orientation effects, i.e., is biased towards edge-on dust distributions. The actual fraction of ellipticals containing dust features may thus be much higher (cf. Paper II; Sadler & Gerhard 1985). Furthermore, a significant fraction of the dust in elliptical galaxies may be expected to follow a smooth distribution similar to that of the stars (e.g., dust which is produced by mass-loss from late-type giant stars within the galaxies), but this dust remains undetected by optical methods.

The means to study dust in galaxies in a more quantitative way became available with data provided by the InfraRed Astronomical Satellite (IRAS). Since the dust opacity is low in the far-infrared, orientation effects do not influence the detectability of dust, thus allowing quantitative estimates of the temperature and total mass of the dust. Using the technique of co-adding IRAS survey scans, Knapp et al. (1989) have shown that a significant fraction ($\gtrsim$50 %) of nearby, bright E and S0 galaxies have been detected at 60 and 100 μm at a limiting sensitivity about 3 times lower than in the IRAS Point Source Catalog. Although this detection rate is similar to that of the optical methods, recent studies of individual elliptical galaxies have shown that estimates of the total mass of dust using the IRAS data are a factor of ~ 10 higher than those derived from optical colour excesses integrated over the areas where dust is found to reside (de Jong et al. 1990; Hansen et al. 1991). To address the discrepancies mentioned above, we combine in this paper our optical survey data with the IRAS data to analyse physical properties of dust in elliptical galaxies, including the distribution of the dust and heating mechanisms for the dust. A more elaborate version of this paper will be published elsewhere (Goudfrooij & de Jong 1995, hereafter Paper IV).

2. The Distribution of Dust in Elliptical Galaxies

2.1 Dust masses from optical and far-infrared data: the "Dust Mass Discrepancy"

The methods used for deriving dust masses from optical extinction values and from the IRAS flux densities are explained in detail in Papers III and IV. In summary,

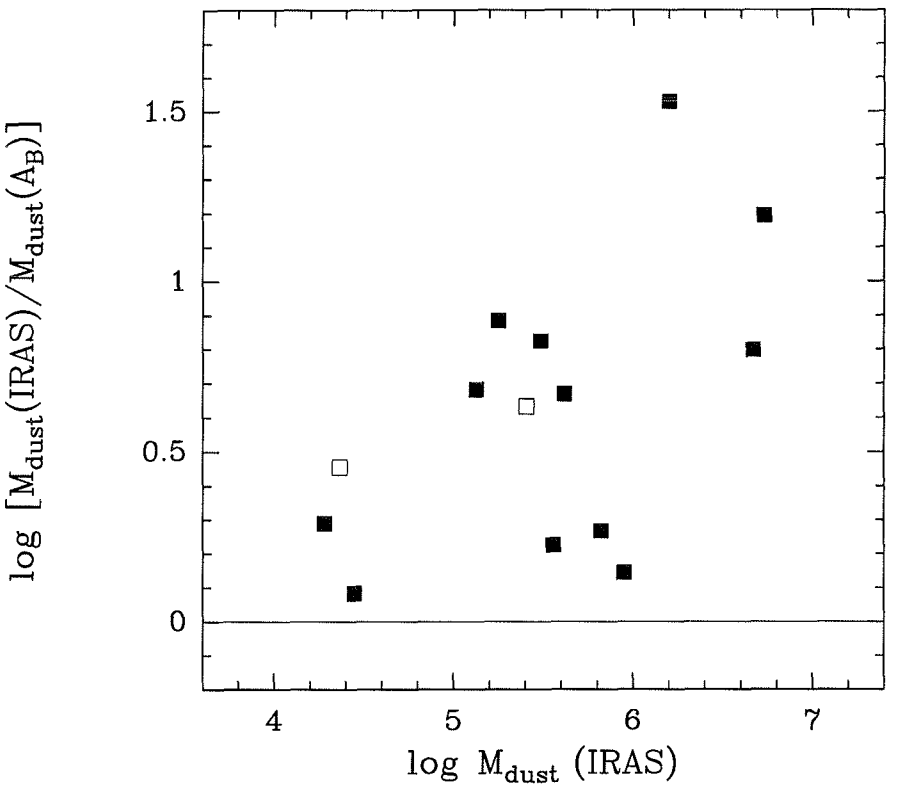

Figure 2: *The quotient of the dust mass derived from the IRAS data and the dust mass derived from optical extinction versus the dust mass derived from the IRAS data for elliptical galaxies from the "RSA sample" with optically detected dust. Filled squares represent galaxies detected by IRAS at both 60 and 100 μm, and open squares represent galaxies detected in only one IRAS band.*

optical extinction values are converted into dust mass column densities by adopting the Mathis et al. (1977) grain size distribution function and optical extinction efficiency factors taken from the literature; the IRAS 60 and 100 μm flux densities are used to determine dust masses under the assumption that the far-infrared emission of elliptical galaxies originates from dust with an emissivity law $\propto \lambda^{-1}$ at the wavelength region covered by IRAS. We assume the 60 and 100 μm emission to be due to a single-temperature component of dust. Thus, derived dust temperatures should be regarded as "representative" values, since a *range* of temperatures is appropriate for dust within elliptical galaxies. We note that IRAS is sensitive to "cool" dust with $T_d \gtrsim 25$ K, but much less to "cold" dust with lower temperatures emitting predominantly at wavelengths far beyond 100 μm (e.g., Young et al. 1986). We will see below that temperatures of order 20 K are appropriate to the outer regions of elliptical galaxies (i.e., beyond ~10 kpc), so that the dust masses calculated from the IRAS data are in principle (firm) lower limits to the real dust mass. In the following, we thus only consider the component of dust which radiates at wavelengths covered by IRAS.

A glance at Figure 2 reveals that the dust masses estimated from the optical extinction are significantly lower than those estimated from the far-infrared emission. Quantitatively, the average ratio $< M_{d,\,IRAS}/M_{d,\,opt} > = 8.4 \pm 1.3$ for the galaxies in our "RSA sample" for which the presence of dust is revealed by both far-infrared emission and optical dust lanes or patches. Strictly speaking, the dust masses derived from optical extinction are lower limits since the conversion factor from extinction to dust mass implicitly assumes the dust to be in front of the stars. Since the dust is probably embedded in the stellar systems, the optically derived dust masses may be of order 2 times higher than the calculated values. However, the disagreement between the two mass determinations is significant.

This disagreement might (partly) be due to the effect of orientation. In Paper II we reported that estimated inclinations of regular dust lanes in early-type galaxies are found to range between 0 and ~ 35°, suggesting that dust lanes are detected only if inclined by less than a certain critical angle. If this were correct, the ratio $M_{d,\,IRAS}/M_{d,\,opt}$ (hereafter "dust mass discrepancy") would be expected to be inversely proportional to cos (i), where i is the inclination of the dust lane

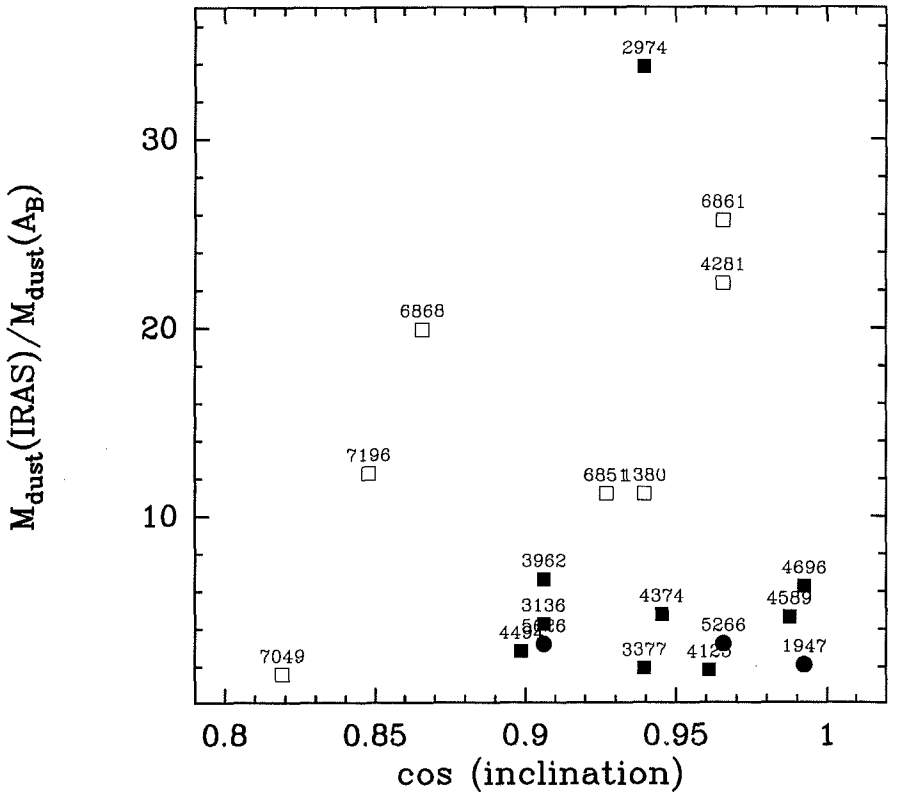

Figure 3: *The quotient of the dust mass derived from the IRAS data and the dust mass derived from optical extinction versus the cosine of the inclination angle of the dust lane in selected elliptical galaxies containing regular dust lanes. Filled squares represent galaxies from the "RSA sample", filled circles represent galaxies from Paper III, and open squares represent galaxies from the sample of Véron-Cetty & Véron (1988). The NGC numbers of the galaxies involved are indicated above the symbols.*

with respect to the line of sight. To evaluate the influence of the effect of orientation on the dust mass discrepancy, we estimated the inclinations of (apparently) regular, uniform dust lanes in elliptical galaxies from images shown in homogeneous optical CCD surveys (Paper II; Paper III; Véron-Cetty & Véron 1988). The dust masses derived from the optical reddening by Véron-Cetty & Véron were scaled up by 10 % proportional to the difference of the adopted dust mass column densities (cf. Paper III). The relation between $M_{d,\,IRAS}/M_{d,\,opt}$ and cos (i) is shown in Figure 3. This being a scatter plot, the effect of orientation on the dust mass discrepancy must be weak if present at all. This suggests that the dust in the lanes is concentrated in relatively small, dense clumps with a low volume filling factor.

2.2 Diffusely distributed dust: dilemma unriddled?

Having eliminated the effect of orientation, the most plausible way out of the dilemma of the dust mass discrepancy is to postulate an additional component of dust with a diffuse, uniform distribution over a large area in elliptical galaxies and therefore virtually undetectable by optical methods. We note that this diffuse component of dust is not unexpected in elliptical galaxies. For instance, the late-type stellar population of typical giant ellipticals ($L_B = 10^{10} - 10^{11}\,L_\odot$) has a substantial present-day mass loss rate (~ 0.1 – 1 $M_\odot\,yr^{-1}$ of gas and dust; cf. Faber & Gallagher 1976) which is expected to be diffusely distributed.

An interesting potential way to trace this diffuse component of dust is provided by radial colour gradients in elliptical galaxies. With very few significant exceptions, "normal" elliptical galaxies (e.g., the galaxies in our RSA sample) show a global reddening toward their centres (see Paper I and references therein). These colour gradients are generally being explained in terms of metallicity variations. This view is supported by the existence of radial gradients of metallic absorption line strengths (Davies et al. 1993; Carollo et al. 1993). There is however significant scatter in the relation between colour gradients and line strength gradients (cf. Peletier 1989; Davies et al. 1993). Although the presence of dust in elliptical galaxies is now beyond dispute, the implications of dust extinction are generally discarded in the interpretation of colour gradients. However, recent model calculations of the transfer of stellar radiation within elliptical galaxies by Witt et al. (1992, hereafter WTC) have demonstrated that a diffuse distribution of dust throughout ellipticals can cause significant colour gradients even with modest dust optical depths, without significantly changing the observed global colours.

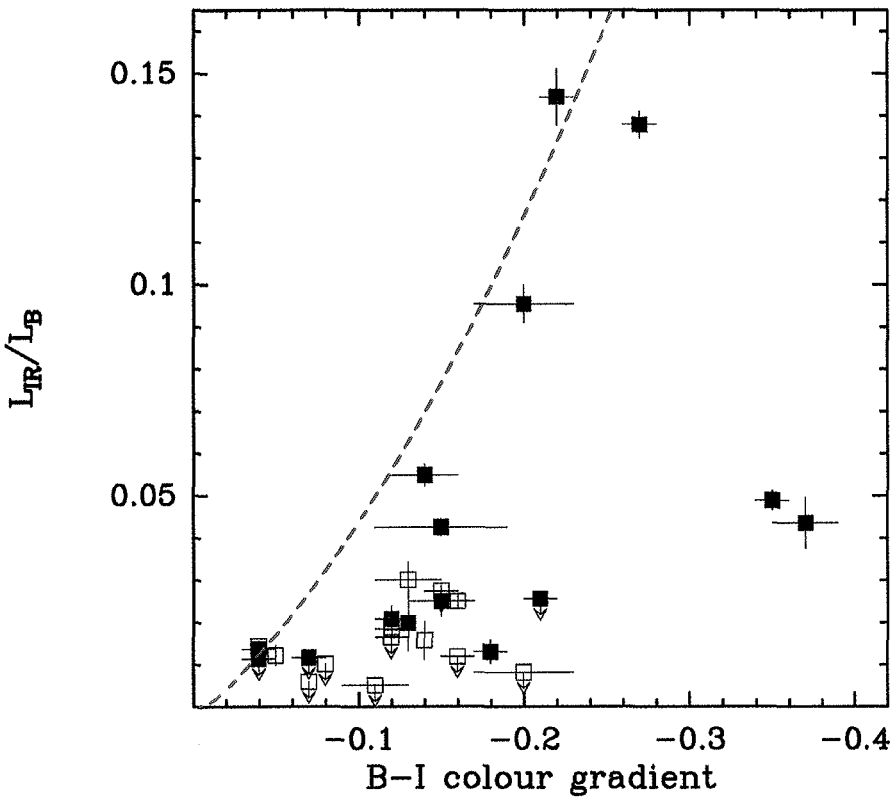

Figure 4: *The relation of L_{IR}/L_B with the radial B–I colour gradients (defined as Δ(B–I)/Δ(log r)) for elliptical galaxies in the "RSA sample". Filled squares represent galaxies detected by IRAS showing optical evidence for dust, and open squares represent galaxies detected by IRAS without optical evidence for dust. Arrows pointing downwards indicate upper limits to L_{IR}/L_B. The red dashed line represents the colour gradient expected from differential extinction by a diffuse distribution of dust (see text).*

We have exploited the elliptical galaxy model described by WTC to derive the predicted colour gradients – due to dust alone – appropriate to the far-infrared properties (and hence the dust content) of the elliptical galaxies in the RSA sample. The Monte Carlo simulations of WTC exploit a spherically symmetric distribution of stars, uniformly mixed with a diffuse, homogeneous distribution of dust. The predicted radial colour gradients are due to the effect of differential extinction (i.e. absorption *and* scattering) throughout the galaxy. The model of WTC reproduces a de Vaucouleurs surface brightness profile quite well, even for relatively high total optical depths of the dust distribution. Substantial amounts of dust can thus be present in (elliptical) galaxies while remaining undetected by conventional optical methods. Using the model computations of WTC, infrared to blue luminosity ratios L_{IR}/L_B and colour gradients [e.g., Δ(B–I)/Δ(log r)] have been derived as a function of the total dust optical depth τ_V of the diffuse dust component.

The result is plotted (as a dashed line) in Figure 4 in which the L_{IR}/L_B ratios of the galaxies in the RSA sample that are detected by IRAS are plotted versus their radial B–I colour gradients (taken from Paper I). Although Figure 4 shows that colour gradients in elliptical galaxies are generally larger than can be generated by a diffuse distribution of dust throughout the galaxies according to the model of WTC, it is obvious that the relation implied by the model of WTC fits the *minimum* of the distribution of colour gradients at a given L_{IR}/L_B quite well. Moreover, there are *no* galaxies in the RSA sample with a colour gradient significantly *smaller* than that indicated by the model of WTC. This result strongly suggests the presence of a diffuse distribution of dust in elliptical galaxies, causing a colour gradient due to differential extinction. This effect should be added to the effects of metallicity and/or age gradients of the stellar population in the interpretation of observed colour gradients of elliptical galaxies.

We have investigated whether published radial metallicity gradients (i.e., radial gradients of the Mg_2 index) of galaxies in the RSA sample are consistent with the positions of the galaxies in Figure 4. Although there are currently only a few galaxies in the RSA sample for which radial metallicity gradients have been published, it is quite reassuring that the galaxies in Figure 4 which lie nearest to the relation implied by the model of WTC

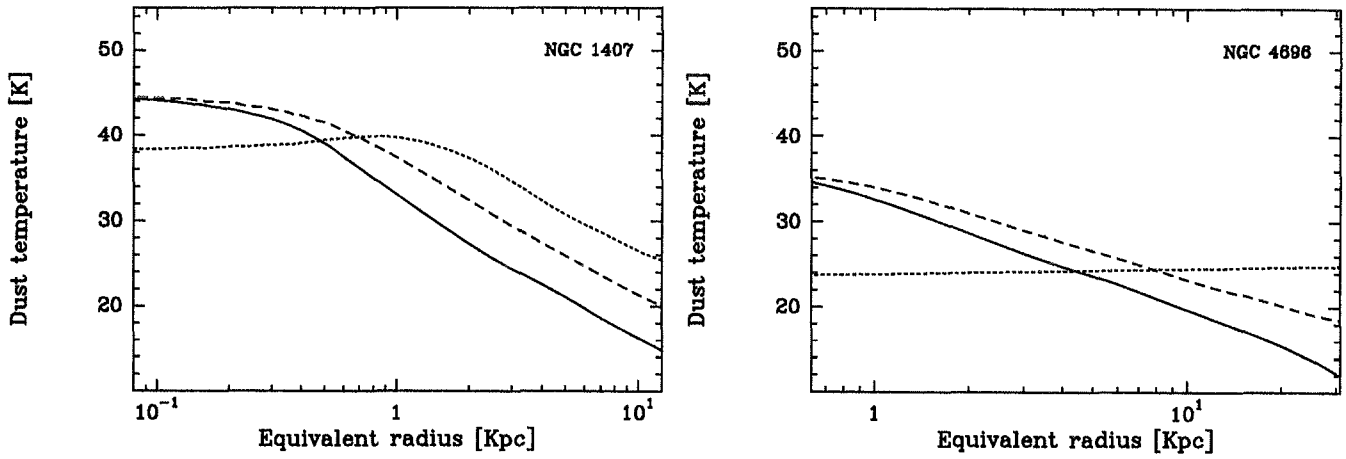

Figure 5: *Radial profiles of the local dust temperature due to optical heating (solid line), the average dust temperature inside a given radius due to optical heating (dashed line), and the average dust temperature due to heating by "hot" electrons in X-ray-emitting gas (dotted line) versus galactic radius in kpc for the elliptical galaxies NGC 1407 and NGC 4696. A mixture of graphite and "dirty silicate" (Jones & Merrill 1976) grains of radius 0.1 μm is assumed.*

have metallicity gradients which are among the smallest of the published values (e.g., NGC 3136, log d(Mg_2)/dr = -0.035 ± 0.011; IC 3370, log d(Mg_2)/dr = -0.026 ± 0.010 (Carollo et al. 1993)).

2.3 Radial dust temperature distribution

To check whether the assumption of the presence of a diffuse, uniformly distributed component of dust in elliptical galaxies is energetically consistent with the available IRAS data, we have investigated plausible heating mechanisms for the dust:

Heating by stellar photons: Using the extensive radial surface brightness profiles of the galaxies in our sample (Paper I), we have calculated radial profiles of the average intensity of optical radiation, from which the heating rate of a dust grain can be derived as a function of galactocentric radius (again assuming grain extinction efficiency factors from the literature; cf. Paper IV).

Heating by hot electrons in X-ray-emitting gas: Observations with the EINSTEIN X-ray satellite have shown that a substantial number of elliptical galaxies in our sample are embedded in a hot T ~ 10^7 K), X-ray-emitting gas (e.g., Fabbiano et al. 1992). The presence of this hot gas has important implications for the dust grains. Collisions of dust grains with protons and α-particles in the hot gas destroy the dust by sputtering (Draine & Salpeter 1979a) while collisions with "hot" electrons provide a potentially important heating mechanism for the dust grains (e.g., de Jong et al. 1990). The measured X-ray surface brightness profiles of elliptical galaxies containing hot gas are generally consistent with a "King-like" distribution (The "beta model", Cavaliere & Fusco-Femiano 1976) Using the prescriptions given by Canizares et al. (1987) which relate the central electron density to the total X-ray luminosity and the X-ray core radius, we compute radial electron density profiles (and, hence, dust heating rates, cf. Paper IV) according to the "beta model" for the galaxies in the RSA sample which are detected by EINSTEIN.

Heating by X-ray photons: From the X-ray luminosities of the hot gas and the core radii mentioned above we derive average X-ray intensities in the core region, and thus heating rates for the dust. For typical values for the X-ray luminosity (~10^{41} erg s^{-1}) and the core radius (~ 2 kpc) we obtain a heating rate by X-rays that is at least two orders of magnitude smaller than the heating rate by optical photons for all galaxies in our sample. The heating of dust by X-rays can thus safely be neglected in elliptical galaxies.

Dust temperatures are derived by equating the heating rate to the cooling rate of a dust grain by infrared emission,

$$L_d = 6.0\ 10^{-8}\ k_{IR}\ m_d\ T_d^5 \text{ erg s}^{-1}$$

(de Jong et al. 1990) where κ_{IR} is the dust opacity in the infrared and m_d is the mass of a dust grain. Relevant physical parameters for dust grains are taken from Hildebrand (1983).

Examples of the distribution of local and average temperature as a function of equivalent radius (which is defined as $\sqrt{ab} = a\sqrt{1-\varepsilon}$, where a and b are the semi-major and semi-minor axes of the elliptical isophote of the galaxy, and ε its ellipticity) are shown in Figure 5 for two elliptical galaxies which are detected at both X-ray and far-infrared wavelengths. In general, the dust temperatures as derived from the IRAS data are found to be compatible with those calculated for a diffuse distribution of dust within the inner few kpc.

2.4 Properties of the diffusely distributed dust component

In this Section we investigate whether the dust optical depths of the postulated diffuse component of dust in elliptical galaxies as derived from the WTC model are consistent with the observed IRAS flux densities. To this end, we derive the mass and infrared luminosity of the diffusely distributed component of dust and compare the dust temperature implied through application of the model of WTC and the radial temperature profiles derived above with the temperature derived directly from the IRAS flux densities. Note that the dependence of the infrared *luminosity* (as derived from the 60 and 100 μm flux densities, cf. JISWG 1986) on the dust temperature is negligible compared to that of the dust *mass*. We limit ourselves to the elliptical galaxies in the RSA sample which are detected at ≥ 2 σ at both the 60 and 100 μm wavelengths (cf. Knapp et al. 1989).

The derivation of the contribution of the different components of dust in these galaxies to the IRAS flux densities using our derived radial temperature distributions was done in the following way:

1. We first estimated the contribution of the optically visible dust component (if present) to the IRAS flux densities. In case of irregular (patchy) dust, this was done by extracting independent, rectangular box-shaped pieces of dust features, comparable in size with the seeing profile. Temperatures, and hence flux densities at 60 and 100 μm were calculated for these elements of dust features according to their average (projected) distance from the centre of the galaxy (cf. Fig. **2?**). Apparently regular dust lanes were assumed to be circular disks of uniform density, reaching down to the centre of the galaxy.

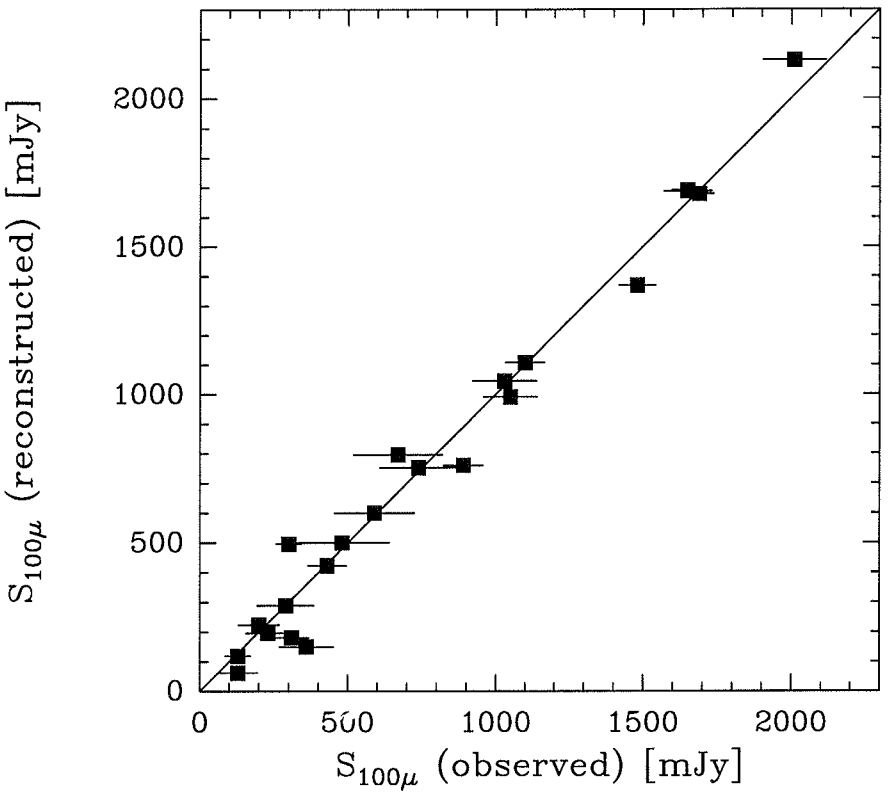

Figure 6: *The 100μm flux densities reconstructed from our calculations of the dust temperatures in elliptical galaxies (as described in the text) versus the observed 100 μm flux densities. The solid line connects loci with "reconstructed = observed".*

2. After subtracting the contribution of the optically visible component of dust (if present) to the IRAS flux densities, the resulting flux densities were assigned to the postulated diffuse dust component; for the ellipticals in which no optical evidence for the presence of dust was found, the *total* IRAS flux densities were assigned to the diffuse dust component. Dust masses and infrared luminosities of the diffusely distributed dust component were subsequently calculated.

3. From the L_{IR}/L_B ratio of the diffuse dust component, radial colour gradients and, by implication, total optical depths in the V band were derived according to the model of WTC (cf. Fig. 4). Dust mass column densities were subsequently computed for the diffuse dust component from the total optical depths τ_V (cf. Paper III).

4. Dividing the implied masses of the diffuse dust component by the dust column densities, outer equivalent radii of the postulated diffuse dust component were derived for each galaxy. Typical values for the outer radii were of the order of 2 kpc.

5. IRAS flux densities at 60 and 100 μm for the diffuse dust component were subsequently constructed from the masses of the diffuse dust component by integrating over spheres. Finally, the average temperatures of the diffusely distributed dust were calculated from these resulting IRAS flux densities.

A comparison of the observed and reconstructed IRAS flux densities (cf. Fig. 6) reveals that the *observed* IRAS flux densities can in *virtually all elliptical galaxies in the RSA sample* be reproduced *within the 1 σ uncertainties* by assuming two components of dust in elliptical galaxies: an optically visible component in the form of dust lanes and/or patches, and a newly postulated dust component which is diffusely distributed within the inner few kpc from the centre of the galaxies.

Heating of the dust by optical photons is found to be generally sufficient to account for the observed dust temperatures as derived from the IRAS flux densities, in contrast to conclusions drawn by previous studies of cool interstellar matter in elliptical galaxies (e.g., Brosch 1987).

We remind the reader that we have only considered dust which radiates at wavelengths covered by IRAS, i.e., with temperatures $\gtrsim 25$ K. In reality, the postulated diffuse component of dust in elliptical galaxies may generally be expected to extend further out than a few kpc. Future observations with the Infrared Space Observatory (ISO) of the RSA sample of elliptical galaxies are foreseen and may reveal this cooler dust component in elliptical galaxies.

3. Origin of the Different Components of Dust

As to the origin of cool interstellar matter in elliptical galaxies, a consensus is developing that dust in these systems *always* has an external origin, i.e., accreted during a galaxy merger or interaction. For instance, spectroscopic studies of the velocity fields of gas and stars in elliptical galaxies with dust lanes show that the gas which is associated with the dust lanes is generally dynamically de-coupled from the stellar body, i.e., in disks rotating at random orientations with respect to the apparent major axis of the elliptical galaxy (e.g., Kormendy & Djorgovski 1989 and references therein). Since it is difficult (if not impossible) to envision an evolutionary scenario for a *primordial* galaxy in which gaseous and stellar components become dynamically decoupled, this strongly suggests an external origin for the dust and gas.

Other important evidence in favour of an external origin of the dust and gas is provided in several cases of X-ray-emitting elliptical and cD galaxies with suspected cooling flows. These galaxies often contain extended regions of ionized gas which have been argued to arise as condensations in thermally instable regions in the cooling flow (see, e.g., Fabian et al. 1991).

The lifetime of a dust grain against collisions with hot protons and α-particles ("sputtering") in a hot gas with $T_e \sim 10^7$ K is of the order of only 10^6–10^7 yr (Draine & Salpeter 1979a). Hence, the emission-line filaments in these galaxies are expected to be dust-free. This is illustrated by the finding that the intergalactic medium within the Coma cluster is depleted in dust by a factor of ~ 140 with respect to the Galactic dust-to-gas ratio (Dwek et al. 1990).

However, dust *has* been found to be quite commonly associated with filaments of ionized gas in these galaxies (Paper II and references therein).

Although the evidence mentioned above provides a strong case for an external origin of dust in elliptical galaxies, these arguments are all based on the *optically visible component* of dust, which, as we have seen, only accounts for $\lesssim 10$ % of the total amount of dust in elliptical galaxies. So the question arises: What is the origin of the postulated diffusely distributed component of dust?

In Figure 7 we show the relationship of the dust mass (of the *diffusely distributed component*) derived from the IRAS data with the blue luminosities of the galaxies in the RSA sample. The dashed lines in Figure 7 connect the loci where all dust could have an internal origin, i.e., replenished by stellar mass loss at the

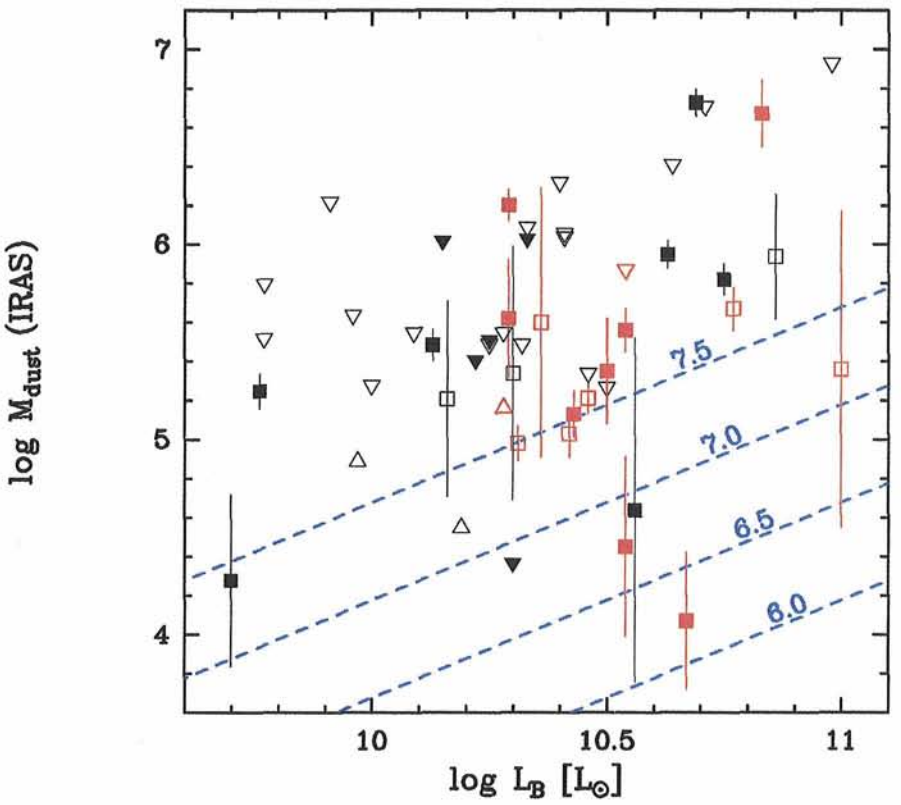

Figure 7: *The relationship of the mass of cool dust (as derived from the IRAS 60 and 100 μm flux densities) and the blue luminosity of elliptical galaxies in the RSA sample. Filled symbols represent galaxies with optically visible dust lanes and/or patches, whereas open symbols represent galaxies in which no sign of optical extinction has been found. Triangles pointing up- or downwards represent galaxies which are detected by IRAS at either 100 or 60 μm only, respectively. Red symbols represent galaxies with detected X-ray emission from hot gas. The position of M 87 is marked. The dashed lines connect loci where dust is replenished by stellar mass loss, and destroyed by sputtering at the given time scale (in dex), as discussed in the text.*

rate given by Faber & Gallagher (1976) and destroyed by (e.g.) sputtering, for different values of the destruction time scale τ_d. We adopted a gas-to-dust ratio of 100. The line with $\tau_d = 10^{7.5}$ yr should be regarded as a maximum destruction time scale in ellipticals known to contain hot, X-ray-emitting gas, since the electron density exceeds 5 10^{-3} cm^{-3} in the inner ~ 10 kpc of all galaxies studied in sufficient detail (e.g., Canizares et al. 1987). As Figure 7 shows, most elliptical galaxies in the RSA sample in which X-ray emission has been detected contain more dust than can be accounted for by stellar mass loss alone. This favours the view that the dust in elliptical galaxies generally has an external origin.

As can be seen in Figure 7, we confirm the absence of a correlation between the mass of dust and the blue luminosity of elliptical galaxies (cf. Forbes 1991). On first sight, this indicates that there is no causal relationship between the dust content and the present-day population of stars within elliptical galaxies, in contrast with the situation in spiral galaxies (e.g., Young et al. 1989), which would again suggest that dust in elliptical galaxies has an external origin. However, this conclusion is somewhat premature since the typical dust destruction time scale in elliptical galaxies is expected to be significantly different among individual objects.

Among the various destruction mechanisms for dust grains in the interstellar medium, sputtering in hot, X-ray-emitting gas is by far the most effective one (Draine & Salpeter 1979a, b; Paper III). The fate of dust within elliptical galaxies is therefore mainly determined by the presence of hot, X-ray-emitting coronal gas and its physical properties (i.e., radial temperature and density profiles). However, the present status of knowledge of these important matters is quite limited, since e.g., most of the galaxies in the RSA sample have not been observed by the EINSTEIN satellite. Future analysis of the ROSAT all-sky survey data and, especially, the gain in sensitivity and spectral resolution of the ASCA satellite should be very valuable in determining typical destruction time scales for dust in elliptical galaxies.

Acknowledgements

We would like to express our gratitude to the European Southern Observatory, the Panel for Allocation of Telescope Time, and the Danish Board for Astronomical Research for their generous allocation of observing time to this project.

References

Brosch N., 1987, *MNRAS* **225**, 257.
Canizares C. R., Fabbiano G., Trinchieri G., 1987, *ApJ* **312**, 503.
Carollo C. M., Danziger I. J., Buson L. M., 1993, *MNRAS* **265**, 553.
Cavaliere A., Fusco-Femiano R., 1976, *A&A* **49**, 137.
Davies R. L., Sadler E. M., Peletier R. F., 1993, *MNRAS* **262**, 650.
de Jong T., Nørgaard-Nielsen H. U., Hansen L., Jørgensen H. E., 1990, *A&A* **232**, 317.
Draine B. T., Salpeter E., 1979a, *ApJ* **231**, 77.
Draine B. T., Salpeter E., 1979b, *ApJ* **231**, 438.
Dwek E., Rephaeli Y., Mather J. C., 1990, *ApJ* **350**, 104.
Fabbiano G., Kim D.-W., Trinchieri G., 1992, *ApJS* **80**, 531.
Faber S. M., Gallagher J. S., 1976, *ApJ* **204**, 365.
Fabian A. C., Nulsen P. E. J., Canizares C. R., 1991, *A&AR* **2**, 191.
Forbes D. A., 1991, *MNRAS* **249**, 779.
Goudfrooij P., Hansen L., Jørgensen H. E., Nørgaard-Nielsen H. U., de Jong T., van den Hoek L. B., 1994a, A&AS 104, 179 (Paper I).
Goudfrooij P., Hansen L., Jørgensen H. E., Nørgaard-Nielsen H. U., 1994b, *A&AS* **105**, 341 (Paper II).
Goudfrooij P., de Jong T., Hansen L., Nørgaard-Nielsen H.U., 1995, *MNRAS*, in press (Paper III; ESO preprint No. 1027).
Goudfrooij P., de Jong T., 1995, *A&A*, in press (ESO preprint No. 1055).
Hansen L., Nørgaard-Nielsen H. U., Jørgensen H. E., 1991, *A&A* **243**, 49.
Hildebrand R. D., 1983, *QJRAS* **24**, 267.
Joint IRAS Science Working Group 1986, *Cataloged Galaxies and Quasars in the IRAS Survey*, JPL-D-1855 (JISWG).
Jones T. W., Merrill K. M., 1976, *ApJ* **209**, 509.
Knapp G. R., Guharthakurta P., Kim D.-W., Jura M., 1989, *ApJS* **70**, 329.
Knapp G. R., Gunn J. E., Wynn-Williams C. G., 1992, *ApJ* **399**, 76.
Mathis J. S., Rumpl W., Nordsieck K. H., 1977, *ApJ* **217**, 425.
Peletier R. F., 1989, Ph. D. Thesis, University of Groningen.
Roberts M. S., Hogg D. E., Bregman J. N., Forman W. R., Jones C., 1991, *ApJS* **75**, 751.
Sadler E. M., Gerhard O. E., 1985, *MNRAS* **214**, 177.
Sandage A. R., Tammann G. A., 1981, *A Revised Shapley-Ames Catalog of Bright Galaxies*, Carnegie Institution of Washington (RSA).
Véron-Cetty M. P., Véron P., 1988, *A&A* **204**, 28.
Witt A. N., Thronson H. A. jr., Capuano J. M., 1992, *ApJ* **393**, 611 (WTC).
Young J. S., Xie S., Kenney J. D. P., Rice W. L., 1989, *ApJS* **70**, 699.

For further information please contact:
P. Goudfrooij, ESO-Garching,
e-mail: pgoudfro@eso.org

Converging Computing Methodologies in Astronomy: A European Science Foundation Scientific Network, 1995–1997

NETWORK COORDINATION COMMITTEE (names below)

Introduction

A "Scientific Network" is the primary funding mechanism used by the European Science Foundation, which is based in Strasbourg. The word "network" is used here to mean a group of research teams and individuals, which aims at coordinating their research work through workshops and conferences, and work visits. A few dozen such "networks" are supported by the ESF at any one time. Such collaborative "networks" have in the past been set up in many areas, spanning the natural and human sciences. They have proven very successful, as springboards for productive work, with a relatively very restricted amount of administrative overhead.

An ESF "Scientific Network" on the topic of "Converging Computing Methodologies in Astronomy" is beginning in January 1995, and will extend over 3 years. As is usual in ESF collaborative networks, the administration of the network is carried out by a committee which is geographically representative.

The increasing integration in an astronomical setting of various methodologies in pattern recognition, information retrieval and data analysis is a characteristic of modern computational astronomy. Large astronomical data-bases and archives from space-borne missions, ground-based observatories, and large wide-field surveys, provide the technological infrastructure.

Against this backdrop, boundaries between theoretical domains have been lowered.

In this project, we wish to highlight and exploit convergence of methods and techniques.

From the astronomer's viewpoint, a coordinated global view of methods and techniques allows optimal exploitation of available information.

Network Activities

- *From vision models to image information retrieval*

Methods such as wavelets and multi-resolution approaches, mathe-matical morphology, and fuzzy methods have proven their worth in the framework of accessing appropriate information from large image databases. Use of such methods in this context is not a purely engineering task (i.e. simply providing them as stand-alone commands in an information retrieval framework). Rather, the methods must be moulded together to allow semantically-driven access to data. New methods, motivated by those mentioned, are required to handle the huge quantities of data which stand ready to be analysed.

Example: the Hubble Space Telescope image database contains roughly 80,000 2-dimensional and 1-dimensional images. Certain types of survey studies could benefit from the ability to access all images satisfying certain broadly-specified characteristics: e.g. objects close in appearance to a certain morphological shape; or objects of a certain morphology within a certain distance of one another. Can multi-resolution and fuzzy characterisation methods provide the basis for such retrieval requests?

- *The data life-cycle methodological aspects*

The astronomical data life-cycle is highly digital: data capture is increasingly on CCD electronic detectors, data are subject to image processing and statistical treatment, and the final major stage in this process involves (a) data archiving, and (b) publication. Not surprisingly, the issues of electronic publishing and of digital libraries are viewed as increasingly important. Data storage and access standards, together with interface standards, must be coordinated. Data characteristics, including dynamic aspects related to the life-cycle, strongly impact on methods for analysis and treatment.

Example: Image data are nowadays stored in many versions: raw; calibrated; compressed with loss of information, for quick-viewing; perhaps iconised; and we may add subsample-selected for data samplers and image processing test suites. Not only is coordination called for, among these incarnations of database contents; but – more than that – we must ask if other derivative products are needed, and are easily produced from the afore-mentioned chains of analysis and reduction.

- *From data integration to information integration*

– Particular data integration (data fusion) problems, such as integration of data associated with different wavelength ranges, are of great relevance in the context of large space- and ground-based observing projects. In certain instances, this takes the form of co-addition in image restoration. It also includes the enhancement of image restoration and fil-tering approaches through building-in semantic information on the cosmic objects of interest. Close, complementary use of multi-million object astronomical catalogues still has some distance to go in order to be tightly coupled with analysis of images from large image databases. Complementarity of such data rests on external information (semantics), and determines the appropriate analysis methodologies. Large-scale data integration prototypes have been pursued by NASA and ESA in recent years (respectively, the Astrophysical Data System, ADS; and the European Space Information System, ESIS), and these serve to point to 'issues and concerns' which are solvable through improved methods.

– Classification of terabyte (10^{12} bytes) data collections, which includes neural networks, decision/classification trees, and machine learning approaches. Widely reused code and paradigms has not yet evolved out of extensive astronomical work done in this area. Through coordination, this could be the case.

– Long-term access to stored data, and the selection of the latter. What should be, in the phrasing of M.J. Kurtz, 'the future of memory' (i.e. humanity's memory, which includes image data and other data)? Ever greater quantities of data are collected – what should be (expensively) stored, and how should this be done? Photographic plate directories exist, and policies based on a range of theoretical issues are required for scanning and maintenance. Major projects

collect many terabytes of data, and reuse is both necessary but also problematic.

– Beyond data, astronomy is all about information. Compression is a by-product of image models. Loss of information involved in compression raises a range of questions. In its broadest sense, compression is summarisation, and therefore is part of the overall process of scientific analysis.

Example: The costs of long-term data storage are large. With greater and better ground-based and space-borne observatories, these costs cannot be ignored. With our knowledge of, and expertise in, state-of-the-art and emerging computational technologies, what is our recommendation to the world's space agencies and observatories in regard to future policy?

These thematic themes of the Network will be axed around a series of workshops.

A conference on the Network's overall theme will be held shortly before the end of the Network, with the aim of bringing the results obtained to a wide audience. A selected set of papers will be published in book form.

The Coordination Committee and Contact Information

The Coordination Committee consists of:

A. Bijaoui, Observatoire de la Côte d'Azur, Nice (bijaoui@corelli.obs-nice.fr)

V. Di Gesù, Department of Mathematics and Applications, University of Palermo (digesu@ipamat.cres.it)

A. Heck, Observatoire Astronomique, Strasbourg (heck@cdsxb6.u-strasbg.fr)

M.J. Kurtz, Center for Astrophysics, Harvard (kurtz@cfa.harvard.edu)

P. Linde, Lund Observatory, Lund (peter@astro.lu.se)

M.C. Maccarone, IFCAI, Palermo (cettina@ifcai.pa.cnr.it)

R. McMahon, Institute of Astronomy, Cambridge (rgm@mail.ast.cam.ac.uk)

R. Molina, University of Granada (rms@ugr.es)

F. Murtagh, European Southern Observatory, Garching (fmurtagh@eso.org)

E. Raimond, Netherlands Foundation for Research in Astronomy, Dwingeloo (exr@nfra.nl), ESF representative

The Coordination Committee decides on administrative matters, but needless to say, many others will be involved. The Network Chair is

M.C. Maccarone (cettina@ifcai.pa.cnr.it),

and the Secretary is F. Murtagh(fmurtagh@eso.org).

Information on the Network can be obtained on the WWW at the address: http://www.hq.eso.org/conv-comp.html.

ESO on CompuServe

F. MURTAGH, ST-ECF, Garching

ESO press releases and a great deal of other ESO information are available on the World-Wide Web (URL: http://www.hq.eso.org/). For over a year, press releases including images are also available on CompuServe. They may be accessed in the Space/Astronomy area (GO SPACE).

CompuServe is a commercial information service, offering local access at many locations worldwide. Membership is about 2.5 million worldwide, of which around 170,000 are in Europe. A very large number of discussion groups and information libraries are available which span all subject domains. Other areas cater for weather images and forecasts, news-feeds from major agencies, a range of databases, and so forth. A number of user interfaces (browsers) are available which support access in a convenient manner, display of images and videos, e-mail, file management of download areas, and navigation through the varied services on offer. Access is often by modem, using dial-up to a local telephone number.

In some respects this is like what the Internet offers, with newsgroups, anonymous ftp and WWW. In fact, it can be claimed with justice that the Internet is slowly groping towards the type of service which has long been available on systems like CompuServe. Only recently, with the emergence of new, reliable and user-friendly toolsets, has the Internet become easily accessible to those who are not networking enthusiasts. The Internet has still some way to go, in terms of ease of access to relevant information.

Especially in Europe, where home and personal connectivity to the Internet is not very high as yet, CompuServe offers an excellent medium to allow for wide

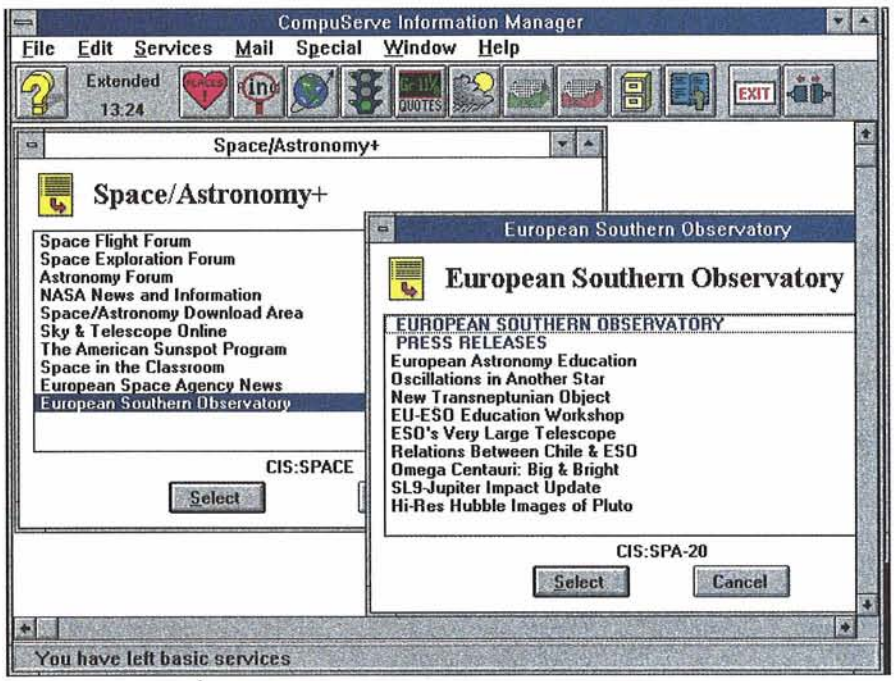

A view of CompuServe, as seen on a Windows notebook, showing the Space/Astronomy area and ESO press releases. Items are clicked on, to access contents. ESO images are available in the area's libraries.

distribution of ESO press information. A basic personal Internet link would not allow for easy transfer of image material. For this reason, access to CompuServe is practical for journalists, teachers and educators, and for others whose professional work environments do not bear the infrastructural costs of Internet access. Unlike national on-line services in Europe, CompuServe is significantly represented internationally. A final point in favour of CompuServe over its large Internet cousin is that much of the information available is of greater quality, not least the messages exchanged in the discussion groups.

During the 'comet week' in July 1994, CompuServe saturated just like various places on the Internet. At the end of the Shoemaker-Levy 9 event, 628 images were available on CompuServe, and 258 information files, originating in 37 observatories or institutes. In addition, there had been 22 video files and many thousands of messages exchanged.

Growth in CompuServe's subscription base is around 50 % per annum. CompuServe's Space/Astronomy area gets several thousand accesses per week. ESO's press releases are made available there, at the time of release. Many expressions of appreciation have been received from CompuServe members regarding this possibility to access information on ESO's work.

For further information please contact:
F. Murtagh, ST-ECF, Garching
(Internet: fmurtagh@eso.org
CompuServe: 100120,3377)

ANNOUNCEMENTS

Council and Committee Members in 1995

Council

Belgium:	J.P. Swings (Vice-President)
	E.L. van Dessel
Denmark:	H. Jørgensen
	H. Grage
France:	B. Fort
	J. Fouan
Germany:	D. Reimers
	A. Freytag
Italy:	F. Pacini
	C. Chiuderi
	E. Campo
The Netherlands:	E.P.J. van den Heuvel
	J. Bezemer
Sweden:	B. Gustafsson
	B. Brandt
Switzerland:	G. Tammann
	P. Creola (President)
	St. Berthet
Portugal:	F. Bello (Observer)

Committee of Council

J.P. Swings	E. Campo
H. Grage	J. Bezemer
J. Fouan	B. Gustafsson, B. Brandt
A. Freytag	P. Creola
F. Pacini	

Scientific Technical Committee

J. Andersen* (1992–96)	T. Lago (1991–95) (Observer)
S. Beckwith (1994–98)	O. Lefèvre (1995–97)
A. Blecha (1992–96)	B. Marano (1993–97)
R. Braun (1993–97)	S. Ortolani (1993–97)
K.S. de Boer (1991–95)	J.W. Pel (1992–96)
D. Dravins (1993–97)	Ch. Sterken (1990–96)
R. Foy (1990–95)	J. Mould (Observer)

Finance Committee

Belgium:	P. Léger
Denmark:	B.K. Rosengreen
France:	P. Laplaud/M. Nauciel
Germany:	M. Stötzel
Italy:	U. Sessi
The Netherlands:	J. Bezemer
Sweden:	J. Gustavsson*
Switzerland:	M. Gottret
Portugal:	F. Bello (Observer)

Observing Programmes Committee

Members	*Substitutes*
C.-J. Björnsson (1993–97)	E. van Groningen
J. Lequeux (1994–96)	M. Gérin
G. Chincarini (1992–96)	G. Vettolani
Knude (1994–98)	P. Kjærgaard Rasmussen
J. Krautter* (1992–96)	Th. Gehren
W. Schmutz (1993–97)	Y. Chmielewski
C. Waelkens (1995–99)	H, Dejonghe
F. Verbunt (1993–97)	J. Lub
T. Lago (1993–96) Observer)	
J. Mould (Observer)	
	P. Barthel, Member at large
	R. Sancisi, Member at large
	C. de Bergh, Member at large

Users Committee

N. Bergvall (1993–96)	P. Magain (1995–98)
M. Dennefeld* (1992–95)	B. Nordström (1995–98)
S. Di Serego Alighieri (1993–96)	H. Schild (1994–97)
F.P. Israel (1994–97)	H. Zinnecker (1992–95)
J. Mould (Observer)	

*Chairman

Time-Table of Council Sessions and Committee Meetings

February 10	Scientific Technical Committee (extraord.)
March 21	Finance Committee (extraord.)
May 2–3	Users Committee
May 4–5	Scientific Technical Committee
May 9–10	Finance Committee
June 7–8	Council
September 25	Finance Committee (extraord.)
November 2–3	Scientific Technical Committee
November 6–7	Finance Committee
November 21–24	Observing Programmes Committee
November 28–29	Council

Programmes Approved for Period 55

Key Programmes

ESO No.	Names of PIs	Title of submitted programme	Telescope
1-003-43K	de Lapparent et al.	A redshift survey of galaxies with $z \leq 0.6$ using multi-slit spectroscopy	NTT
1-023-49K	Böhringer et al.	Redshift survey of ROSAT clusters of galaxies	2.2-m
4-004-51K	Turatto et al.	A photometric and spectroscopic study of supernovae of all types	3.6-m, NTT, 2.2-m, 0.9-m Du
9-002-49K	Epchtein et al.	Deep near-infrared survey of the southern sky (DENIS)	1-m
9-004-51K	Ferlet et al.	Is our halo dark matter made of compact objects?	GPO

ESO No.	Names of PIs (in alphabetical order)	Title of submitted programme	Telescope
D-0949	Abbott/Haswell/Patterson	Disk precession in ultrashort-period cataclysmic variables	1.5-m
D-0921	Abbott/Shafter	Time series photometry of old novae	0.9-m Dutch
E-0555	Achmad/Lamers	The mechanism of mass loss in A, F, G supergiants	1.4-m CAT
C-0022	Acker/Köppen/Stasinska/Stenholm/ Durand Aerts/Waelkens	Oxygen abundances in the galactic bulge from planetary nebulae	1.5-m
D-0775	Aerts/Waelkens	Mode identification in the rapidly rotating β Cephei stars κ and λScorpii	1.4-m CAT
C-0816	Ageorges/Eckart/Quirrenbach	Sharp imaging and polarimetry of reflection nebulae associated with young stellar objects	NTT
E-0733	Ageorges/Hofmann/Ménard	Two-dimensional polarisation observation of highly polarised young stellar objects	NTT
E-0738	Alcalá/Bouvier/Covino/Krautter/Magazzù/ Martín/Rebolo/Terranegra/Wichmann	Study of the evolution of lithium and rotation in low-mass Pre-Main Sequence stars	3.6-m
E-0792	Alcalá/Sterzik/Neuhäuser/Schmitt/ Covino/Terranegra	A search for young disk population stars from the ROSAT All-Sky Survey	1.5-m
A-0768	Andreani/La Franca/Miller/Cristiani/ Lissandrini	The cosmological evolution of the clustering of quasars	3.6-m
F-0654	Arlot/Thuillot/Bouchet/Colas/Descamps/ Sicardy/Vu	Observation of the events of the satellites of Saturn	0.5-m
D-0703	Augusteijn/Abbott/Rutten/van Paradijs/ van der Klis	A comparative study of disk and halo cataclysmic variables	0.9-m Dutch
D-0701	Augusteijn/Spruit/Groot/van Paradijs	Phase-resolved spectroscopy of the eclipsing dwarf nova GS Pav	1.5-m Danish
D-0502	Baade/Stefl/Cuypers	Origin and coupling of stellar and circumstellar Balmer jump variations	1.5-m, 1.4-m CAT, 0.5-m
C-0416	Baluteau/Joubert/Cox/Armand	Physical conditions in and around compact HII regions	2.2-m
F-0489	Barucci/Fulchignoni/Lazzarin/De Sanctis/ Dotto	Study of the physical and chemical properties of asteroids 1071 Brita, 3057 Malaren and 3328 1985 OD1: possible ROSETTA targets	1.5-m
E-0855	Bedding/Frandsen/Kjeldsen/Cram/ Christensen-Dalsgaard/Dall	Oscillations in α Centauri A: a challenge to stellar evolutionary theory	3.6-m
A-0843	Bedding/Minniti	Population studies with Come On+: the dwarf irregular galaxy IC 5152	3.6-m
D-0658	Bell/Schwarz/Pollacco	Time resolved narrow-band photometry of planetary nebula central stars	0.9-m Dutch
B-0583	Bergeron/Le Brun	Identification of the gaseous systems detected by their OVI and Ly α absorption in the quasar spectra of the Hubble Space Telescope Key Project	NTT
A-0984	Bergvall/Rönnback/Masegosa/Hidalgo-Gamez/Östlin	Near-IR imaging of blue low-surface brightness galaxies	2.2-m
A-0691	Bettoni/Galletta/Ciri/Brocca	The nature of peculiar dust-arcs in spiral galaxies	2.2-m
B-0381	Bock/Wagner	Rapid flares and particle acceleration in BL Lac objects	1.5-m Danish
F-0337	Böhnhardt/West/Schwehm/Bär	Investigation of Comet P/Wirtanen, prime target of the ESA ROSETTA mission	2.2-m
A-0987	Bonfanti/Rampazzo/Longhetti/Reduzzi	Using ellipticals in pairs as a probe of the universality of the fundamental plane	1.5-m
E-0575	Bouvier/Allain/Wichmann	The rotational periods of post-T Tauri stars	0.9-m Dutch
E-0450	Bragaglia/Cacciari/Kinman/Carretta	The nearby blue horizontal branch stars	1.4-m CAT
F-0957	Brahic/Ferrari/Lagage/Rotundi/Thebault	1995 Saturn's rings edge-on observations	2.2-m, 0.9-m Du
D-0788	Brandl/Sams/Eckart/Bertholdi/Genzel	Diffraction-limited NIR imaging and identification of WR-stars in R136	3.6-m
A-0498	Bremer/Miley/van Ojik/van der Werf	Evolution and influence of the cluster environment of distant quasars	2.2-m
E-0438	Bues/Karl-Dietze	Spectral variability of single magnetic white dwarfs	1.5-m
D-0383	Burwitz/Reinsch/Beuermann/Schwope	Magnetic field configuration and synchronisation of long-period AM Herculis systems	2.2-m, 0.9-m Du
A-0607	Cacciari/Federici/Held/Stanghellini	A spectroscopic study of the globular clusters in the Sculptor spiral galaxy NGC 253	3.6-m
B-0308	Calvani/Sulentic/Zwitter/Marziani	The very broad line region in active galactic nuclei	1.5-m
B-0954	Campusano/Clowes	Testing a galaxy excess in the direction of the largest known quasar group	NTT
E-0014	Carrasco/Loyola	UBVRI photometry of FK5 faint stars	0.5-m

ESO No.	Names of PIs (in alphabetical order)	Title of submitted programme	Telescope(s)
E-0874	Casanova/Montmerle/Gregorio-Hetem/Martín/Bouvier	A large-scale spectroscopic survey of ROSAT-discovered T Tauri candidates in the ρ Oph star forming region	1.5-m
E-0685	Cayrel/Nissen/Beers/Spite F./Spite M./Andersen/Nordström/Barbuy	Survey of very metal-poor stars in the Galaxy	NTT, 1.5-m
A-0515	Chiosi/Ortolani/Vallenari/Bertelli	Star formation of dwarf galaxies of the Local Group	NTT
A-0887	Clements/Saunders/Mobasher/Sutherland/Kraan-Korteweg/Maddox/Rowan-Robinson/Bottinelli/Tully	Inclinations and extinctions for nearby IRAS galaxies	0.9-m Dutch
A-0890	Clements/Saunders/Mobasher/Sutherland/Kraan-Korteweg/Maddox/Rowan-Robinson/Bottinelli/Tully	An all-sky K'-band Tully-Fisher survey of IRAS galaxies	2.2-m
A-0891	Clements/Saunders/Mobasher/Sutherland/Maddox/Mamon/Rowan-Robinson/Tully	Identification of IRAS galaxies behind the southern Milky Way	2.2-m
B-0411	Clements/Saunders/Sutherland/McMahon/Efstathiou/Rowan Robinson/Lawrence	Spectroscopy of candidate high z IRAS galaxies	3.6-m
A-0480	Collins/Burke/Böhringer/Neumann/Nichol/Romer/Sharples/Kron/Ulmer	A distant sample of X-ray selected galaxy clusters	3.6-m
D-0568	Corporon/Lagrange/Böhm	A search for spectroscopic binaries among Herbig stars	1.4-m CAT
B-0544	Courvoisier/Carrillo/Walter	Observation of circumnuclear regions of Seyfert galaxies through infrared bands	2.2-m
E-0334	Cuntz/Mandel/Kaufer/Wolf/Ulmschneider/Brown	Chromospheric variability of selected K giants	0.5-m
D-0724	Daems/Waelkens	Mapping the accretion disk in the HD104901B system	1.4-m CAT
C-0330	Danziger/Barlow/Liu/Storey	C, N and O abundances of planetary nebulae and H II regions from optical recombination lines	1.5-m
D-0986	Danziger/Bouchet/Gouiffes/Lucy/Fransson/Mazzali/Della Valle/Chugai	SN 1987A	3.6-m, 2.2-m, 1.5-m Danish
A-0831	Danziger/Carollo	Infrared (IR) colour gradients in early-type galaxies	2.2-m
E-0565	de Boer/Theisen/Geffert/Colin/Dauphole/LeCampion	Separating Population II from Population I SdB stars	3.6-m
A-0623	De Grandi/Molinari/Böhringer/Chincarini	Photometric properties of X-ray selected clusters of galaxies	1.5-m Danish
B-0826	de Kool/Ulrich	High-resolution spectroscopy of broad absorption line QSOs	NTT
D-0387	de Martino/Mouchet/Dhillon/Buckley/Bonnet-Bidaud/Mukai	Infrared Spectroscopy of a sample of intermediate polars	NTT
C-0608	de Winter	Detection of circumstellar material and mass-outflow indicators of young stellar objects of intermediate mass	0.9-m Dutch
D-0596	de Winter	Identifying star-grazing bodies in the close vicinity of young intermediate mass stars	1.4-m CAT
F-0548	Di Martino/Barucci/Farinella/Cellino/Migliorini/Lazzarin	Spectroscopic observations of family osteroids	1.5-m Danish
D-0819	Dieters/van Paradijs/Spreeuw/Greenhill/Rutledge	Black hole candidates amongst the old novae	1.5-m Danish
B-0584	D'Odorico/Cristiani/Fontana/Giallongo	Deep imaging of primeval galaxies at $z \sim 4.5$ in the field around the high redshift QSO 1202-07	NTT
A-0856	Doublier/Caulet/Comte	Blue and red photometry of blue compact galaxies at low redshift	1.5-m
E-0016	Drossart/Forni/Benit/Beuzit/Bibring/Encrenaz/Lellouch	Observations of the Jovian system at 4 microns with Come-On+	3.6-m
E-0024	Ducourant/Hawkins	Measurement of parallaxes of 30 brown dwarf candidates	1.5-m Danish
D-0641	Duerbeck/Leibowitz/Seitter/Shara	What powers recurrent novae?	3.6-m
A-0018	Ebeling/Edge/Oliveira	Spectrophotometrical study of optically rich ACO clusters of galaxies featuring a pronounced lack of X-ray emission	3.6-m
A-0687	Eckart/Genzel/Sams/Tacconi-Garman/Hofmann	Proper motions in the galactic centre	NTT
E-0777	Edvardsson/Feltzing/Gustafsson/Lambert/Morell/Tomkin	Europium and Carbon in the galactic disk	1.4-m CAT
C-0908	Eislöffel/Davis/Lioure/Smith	Which shocks in outflows from young stars?	NTT
F-0590	Encrenaz/Schultz/d'Hendecourt/Stuewe/Drossard	A monitoring of Jupiter in the Near-IR emissions of H_2 and H_3+	NTT
B-0409	Falomo/Kotilainen	Near-infrared imaging of flat spectrum radio quasars	2.2-m
A-0812	Felenbok/Balkowski/Cayatte/Kraan-Korteweg/Woudt	MEFOS guaranteed time: Search in the galactic plane towards the Great Attractor	3.6-m
A-0835	Felenbok/Balkowski/Maurogordato/Batuski/Olowin/Slinglend	MEFOS guaranteed time: Spectroscopy of two southern supercluster candidates	
F-0943	Ferrari/Brahic/Lagage/Thebault/Rotundi	Saturn's ring plane crossing: 17-micron observations	3.6-m
E-0631	Ferrari/Bucciarelli/Massone/Lasker/Postman/Le Poole/Lattanzi/Pizzuti	Photometric calibrators for the southern sky surveys	0.9-m Dutch
E-0326	Festin	Deep CCD photometry for determination of the IMF for the latest M-dwarfs	NTT
A-0901	Freudling/Alonso/da Costa/Wegner	The peculiar motion of galaxies	1.5-m, 1.5-m Da
C-0382	Gehrz/Krautter	Measurement of the infrared angular diameters of old nova shells	3.6-m, 2.2-m
B-0615	Gerritsen/Barthel	Probing starburst events in QSOs	NTT
B-0616	Gerritsen/Barthel	Infrared imaging of quasar host galaxies	2.2-m
B-0417	Giallongo/Petitjean/Fontana	The CIV content of the Lyman-α forest	NTT
A-0329	Goudfrooij/Binette/Hansen	Origin and excitation of gas in cooling flow galaxies	1.5-m

ESO No.	Names of PIs (in alphabetical order)	Title of submitted programme	Telescope(s)
E-0764	Gratton/Carretta/Fusi Pecci/Ferraro	Spectroscopic observations of blue straggler progeny in globular clusters	3.6-m, 1.5-m Da
E-0487	Gratton/Carretta/Sneden	Mixing episodes during the RGB evolution of metal-poor stars	1.4-m CAT
E-0388	Grebel	Early evolution of the galactic bulge: Age abundances of bulge globular clusters	2.2-m
D-0704	Grosbøl	Radial velocity field in the Sagittarius spiral arm	1.5-m, 0.5-m
B-0347	Grupe/Beuermann/Mannheim/Reinsch/Thomas	Spectropolarimetry of soft X-ray selected narrow-line Seyfert 1 galaxies	3.6-m
B-0348	Grupe/Beuermann/Reinsch/Mannheim/Thomas	Short-time variability of soft X-ray selected narrow-line Seyfert 1 galaxies	1.5-m
E-0491	Guenther/Emerson/Folha	Spectro-photometry of T Tauri stars with known rotation periods	1.5-m, 0.5-m
D-0003	Häfner/Simon/Fiedler/Sturm	Binaries with early-type components	0.5-m
A-0525	Hammer/Angonin-Willaime	Multiple spectroscopy of luminous arcs	NTT
B-0355	Hasinger/Schwope/Roth/Truemper/Voges	Optical study of a complete sample of bright ROSAT-selected AGN candidates	2.2-m
E-0665	Hawkins	Infrared colours of very low mass stars and brown dwarfs	2.2-m
C-0674	Henning/Hoare/Hofner/Stecklum	High-resolution imaging of ultracompact H II regions with adaptive optics	3.6-m
D-0675	Heydari-Malayeri/Beuzit	Are there stars with a mass over 100 $M_\odot$ in the Magellanic Clouds?	3.6-m
E-0392	Hilker/Kissler	Strömgren metallicities of a large number of evolved stars in ω Centauri	1.5-m Danish
B-0610	Hjorth/Sørensen/Grundahl	Near IR observations of the gravitational lens candidate	NTT
D-0475	Hubrig/Mathys	Magnetic fields in chemically peculiar double-lined spectroscopic binaries	3.6-m
B-0627	Hutsemékers/Lamy/Remy/Van Drom	Spectropolarimetry of broad absorption line (BAL) QSOs	3.6-m
A-0429	Iovino/Chincarini/Garilli/Maccagni/Saracco	A deep, infrared selected, galaxy sample	2.2-m
A-0462	Iovino/Oliveira/Hickson/Focardi/MacGillivray	Morphology and dynamics of galaxies in dense environments	1.5-m, 1.5-m Da
B-0730	Jakobsen/Picard	Searching for large-scale structure surrounding the rich absorption line quasar Q0122-380	3.6-m
D-0582	Kaper/Baade/Fullerton/Gies/Henrichs/Puls	A search for cyclical variability in O-star winds	1.4-m CAT
F-0321	Karkoschka	Spatially resolved spectrophotometry of Jupiter, Saturn, and Uranus	1.5-m
E-0534	Kavelaars/Brigdes/Jablonka/Sarajedini	CMDs for inadequately studied metal-poor galactic bulge globular clusters	1.5-m Danish
D-0459	Koester/Allard	Rotation velocities of white dwarfs	3.6-m
B-0818	Köhler/Wisotzki	Statistical investigation of a complete sample of Seyfert galaxies	1.5-m
D-0008	Kohoutek	Investigation and search for variability of selected planetary central stars	0.9-m Dutch
C-0366	Krautter/Evans/Scott	Nova abundances from infrared recombination lines	NTT
D-0379	Krautter/Starrfield/Wagner	Physical nature of galactic bulge novae in quiescence	NTT
F-0622	Kueppers/Jockers/Chernova	Imaging of oxygen and sulfur in the Io torus	2.2-m
A-0932	Kuijken/Franx	The recent merger remnant NGC 7252	NTT
E-0964	Kunkel/Zinnecker	Radial velocities and $v \sin i$ of Pre-Main Sequence stars in the ScoCen OB association	1.5-m Danish
E-0934	Kunkel/Zinnecker/Schmitt	Optical and infrared photometry of Pre-Main Sequence X-ray sources in the ScoCen OB association	2.2-m, 1.5-m Da
A-0894	Kunth/Schaerer/Meynet	Wolf-Rayet populations in starburst galaxies	2.2-m
E-0361	Kürster/Hatzes/Cochran/Dennerl/Döbereiner	High-precision stellar radial velocities, Part VI	!.4-m CAT
A-0563	La Franca/Petitjean/de Lapparent/Cristiani	QSO MgII absorption systems and large-scale structures	NTT
E-0940	Lagage/Cabrit/Olofsson/Huldtgren	10-micron spectro-imaging of young outflow sources	3.6-m
F-0331	Lagerkvist/Dahlgren/Lahulla/Williams/Fitzsimmons	Rotational properties and shapes of Hilda asteroids	0.9-m Dutch
F-0512	Lagerkvist/Erikson/Magnusson/Piironen	Physical properties of asteroids with long rotational period	0.5-m
F-0589	Lagerkvist/Lagerros/Jämsä/Schloerb	Thermal light curves of asteroids	3.6-m
F-0827	Lagerkvist/Rickman/Magnusson/Dahlgren/Lindgren/Erikson/Lagerros	Physical studies of trans-Neptunian objects	NTT
E-0588	Lagrange/Beuzit/Mouillet/Forveille/Vidal-Madjar/Ferlet/Lecavelier	Search for disks around Main Sequence (MS) stars using adaptive optics in the infrared	3.6-m
D-0567	Lagrange/Corporon	Spectroscopic study of the TY CrA system	1.4-m CAT
B-0834	Lai/Rouan/Lacombe/Gendron	High spatial resolution infrared imaging of starburst activity in AGNs	3.6-m
A-0731	Le Borgne/Soucail/Bezecourt/Mellier/Pelló	Redshift and spectral content of the distant galaxies sources of the arcs in CL2244-02, MS2137-23 and Abell 2104	NTT
A-0635	Le Fèvre/Crampton/Dickinson	Clustering of galaxies around 3CR radio galaxies with $0.8 \leq z \leq 1.4$	NTT
A-0773	Leibundgut/Hamuy/Maza/Phillips/Schommer/Smith/Suntzeff/Spyromilio/Schmidt/Kirshner/Riess	Spectroscopy and photometry of distant supernovae	NTT, 1.5-m Da
E-0481	Leinert/Weitzel/Eckart	Very low mass multiple systems	NTT
E-0492	Leinert/Weitzel/Eckart	Spectral energy distribution of the components of LHS 1070	3.6-m
D-0433	Lennon/Dufton/Kudritzki/Venn	The chemical composition of the galactic centre	3.6-m

ESO No.	Names of PIs (in alphabetical order)	Title of submitted programme	Telescope(s)
F-0828	Lindgren/Rickman/Tancredi/ Fernández/Licandro	Nuclear photometry of short-period comets	1.5-m Danish
A-0711	Longhetti/Rampazzo/Reduzzi	Nature of fine structure in early-type galaxies in pairs	1.5-m
B-0757	Lutz/Genzel/Sternberg/Krabbe/Kunze	Probing stars in AGN and starburst galaxies by CO bandhead spectroscopy	NTT
A-0833	Macchetto/Bender/Capaccioli/ Pastoriza/Sparks	Long-slit spectroscopy of gas-rich elliptical galaxies	3.6-m
A-0647	Macchetto/Giavalisco/Madau/Steidel	Multi-colour medium-band imaging of cluster galaxies at redshift $z \approx 3.4$	NTT
A-0632	Macchetto/Sparks	Geometric measurement of galaxy distances	3.6-m
E-0770	Magain/Hammida/Zhao	Cosmic scatter of heavy elements in halo stars	1.4-m CAT
F-0527	Magnusson/Kwiatkowski/Erikson/ Piironen	CCD photometry of the near-Earth radar target asteroid 1991 JX	0.9-m Dutch
B-0823	Marco/Tacconi-Garman/Alloin/Blietz/ Rouan	Diffraction-limited L-, M-band studies of the Seyfert galaxies NGC 7469 and NGC 1068	3.6-m
B-0646	Marziani/Dultzin-Hacyan/Laurikainen/ Salo	The nature of super-winds in FIR strong galaxies	1.5-m Danish
D-0840	Mathys	Elemental abundances in A and B stars belonging to NGC 6231	NTT
E-0751	Mathys/Hubrig/Landstreet/Lanz/ Manfroid	Systematic search and study of Ap stars with magnetically resolved lines	1.4-m CAT
D-0737	Mathys/Hubrig/Landstreet/Lanz/ Manfroid	Magnetic field geometry in Ap stars with magnetically resolved lines	3.6-m
A-0560	Méndez/Arnaboldi/Capaccioli/Ford/ Freeman/Gerhardt/Hui/Kudritzki/ Quinn	Dynamics of the outer halos of normal elliptical galaxies	NTT
D-0736	Mereghetti/Kaper/Belloni/Haberl/ Voges	Spectroscopy of new Wolf-Rayet candidates discovered in the ROSAT All-Sky Survey	1.5-m
E-0543	Mermilliod/Mayor	Constraints on stellar formation from orbital elements of cluster binaries	1.5-m Danish
D-0452	Mermilliod/Raboud	Fundamental data on stellar formation: the young cluster NGC 6231	2.2-m
D-0451	Mermilliod/Raboud/Levato	Fundamental data on stellar formation: the young cluster NGC 6231	3.6-m
E-0975	Meylan/Bender/Jablonka/Spurzem	Is 47 Tucanae a collapsed-core globular cluster?	NTT
B-0972	Meylan/Courbin/Hammer/Magain	Deep imaging of selected gravitationally lensed quasars	NTT
E-0978	Meylan/Dubath/Jorissen/Mayor	Are the two high-velocity stars in the core of 47 Tucanae genuine cluster members?	NTT
D-0734	Mignani/Goldoni/Bignami/Caraveo	Optical studies of isolated neutron stars detected as high-energy sources	NTT
B-0700	Miley/van Ojik/Röttgering/Bremer	High-resolution study of the ionised gas in $z > 2$ radio galaxies	NTT
E-0557	Minniti	Kinematics of bulge giants and the formation of the Galaxy	3.6-m
E-0349	Moehler/Heber/Rupprecht	Spectroscopy of faint blue stars in NGC 6752	2.2-m
E-0656	Molaro/Rebolo/Martín/Casares/ Charles	Lithium observations in the cool companions of black holes	NTT
C-0936	Molaro/Vladilo/Centurión	High-resolution observations of metal systems in bright QSOs	3.6-m
D-0952	Montmerle/Lagage/Cabrit	Spectral properties of UV/X-ray irradiated circumstellar dust around low- and intermediate-mass young stars	3.6-m
E-0591	Mürset/Dumm/Nussbaumer/Schild/ Schmutz	Rotation of red giants	1.4-m CAT
D-0552	Munari/Zwitter	Spectrophotometric survey of possible cataclysmic variables	1.5-m
A-0969	Näslund/Jörsäter	Deep surface photometry of edge-on spiral galaxies	1.5-m Danish
D-0526	Napiwotzki/Werner/Heber	A search for cool companions of CPN and PG 1159 stars	2.2-m
E-0549	Neuhäuser/Alcalá/Sterzik/Schmitt	Search for weak-line T-Tauri stars in CrA star-forming region	1.5-m
E-0479	North/Bétrix/Künzli	Lithium in evolved metallic A-F stars	1.4-m CAT
D-0851	Nota/Clampin/Schulte-Ladbeck/ Pasquali/Smith/Stroud	Dynamical mapping and abundance analysis of the HR Carinae nebula	NTT
D-0849	Nota/Clampin/Sirianni	Dynamical mapping and abundance analysis of the M1-67 nebula	NTT
A-0950	Östlin/Amram/Bergvall/Boulesteix/ Masegosa/Feltzing/Källander	The velocity field of luminous blue compact galaxies	3.6-m
A-0800	Oliveira/Amram/Balkowski/Boulesteix	Hα velocity fields of galaxies in compact groups	3.6-m
E-0904	Olofsson/Eriksson/Gustafsson/ Olander/Schwarz	Imaging of circumstellar envelopes in resonance scattered light	3.6-m, NTT
E-0467	Ortolani/Guarnieri/Barbuy/Bica	Near-Infrared observations of globular clusters in the galactic bulge	2.2-m
E-0762	Ortolani/Renzini/Rich	The galactic bulge population	NTT
E-0425	Pasquini/Achmad	Absolute magnitudes of cool stars: the Wilson-Bappu law	1.4-m CAT
E-0424	Pasquini/Molaro	Li abundance in turnoff stars of NGC 6397	NTT
A-0005	Pellegrini/Böhringer/Danziger	A study of a complete sample of galaxy clusters detected by ROSAT	3.6-m
A-0821	Petitjean/Smette/Surdej/Shaver/ Mücket/Remy	Structure of the Universe at low z from the Lyα gas	NTT
E-0779	Pettersson/Edvardsson/Westerlund	Lithium abundances and age of the ζ Scl open cluster	NTT, 0.9-m Dutch
A-0506	Piotto/Ferraro/Origlia/Palazzi	Near-Infrared observations of Cepheids in Local Group galaxies	2.2-m
D-0550	Pollacco/Schwarz/Bell/Aspin	Binary central stars of planetary nebulae: the progenitors of the cataclysmic variables?	NTT
E-0399	Poretti/Bossi/Mantegazza/Riboni/ Zerbi	Pulsation mode identification of the δ Sct star FG Vir	1.4-m CAT
C-0880	Pottasch/Manchado/García-Lario	Direct imaging and photometry of proto-planetary nebulae candidates	1.5-m Danish

ESO No.	Names of PIs (in alphabetical order)	Title of submitted programme	Telescope(s)
C-0916	Pottasch/Manchado/García-Lario	Infrared imaging and photometry of proto-planetary nebulae candidates	2.2-m
A-0019	Queloz/Dubath/Mayor	Search for an extended dark matter component in the Sculptor dwarf spheroidal galaxy	NTT
B-0666	Quirrenbach/Eckart/Genzel/Tacconi-Garman/von der Lühe	Diffraction-limited near-IR imaging of the nucleus of NGC 1068	NTT
A-0698	Rafanelli/Richter/Lipovetsky/Izotov/Kohler/Wisotzki/Esposito/Radovich	Chemical abundances of blue compact galaxies from Hamburg-ESO Survey	1.5-m
A-0564	Ramella/da Costa/Nonino/Geller/Smith/Pellegrini	Redshift survey of a dense region of the southern sky	1.5-m
E-0808	Randich/Schmitt	Investigating the early main sequence evolution of low-mass stars	1.5-m
D-0319	Rauch/Werner	Neon abundance in PG 1159 stars	3.6-m
A-0662	Reduzzi/Rampazzo/Combes/Bonfanti	Frequency of tidal distorsions in a complete sample of southern E+E pairs	3.6-m
A-0811	Robertson/Leibundgut	Spectroscopic search for Lyman alpha emission in damped systems	NTT
A-0516	Rönnback/Thimm/Hopp/Bergvall	A search for low surface-brightness galaxies with star-formation activity in the galaxy cluster A 3998	NTT
D-0530	Ruiz	Luminosity function of cool white dwarfs	3.6-m
A-0965	Sahu	The observed microlensing events towards the galactic bulge	3.6-m
B-0864	Sams/Genzel/Eckart	High spatial and time resolution infrared studies of the superluminally expanding galactic source GRS1915+105	NTT
A-0514	Saracco/Garilli/Iovino	Optical multicolour luminosity function of field galaxies	0.9-m Dutch
D-0598	Schmutz/Folini/Mürset/Nussbaumer/Schild/Walder	Doppler tomography of the wind-wind interaction zone in S-type symbiotic systems	1.4-m CAT
E-0466	Schmutz/Mürset/Nussbaumer/Schild	Orbital elements, M giant radius, and distance of symbiotic systems	1.4-m CAT
B-0447	Shaver/Wall/Kellermann	A search for radio-loud quasars at $z > 5$	3.6-m, 2.2-m
F-0015	Sicardy/Arlot/Beuzit/Colas/Descamps/Jorda/Lacombe/Poulet/Thuillot	Imagery of Saturn ring plane crossing in May and August	3.6-m
B-0905	Siebenmorgen/Cimatti/Freudling	Primordial dust in distant radio galaxies	3.6-m
B-0988	Siebenmorgen/Krügel/Zeilinger/Freudling	Probing the radiation field in active galaxies	2.2-m
B-0727	Smette/Williger/Petitjean/Surdej/Shaver/Mücket/Remy	Extent of the Ly-α clouds	NTT
D-0798	Stecklum/Eckart/Löwe/Hofner/Henning	High-resolution infrared interferometry of young, massive stars	NTT
A-0532	Stein/Binggeli/Jerjen	Dynamics of dwarf galaxies in the Centaurus cluster	0.9-m Dutch
D-0317	Sterken/Thé/Hensberge/Bruch/Wolf/Jorissen/Vreux/Vogt	Long-term photometry of variables	0.5-m
C-0574	Strom/Verbunt/Johnston	Emission from a radio/X-ray knot expelled by the Vela supernova	2.2-m
C-0313	Szeifert/Baschek/Gummersbach/Kaufer/Wolf	Element abundances towards the galactic centre	0.9-m Dutch
E-0403	Tagliaferri/Cutispoto/Pallavicini/Pasquini/Fleming	Spectroscopic and photometric studies of cool stars detected by WFC and EUVE	1.4-m CAT, 0.5-m
D-0522	Telting/Groot/Henrichs/van Paradijs/Piters	Accurate determination of $v \sin i$ of early-type stars	1.4-m CAT
B-0430	Tinney/Gemmo/Zinnecker/Hasinger/Pietsch/Kahabka	The search for QSOs behind Local Group galaxies	NTT
D-0753	Turon/Mermilliod/Gómez/Robichon/Sellier/Guibert	Photometric calibration for open clusters observed with Hipparcos	1.5-m Danish
C-0719	Van de Steene/Jacoby	Abundance study of new planetary nebulae close to the galactic centre	1.5-m
C-0712	Van de Steene/van Hoof/Waters	Imaging of suspected emerging planetary nebulae	3.6-m, NTT
E-0945	van der Bliek/Schwarz/Nyman/Eriksson/Gustafsson	Symbiotics: ancient mass transfer just like in Ba stars?	1.4-m CAT
D-0339	van der Hucht/Williams/Setia Gunawan/Bouchet	Search and monitoring of eruptive Wolf-Rayet dust formation	2.2-m
D-0520	van der Klis/Augusteijn/Berger/van Paradijs	IR counterparts of highly reddened low-mass X-ray binaries	2.2-m
A-0572	van der Werf	Hα emission from damped Lyman α systems	NTT, 2.2-m
C-0709	van Hoof/Van de Steene/Pottasch	Accurate abundance determination of CNO in planetary nebulae	1.5-m
B-0825	van Ojik/Bremer/Miley	Detailed imaging quasar host galaxies with Come-On+	3.6-m
D-0465	van Paradijs/Charles/Martin/Casares/van der Hooft/van der Klis/Augusteijn	Black hole candidates in quiescent soft X-ray transients: photometry	1.5-m Danish
D-0469	van Paradijs/Charles/Martin/Casares/van der Hooft/van der Klis/Martín/Augusteijn	Black hole candidates in qiescent soft X-ray transients: spectroscopy	NTT
D-0448	van Paradijs/Leibundgut/Abbott/Augusteijn/Strom	Supernova light curves	0.9-m Dutch
D-0023	van Paradijs/van der Hooft/Kouveliotou/Teleso	A 10-micron minisurvey of low-mass X-ray binaries	3.6-m
D-0722	Van Winckel/Waelkens/Waters	The circumstellar material of the binary high-galactic-latitude supergiant HD 213985	1.4-m CAT
D-0602	Veen/van Genderen/van der Hucht	Is WR46 (= HD 104994, WN3pec+?) a 1994L-like supernova precursor? Looking for signs of its companion	1.5-m, 0.5-m
D-0333	Venn/Kudritzki/Lennon/Husfeld	Spectral analyses of A-type supergiants in the SMC and the wind momentum-luminosity relationship for massive stars	3.6-m

ESO No.	Names of PIs (in alphabetical order)	Title of submitted programmes	Telescope
B-0540	Véron/Hawkins	Spectroscopy of variable quasar candidates	3.6-m
A-0797	Vigroux/Sauvage/Césarsky/Mirabel/ Lagage/Gallais	Detailed mid-infrared mapping of the central regions of Centaurus A	3.6-m
C-0929	Vladilo/Centurión/Càssola	The interstellar $^{12}C/^{13}C$ towards Sco OB1: chemical inhomogeneities in the solar vicinity?	1.4-m CAT
B-0385	Wagner/Pfeiffer	Broad-band energy distributions of unidentified EGRET sources	1.5-m Danish
C-0696	Walsh/Clegg/Hui/Jacoby/Peletier/Walton	Using planetary nebulae to probe abundances in the early-type galaxy Cen-A (NGC 5128)	3.6-m
C-0755	Walsh/Walton	Imaging and spectroscopic survey of the Abell planetary nebulae	2.2-m
D-0743	Werner/Rauch/Weinberger/Saurer	Spectroscopy of central stars in old planetary nebulae	3.6-m
F-0461	West/Hainaut/Marsden/Meech	Activity in very distant comets	NTT, 1.5-m Da
D-0913	Wheatley/Watson/Rosen/Verbunt	Time-resolved spectroscopy of stream dips in AM Her-type systems	2.2-m
D-0311	Wolf/Kaufer/Mandel/Stahl/Gäng/Rivinius/ Szeifert/Gummersbach/Sterken/ Kovacs	High-resolution spectroscopic monitoring of B-type supergiants	0.5-m
C-0841	Zanin/Cappellaro/Turatto/Sabbadin	Imaging of new planetary nebulae and photometry of their central stars	1.5-m Danish
A-0001	Ziegler/Bender	The age of elliptical galaxies in clusters	NTT
E-0725	Zijlstra/Minniti	Miras in nearby galaxies (cont.)	NTT
E-0968	Zinnecker/Eckart/Leinert/Alcalá/ Wichmann	The binary frequency among X-ray selected, weak-line T Tauri stars	NTT

ESO-IRAM-NFRA-Onsala Workshop on

SCIENCE WITH LARGE MILLIMETRE ARRAYS

ESO Garching, 11–13 December 1995

The next major step in millimetre astronomy, and one of the highest-priority items in radio astronomy today, will be a large millimetre array with a collecting area of up to 10,000 m^2. Such an array will open new frontiers and make virtually all areas of astronomy accessible to observations in the millimetre wavebands. The purpose of this workshop is to discuss the scientific advances which such an array will make possible.

A wide range of scientific topics will be covered in the following sessions:

- **The early Universe**
- **Galaxies and clusters**
- **Molecular clouds and star formation**
- **Stellar astronomy**
- **Planetary science**

and possible new technologies for large millimetre arrays will also be discussed:

- **Array concepts, configurations, and potential sites**
- **Innovative telescope designs**
- **Prospects for receiver technology**

Scientific Organising Committee:

P. Andreani (Padova), R. Booth (Onsala), L. Bronfman (Santiago), D. Downes (IRAM), P. Encrenaz (Paris), M. Grewing (IRAM), S. Guilloteau (IRAM), R. Hills (Cambridge), F. Israel (Leiden), L. Nyman (ESO), P. Shaver (ESO), E. van Dishoeck (Leiden), F. Viallefond (Paris), J. Whiteoak (Culgoora), T. Wilson (Bonn).

Contact Address:

Peter Shaver, European Southern Observatory,
Karl-Schwarzschild-Str. 2, D-85748 Garching bei München, Germany
e-mail: pshaver@eso.org
fax: +49 89 320-06-480/320-23-62

New Deadline . . . New Deadline . . .

June 15, 1995

ESO Studentship Programme

The European Southern Observatory has positions available for 12 research students. Six of these positions are at the ESO Headquarters in Garching, and the other six are at ESO's Institute of Astronomy in Santiago, Chile. Studentships are for one year, normally renewed for a second year. Up to 3 students may be accepted each year in either place. These positions are available to students enrolled in a Ph. D. (or equivalent) programme in the ESO member states and exceptionally at a university outside the ESO member states.

Note that the closing date for applications has been moved to **June 15,** 1995.

Potential candidates, or their supervisers, should obtain the detailed information about the programme by requesting the brochure and application form from the European Southern Observatory, Studentship Programme, Karl-Schwarzschild-Str. 2, D-85748 Garching bei München, Germany. The brochure describes the prerequisites for participation in the programme, as well as the research interests of the staff member who would act as the local supervisor.

ESO Astrophysics Symposia Series

The proceedings of the ESO Astrophysics Symposia will be published in a new hard bound series by Springer Verlag. This series is intended for the proceedings of those ESO sponsored symposia, conferences and workshops which cover topics closely related to the scientific goals of ESO and will not replace the proceedings of meetings of a more technical nature which are currently produced by ESO. This new series offers a format and price which should make it attractive both to individuals and to libraries. The first three volumes will become available in the spring of 1995. The titles are:

- **The Light Element Abundances**
- **Science with the VLT**
- **The Bottom of the Main Sequence and Beyond**

Springer will handle the production, sales, and distribution of these books. Interested individuals can order these volumes directly from Springer for a price of DM 48.–.

New ESO Conference and Workshop Proceedings

The following two volumes have been edited and submitted to the printer. They will both become available during the month of April 1995.

Third CTIO/ESO Workshop on

THE LOCAL GROUP:
Comparative and Global Properties

(ESO Conference and Workshop Proceedings No. 51)

Editors are A. Layden, R.C. Smith and J. Storm. The volume has 274 pages and its price is DM 50.–.

EUROPEAN SL-9/JUPITER WORKSHOP

(ESO Conference and Workshop Proceedings No. 52)

The price for the 470-page volume, edited by R.M. West and H. Böhnhardt, is DM 80.–.

Prepayment is required for both publications.

Payments have to be made to the ESO bank account 2102002 with Commerzbank München, or by cheque, addressed to the attention of

ESO, Financial Services,
Karl-Schwarzschild-Str. 2,
D-85748 Garching bei München, Germany

STAFF MOVEMENTS

Arrivals

Europe

BÄUMER, Volker (D), Student
BELLER, Angelika (D), Administrative Employee
BONACCINI, Domenico (I), Optical Engineer
DERIE, Frédéric (B), Project Engineer
DUDZIAK, Gregory (F), Student
GERDES, ROLF (D), Engineer
PARESCE, Francesco (I), Senior Astronomer
SBAIHI, Marc (F), Mechanical Engineer
SOGNI, Fabio (I), Archive Operator
VAN LOON, Jaco (NL), Student

Chile

AUGUSTEIJN, Thomas (NL), Fellow
RUSELER, Francisco (NL), Administrator
VAN DE STEENE, Griet (NL), Fellow

Departures

Europe

OCH, Susanne (D), Student

Chile

ABBOTT, Timothy (GB), Fellow
FAUCHERRE, Michel (F), Optical Engineer
LEHMANN, Thomas (D), Student

Transfer

CABILLIC, Armelle (F)
from Chile — Senior Administrator
to Europe — Senior Administrator (Assistant to the Head of Administration)

New ESO Publications

(December 1994 – February 1995)

Scientific Report No. 15: Future VLT Instruments: Scientific Drivers and Concept Definitions. Ed. S. D'Odorico.

Scientific Preprints

1050. C.M. de Oliveira and E. Giraud: Lensing by Compact Groups of Galaxies. *ApJL.*
1051. C.M. de Oliveira: The Nature of Discordant Redshift Galaxies in Compact Groups. *M.N.R.A.S.*
1052. W. Brandner et al.: Low-Mass Star Formation in CG1: a Diffraction Limited Search for Pre-Main Sequence Stars Next to NX Pup. *AA.*
1053. P. Jablonka and D. Alloin: The Nature of Blue Galaxies in Distant Clusters. *AA.*
1054. S. Cristiani et al.: The Space Distribution of the Lyman Alpha Clouds in the Line of Sight to the z = 3.66 QSO 0055-269. *M.N.R.A.S.*
1055. P. Goudfrooij and T. de Jong: Interstellar Matter in Shapley-Ames Elliptical Galaxies. IV. A Diffusely Distributed Component of Dust and Its Effect on Colour Gradients. *AA.*
1056. E. T. Chatzichristou and Ch. Vanderriest: Bidimensional Spectroscopy of Double Galaxies: I. Markarian 463. *AA.*
1057. C.M. Carollo et al.: Dark Matter in Elliptical Galaxies. *ApJL.*
1058. F. Patat, N. Chugai, P.A. Mazzali: Late Time Hα Emission from the Hydrogen Shell of SN 1993J. *AA.*
1059. S. Benetti, L. Pasquini, R. M. West: First Spectroscopic Confirmation of a Microlensing Event towards the Galactic Bulge. *AA.*
1060. B. Leibundgut: Type Ib/c Supernovae and their Relation to Binary Stars. To appear in *Compact Stars in Binaries,* Proc. IAU Symp. 165, eds. J. van Paradijs, E.P.J. van den Heuvel and E. Kuulkers (Dordrecht: Kluwer Academic Publishers).
1061. F. La Franca, A. Franceschini, S. Cristiani, R. Vio: On the Relationship between Optical and X-Ray Luminosity of Quasars. *AA.*
1062. P. Crane, D.L. Lambert, Y. Sheffer: Very High Resolution Survey of Interstellar CH and CH^+. *ApJ.Suppl.*
1063. H.-M. Adorf: Hubble Space Telescope Image Restoration in its Fourth Year. *Inverse Problems* – special issue on *Inverse Problems in Astronomy.* J.C. Brown, Univ. of Glasgow (ed.).
1064. T. Böhm and C. Catala: Rotation, Winds and Active Phenomena in Herbig Ae/Be Stars. *AA.*
1065. D. Minniti: Metal Rich Globular Clusters with R ≤ 3 Kpc. *AJ.*
1066. D. Minniti: The Helium Abundance of the Galactic Bulge. *AA.*
1067. L. Kaper et al.: Wray 977 (GX 301–2): a Hypergiant with Pulsar Companion. *AA.*

Publications Still Available

Most ESO Conference proceedings are still available. To inform you about any volume that you may have missed, we list here some of the more recent volumes.

No. 43	Astronomy from Large Databases II, 1992 ESA/ESO/ST-ECF/STScI Workshop on	DM 70.–
No. 44	Science with the Hubble Space Telescope, 1993	DM 80.–
No. 45	ESO/EIPC Workshop "Structure, Dynamics and Chemical Evolution of Elliptical Galaxies", 1993	DM 90.–
No. 46	Second ESO/CTIO Workshop on Mass Loss on the AGB and Beyond, 1993	DM 70.–
No. 47	5th ESO/ST-ECF Data Analysis Workshop, 1993	DM 30.–
No. 48	ICO-16 Satellite Conference on "Active and Adaptive Optics", 1994	DM 90.–
No, 49	ESO/OHP Workshop on "Dwarf Galaxies", 1994	DM 90.–
No. 50	ESO/OAT Workshop "Handling and Archiving Data from Ground-based Telescopes", 1994	DM 35.–

ESO, the European Southern Observatory, was created in 1962 to . . . establish and operate an astronomical observatory in the southern hemisphere, equipped with powerful instruments, with the aim of furthering and organizing collaboration in astronomy . . . It is supported by eight countries: Belgium, Denmark, France, Germany, Italy, the Netherlands, Sweden and Switzerland. It operates the La Silla observatory in the Atacama desert, 600 km north of Santiago de Chile, at 2,400 m altitude, where fourteen optical telescopes with diameters up to 3.6 m and a 15-m submillimetre radio telescope (SEST) are now in operation. The 3.5-m New Technology Telescope (NTT) became operational in 1990, and a giant telescope (VLT = Very Large Telescope), consisting of four 8-m telescopes (equivalent aperture = 16 m) is under construction. It will be erected on Paranal, a 2,600 m high mountain in northern Chile, approximately 130 km south of the city of Antofagasta. Eight hundred scientists make proposals each year for the use of the telescopes at La Silla. The ESO Headquarters are located in Garching, near Munich, Germany. It is the scientific-technical and administrative centre of ESO where technical development programmes are carried out to provide the La Silla observatory with the most advanced instruments. There are also extensive facilities which enable the scientists to analyze their data. In Europe ESO employs about 200 international Staff members, Fellows and Associates; at La Silla about 50 and, in addition, 150 local Staff members.

The ESO MESSENGER is published four times a year: normally in March, June, September and December. ESO also publishes Conference Proceedings, Preprints, Technical Notes and other material connected to its activities. Press Releases inform the media about particular events. For further information, contact the ESO Information Service at the following address:

EUROPEAN
SOUTHERN OBSERVATORY
Karl-Schwarzschild-Str. 2
D-85748 Garching bei München
Germany
Tel. (089) 32006-0
Telex 5-28282-0 eo d
Telefax: (089) 3202362
ips@eso.org (internet)
ESO::IPS (decnet)

The ESO Messenger:
Editor: Marie-Hélène Ulrich
Technical editor: Kurt Kjär

Printed by Universitäts-Druckerei
Dr. C. Wolf & Sohn
Heidemannstraße 166
80939 München 45
Germany

ISSN 0722-6691

Contents